DIGITAL SIGNAL PROCESSING FOR THE ANALYSIS OF FETAL BREATHING MOVEMENTS

Megeurditch N. Ansourian

B.Sc.(Hons.) M.Sc. A.M.I.E.E.

A thesis submitted for the degree

of Doctor of Philosophy to the

Faculty of Science

University of Edinburgh

1989

ABSTRACT

In this thesis, the application of digital signal processing for the analysis of fetal breathing movements (FBM) is presented. The background history and the possible significance of FBMs in antenatal monitoring is discussed.

Prior to analysis of fetal breathing movements, they must be monitored and detected. Therefore a non-invasive transducer was developed to monitor FBMs using Polyvinylidene Flouride (PVDF) based piezo film and the nonstationary nature of the resulting data and analogue preprocessing designs are discussed. Autoregressive (AR) spectral analysis techniques are presented to model FBMs. The least-mean-square (LMS) and the optimum tapered Burg (OTB) algorithms were used. The problems of deciding the optimum data block length and of selecting the correct model order are also discussed. The performance of the OTB algorithm and the LMS algorithm are compared for highly nonstationary signals.

A rule based expert system which was used to estimate FBM rate is described. The expert system was implemented using the C programming language.

A new FBM pattern was discovered during this research. This pattern is referred to as the "augmented breath" or "deviant pattern". Pattern recognition algorithms are used to identify these deviant patterns and hence quantify their incidence. Conventional classifiers using quadratic and linear Bayesian discriminant functions and Mahalanobis distance are discussed as are classifiers using a neural network structure based on multilayer perceptrons (MLP). The MLP uses the back error propagation algorithm to train the network. The performances of the MLP based neural network and conventional classifiers are discussed in the context of identifying deviant fetal breathing patterns.

DECLERATION OF ORIGINALITY

This thesis and work reported within it was composed entirely by myself in the Department of Electrical Engineering at the University of Edinburgh, Scotland, UK.

Megeurditch N. Ansourian

1/11/1989

ACKNOWLEDGEMENT

I would like to thank my supervisor Dr. James H. Dripps for his encouragement support and guidance. Prof. Peter M. Grant and Prof. James R. Jordan for their support. Dr. Ken Boddy and Dr. Gerald Beattie for their assistance in providing medical expertise and assisting in patient monitoring. Dr. Nigel Colley for providing some of the fetal breathing recordings. Numerous individuals within the university have made the three years enjoyable and productive, and Dr. Keith Manning, Dr. Bernard Mulgrew and Dr. Ahmad Mirzai merit special mention.

I also wish to acknowledge the Royal Scientific Society - Jordan for their financial support.

Dedicated to both
my wife and my mother

for their patience.

TABLE OF CONTENTS

LIST OF ABBREVIATIONS

ALE	Adaptive line enhancement
AM	Amplitude modulation
AR	Autoregressive
ARMA	Autoregressive moving average
DC	Direct current
DSP	Digital signal processing
FBM	Fetal breathing movement
FFT	Fast Fourier transform
FHR	Fetal heart rate
FHS	Fetal heart sound
FM	Frequency modulation
Hz	Hertz
KV	Kilo volts
LED	Light emitting diode
LMS	Least-mean-squared
MA	Moving average
MAM	Maternal abdominal movement
MBM	Maternal breathing movements
MLP	Multi layer perceptron
MMSE	Minimum mean-squared-error
MSE	Mean-squared-error
OTB	The optimum tapered Burg algorithm
PARCOR	Partial correlation
PLL	Phase locked loop
PSD	Power spectral density
PVDF	Polyvinylidene Flouride
SNR	Signal to noise ratio
T.F.	Transfer function
cw	Continuous wave

CHAPTER 1

INTRODUCTION

Digital signal processing (DSP) is mainly concerned with the computer processing of signals represented as discrete time series in digital form. Autocorrelation is one common DSP technique which is used to analyse temporal data, and highlight some of its characteristics, for example periodicities. Analysis is not restricted to the time domain. The digitised data can be transformed, for example, to the frequency domain for analysis. Analysis in either the time or the frequency domain may be used to reveal information contained in the data.

Digital signal processing has undergone phenomenal growth in application in the past two decades. This is largely due to the impact of computers with real-time DSP capability. The availability of powerful digital computers has aroused greater interest in the field and fostered the development and application of increasingly sophisticated and computationally complex algorithms. DSP has become increasingly used in engineering and in non-engineering fields. Applications include: the reduction of noise introduced by a transmission channel; data compression with minimal loss of information, for example in speech and image systems. Prediction of future outcomes of a process from knowledge of the past events, such as in economics, and market forecasting; the detection of underlying periodicities in a given data set, such as periodicities in the sun spot data, or the periods of structural vibration in buildings and mechanical structures; modelling and analysis of physiological activities in

biomedical engineering. These are just few examples of the wide variety of applications of digital signal processing.

1.1. REVIEW OF FETAL BREATHING LITERATURE

The development of accurate and objective antepartum assessment of fetal health *in utero* has long been a challenge to both obstetricians and technologists alike. Antenatal assessment must date back to the dawn of man, when gravid mothers took fetal movements as a reassuring sign of fetal well being. Practice moved away from such non-specific markers, and more objective intrauterine assessment of fetal health was introduced in the nineteenth century, where fetal auscultations were monitored using the simple Leannec stethoscope[1]. With the limitations of human aural perception however, fetal auscultations were only used to provide fetal heart rate (FHR), and hence, fetal distress was only indicated by gross changes of FHR. As science and technology advanced, so facilities were rendered to provide a more specific and accurate diagnostic tests for recognising the fetus at risk *in utero*.

At the turn of the century, Ahlfeld[2] observed rhythmic movements on the maternal anterior abdominal wall during late pregnancy. He ascribed these movements to fetal breathing. These observations of the fetus making breathing movements were discounted by his contemporary peers. The disbelief came about, however, due to the inability of corroborating maternal abdominal wall movements with fetal breathing movement (FBM). Over the years, such observations have been documented using exteriorised fetal lambs[3, 2]. The presence of FBMs in exteriorised fetal lambs was attributed to exposure, tactile and asphyxial stimuli. Sceptism of the presence of FBMs was not overcome until the development of catheter placement techniques and advancements in blood gas determination in the 1960's. These observations were correlated with both intra tracheal flow and recorded pressure changes[3, 4] In addition, numerous investigators have observed rhythmic episodes

in human fetus *in utero*[5, 6, 7, 8].

FBMs *in utero* are not associated with alveolar expansion or gas exchange. Fetal lungs are relatively small in size compared to the rest of fetal organs (figure 1.1). The size of the fetal lung grows with gestation age until taking their final form and size just before term. Figure 1.2 depicts the relative sizes of organs in the newly born.

A reason for having fetal breathing movements *in utero* was proposed by Boddy and Dawes [2]. They postulated it to be a method by which the diaphragmatic musculature develops and as a consequence prepares the human respiratory system to maintain breathing after parturition. Research has been conducted to ascertain the clinical significance of FBMs *in utero* and their possible correlation to interpartum mortality, post natal health and post natal mortality. The clinical value of FBMs as an indicator of fetal health is assuming increasing significance[9, 10]. The mechanisms which control fetal breathing movements are complex and the medical explanation of such mechanisms are well documented for the interested reader[3, 4, 2].

The parameter extracted from FBMs was the breathing rate, and it was observed by many investigators of fetal breathing that FBM rate lies in the range of 30-90 breaths/minute[2, 11, 5, 4]. It was also observed that certain factors, other than fetal health and gestational age, influence FBMs in humans. According to the extent of this influence the behaviour of FBMs would change. Studies have been documented showing that maternal blood glucose level, maternal intake of medication, smoking, alcohol and coffee all have an effect on the incidence of FBMs and on the FBM rate[12, 4]

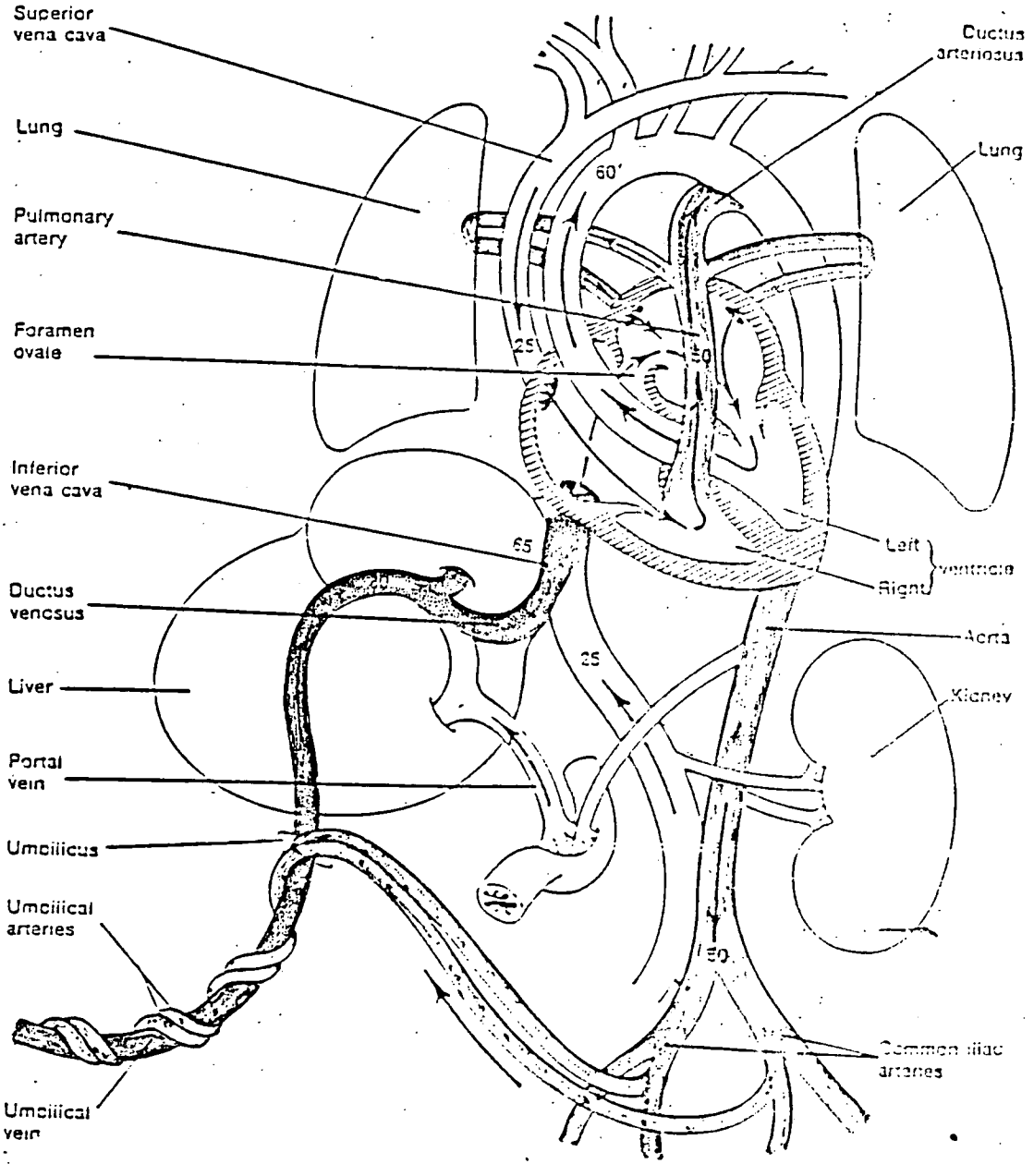

Figure 1.1: A diagram showing the size of fetal lungs relative to the sizes of other fetal organs

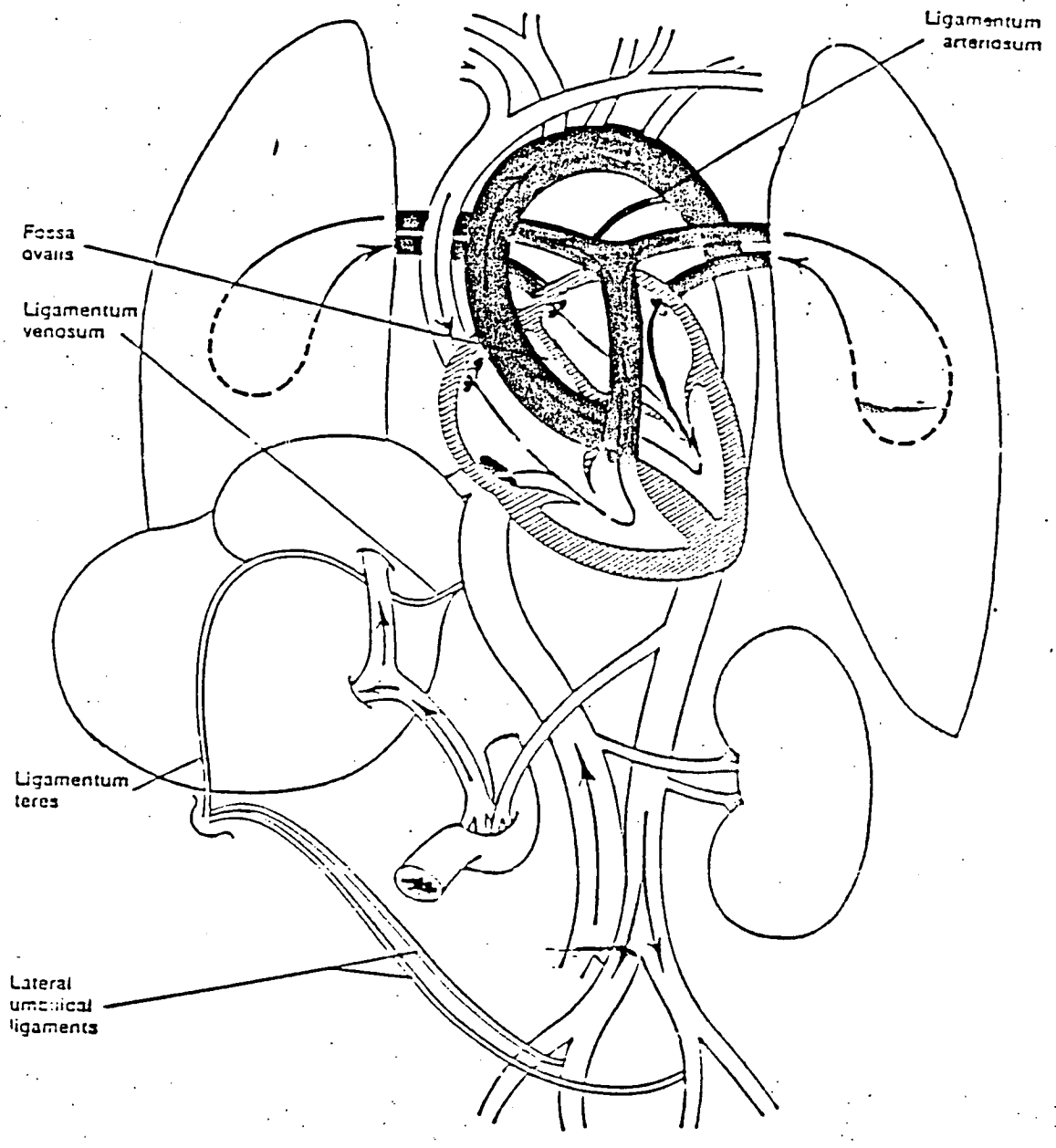

Figure 1.2: A diagram showing the size of lungs for neonates relative to other organs (compared with the size of fetal lungs, figure 1.1)

1.2. FETAL BIOPHYSICAL PROFILE

In the past, fetal biophysical variables were monitored and examined individually, with few interrelationships between the different variables being considered. The individual analysis of fetal variables disjointly provides some assessment of fetal health *in utero*, but leaves considerable room for improvement. This sceptism is confirmed in the fetal mortality rate and the unnecessary medical interventions. Assessment of fetal health entails the synthesis of knowledge from a spectrum of conditions. Manning *et al* [13] developed the fetal biophysical profile.

Five fetal parameters are combined to provide the above biophysical profile. These are:

- Fetal heart rate and patterns.
- Fetal breathing movements.
- Fetal trunk movements.
- Amniotic fluid volume.
- Fetal tone.

The above features are classified into two categories: dynamic and static parameters. Figure 1.3 presents the fetal biophysical profile, depicting the two categories. The fetal biophysical profile analysed fetal parameters in amalgamation to distinguish the normal fetus from the fetus in distress. All variables were considered as being equally significant.

1.3. METHODS OF DETECTING FETAL BREATHING MOVEMENTS

During the late nineteenth century, when fetal breathing movements were first observed, investigators made Kymographic recordings of rhythmic fetal movements as detected from the maternal abdominal wall[14]. Some of the current methods of recording FBMs, are outlined below.

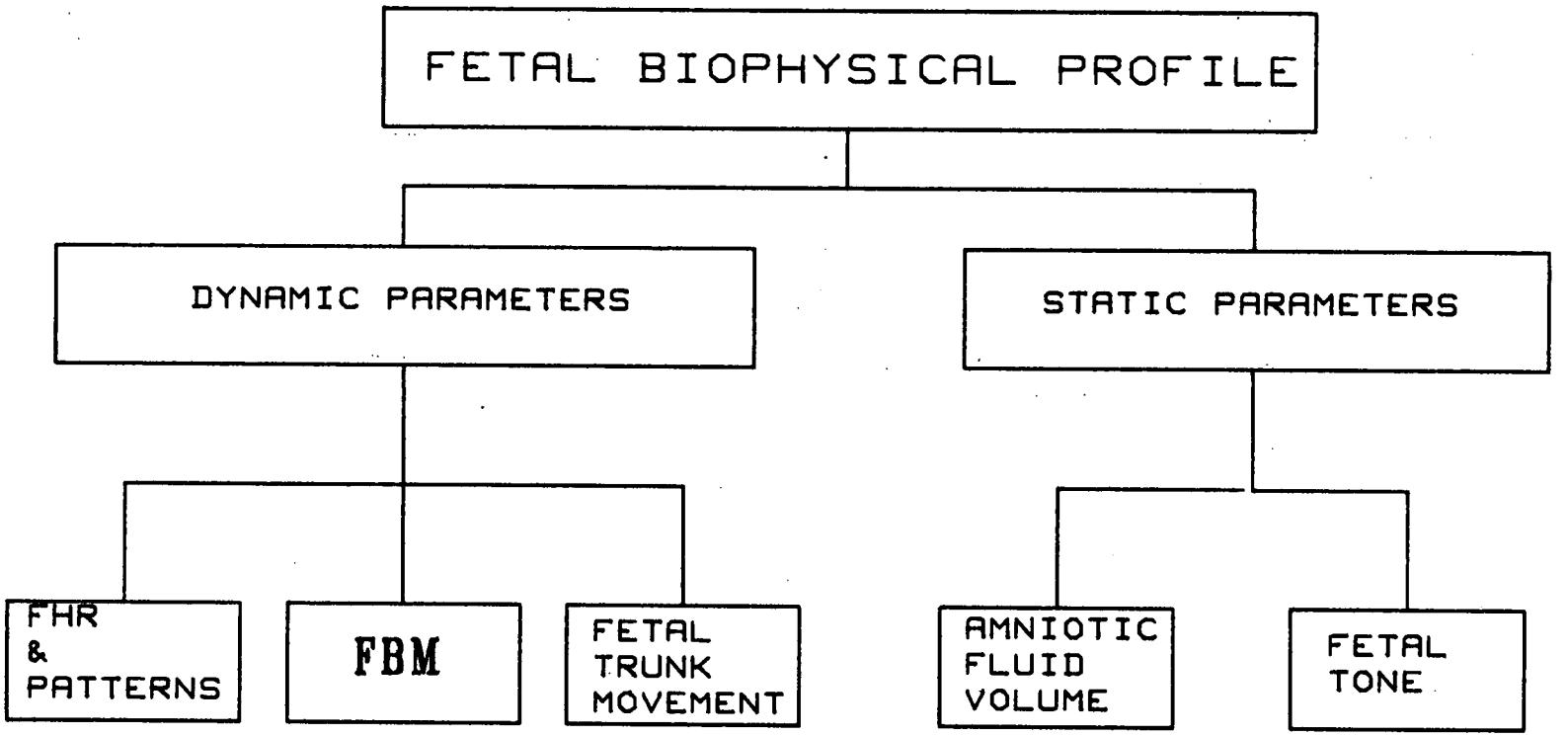

Figure 1.3: Fetal biophysical profile.

1.3.1. ULTRASONOGRAPHY

Boddy and Robinson [5, 15] first described the detection of FBMs using A-mode (Amplitude mode) ultrasonography. A narrow beam pulsed transmitter was placed on the maternal abdomen and the selected echos from the A- scan display representing movements of fetal chest wall were recorded. Fetal heart movement was recognised on the display and from this orientation, echos pertaining to FBMs were identified. Unfortunately, it was often difficult to distinguish FBMs from general fetal movement and signal interference.

The introduction of real time ultrasonography (B-mode or Brightness mode) has overcome the problems encountered using the above method. With B-mode ultrasonography, fetal structures can be observed continuously. The B-mode scanner comprises linear array transducer, and a two-dimensional cross sectional image of the fetus is obtained. The ultrasound beam is aligned with the fetal thorax, and the A-scan output from the distal or proximal chest wall echoes can be recorded. The recorded output varies in sympathy with fetal chest wall movements and hence indicates FBMs[7, 15, 16, 4, 17, 5].

Although FBM is characterised by fetal thoracic wall movements, it can also include diaphragmatic movements. Rapoport and Cousin[18] used a real time ultrasound scanner, but adapted it to incorporate a multiple gate tracking facility. The latter provided simultaneous tracking of both fetal thoracic wall and diaphragmatic movements. The instrument was capable of tracking the different fetal movements simultaneously.

Gough and Poore [8] recorded FBMs using continuous wave (cw) doppler ultrasound. This method does not monitor fetal chest wall movements, but it measures FBMs indirectly through its presumed effect on blood velocity in the fetal hepatic vein and the fetal inferior vena cava, at the level of the liver.

The above methods suffer from their need for the presence of a trained observer throughout the recording for frequent realignment of the ultrasound beam following fetal movement.

1.3.2. TOCODYNAMOMETRY

Tocodynamometry involves the recording of signal generated by movements of the fetus with respect to the maternal abdominal wall. Boddy and Mantell[11] demonstrated the use of a strain gauge on the maternal abdominal wall as means of recording FBMs. Tocodynamometry was also used to measure FBMs by Timor-Tritsch[19].

1.3.3. PHONOGRAPHY

Phonocardiography is one of the oldest methods of detecting biophysical activities in the body. The application of ultrasound has raised the question of its possible biological effect on the fetus, particularly in the case of long term monitoring. Unfortunately, such fears have not yet been alleviated. Phonography has not been a favourable method in the past due the relative inefficiency of the transducers. Talbert *et al*[1] developed a phonographic transducer using a piezoelectric bar. This transducer was capable of detecting fetal heart sounds as well as fetal breathing movements and was compliance matched to the maternal abdomen to ensure a more efficient energy transfer, and hence an improved sensitivity. Goovaerts *et al*[14] developed a similar transducer but based on the inductive principle.

1.4. ANALYSIS OF FBMs

Conventional time-domain analysis of FBMs was conducted by visual inspection† of the recorded signal. This is prone to error and is laborious, especially in the

† This entailed measuring the percentage time a fetus spends breathing and the estimate of breathing rate.

presence of noise. However, investigators have come to rely on this method as it provides them with a quick result. Visual inspection is the only available method when real time ultrasound imaging is used to monitor FBMs.

Stagg and Gennser[20] used the phase-lock-loop (PLL) principle to analyse FBMs. The signal used was recorded using a real time ultrasound imaging scanner. The analogue filtered output of the phase comparator provided an analogue estimate of FBM rate. The PLL had a free running frequency of 1.1 Hz, and the maximum capture range of $\pm 50\%$. The implicit assumption in this PLL design is that FBM rate lies between 40-80 breaths/minute.

1.5. THESIS LAYOUT

The description of the work commences in chapter 2, where system layout and analogue preprocessing is discussed, and a brief outlook on the different processing methods contained in this thesis. Chapter 3 outlines a non-invasive transducer designed to detect FBMs represented as maternal abdominal wall movements (MAM). The transducing medium used is a piezo film based on Polyvinylidene Flouride (PVDF). It is designed to measure displacements of the order of microns, and the transducer is capable of detecting both FBMs and fetal heart sounds. Chapter 4 extends the work to the analysis of recorded FBMs. Spectral analysis algorithms are outlined before concentrating on the least-mean-squared algorithm which uses the steepest descent principle and the Burg algorithm and its variants (i.e. different weighted windows). At the end of chapter 4 the performance of the various algorithms is compared for the specific application case of modelling nonstationary signals.

Chapter 5 presents a brief review of different realisation of expert systems and their merits. A rule based expert system is discussed which was developed to track

the peaks of an autoregressive spectral model pertaining to FBM rate. The results of the peak tracking algorithm to estimate FBM rate is presented.

The detection of the incidence of deviant breathing patterns is presented in chapter 6. Pattern recognition algorithms were used to detect their occurrence. In the absence of a universal definition of these patterns, a definition is presented. The features selected to describe both normal and deviant breathing patterns are presented. Different conventional classification techniques were used, and these were outlined:

- Equal and non-equal Bayesian discriminant functions
- Mahalanobis distance classifier.

In recent years, there has been a new interest in computational models based on human biological neural structures. These so called "neural networks" are gaining popularity as tools for artificial intelligence and pattern recognition. Chapter 6 also outlines the principles of neural networks in pattern recognition. The structure of the neural network which was used is the multilayer perceptron (MLP) with back error propagation algorithm. The performance of the different classification techniques is also compared at the end of chapter 6.

In the final chapter, the conclusions drawn from the work in this thesis are presented.

CHAPTER 2

SYSTEM LAYOUT AND ANALOGUE PREPROCESSING

This chapter presents the outline of the system used to analyse FBMs. Figure 2.1 is a system block diagram. It shows the signal path and the preprocessing carried out from the maternal abdomen through to the output showing FBM rate. This chapter deals mainly with the analogue signal preprocessing required prior to the digitisation. Section 2.1 discusses the signal properties and characteristics. The transducer design and associated aspects are presented in chapter 3 in detail. Section 2.2 discusses the patient isolation incorporated with the transducer. Section 2.3 introduces the analogue filtering and preemphasis used. Section 2.4 presents the digitisation prior to downloading the signal to a digital computer for analysis.

2.1. SIGNAL PROPERTIES

Fetal breathing movement *in utero* is considered as either thoracic or diaphragmatic movements or both. The use of a single gate tracking real time ultrasound imaging scanner only allows one of these two movements to be monitored. The fact that either or both movements may occur simultaneously means that the single gate tracking scanner may not provide the true reflection of FBMs. A scanner incorporating two gate tracking[18] has provided the ability to monitor both fetal thoracic and diaphragmatic movements. In this thesis, FBMs are monitored and recorded using phonography. Sound waves are acoustic pressure waves travelling through a

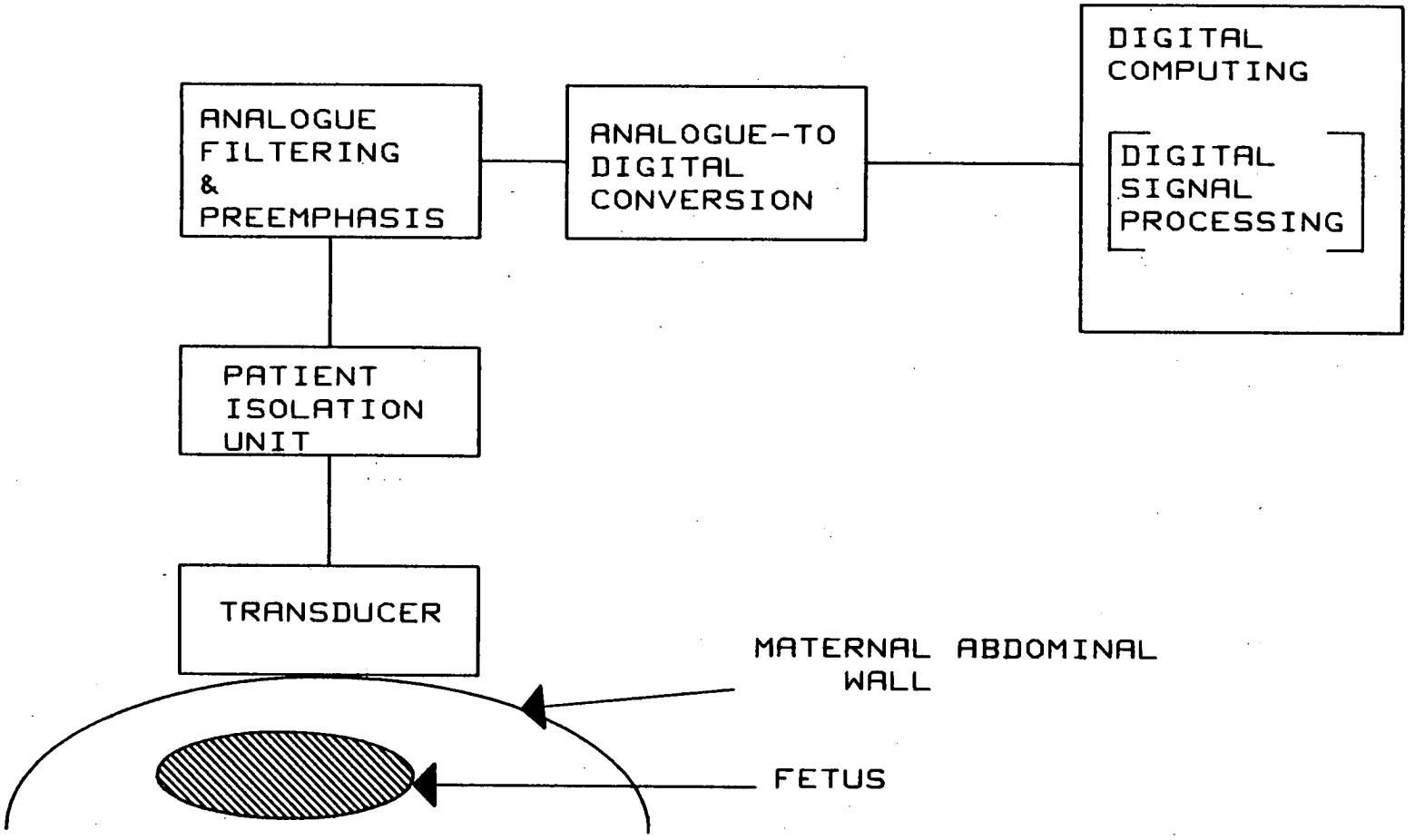

Figure 2.1: Schematic layout for FBM analysis

medium. In the cases of fetal breathing movement, fetal thoracic and diaphragmatic movements generate pressure waves which travel through the amniotic fluid towards the maternal abdominal wall. The surface of the maternal abdomen oscillates in sympathy with the pressure waves travelling through the abdomen.

Unfortunately, FBM is not the only biological activity generating pressure waves in the maternal abdomen. There are maternal and fetal biological organs which also transmit pressure waves to the surface of the maternal abdominal wall. Fortunately most of these corrupting signals have different amplitudes and are in a different frequency band. The corrupting signals generated from fetal biophysical activities are: fetal heart sounds and fetal trunk and limb movements. The most significant corrupting signals generated from maternal biophysical movements are: maternal heart sounds generated through the maternal abdominal artery and maternal breathing movements.

The significant information detected from maternal abdominal wall movements is contained in two frequency bands. In the low frequency band (0.1 - 2 Hz) components relating to fetal breathing and maternal breathing are present. In the upper frequency band (40 - 60 Hz) fetal and maternal heart sounds are present. Fetal and maternal heart sounds, which are present in the upper frequency band have amplitudes of the order of 40 dB below that of fetal breathing movements. In chapter 3, aspects of the design of the transducer to monitor fetal breathing movements and fetal heart sounds are discussed in detail.

2.2. PATIENT ISOLATION

When connecting patients to electrical apparatus, one of the main points which must be taken into consideration is patient safety. It is a prerequisite that patients must be isolated from the parts of the apparatus connected to the mains. The pur-

pose of this isolation is to protect the patient from electric shocks. It must be borne in mind that currents in milliamperes can damage living tissue applied through the skin (British standards BS5724), and if such a current is applied for a prolonged period of time then it could also be fatal. There are clinical requirements set for patient safety. Principally, there must be voltage isolation of at least 800 volts between parts connected to the patient and those connected to the mains.

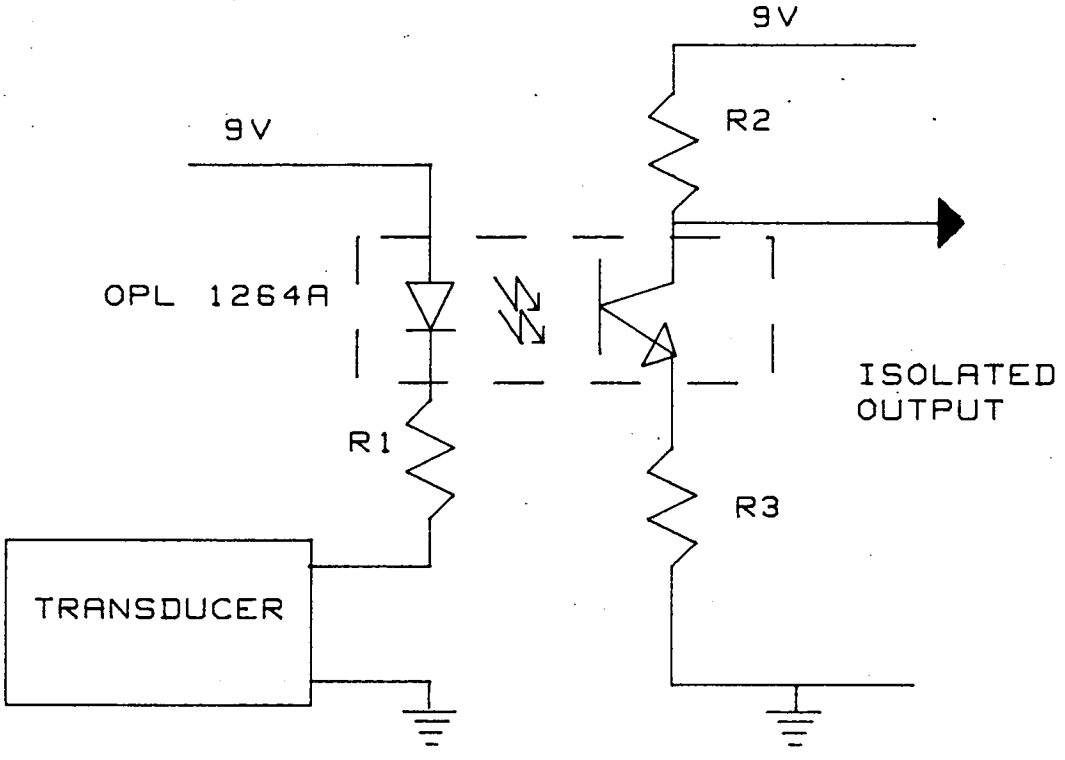

Figure 2.2: Opto-isolator circuit.

There are different principles commonly applied to provide patient voltage isolation. These are based on optical, capacitive or inductive transfer of signals applied to the patient or transduced from the patient.

In this research, isolation is using a commercially available opto-isolator (OPL 1264A). The opto-isolator consists of a GaAsP light emitting diodes optically coupled to an NPN silicon phototransistor. The form of the construction used for this

particular isolator provides a 10 KV isolation between the input and the output.

Figure 2.2 depicts the final circuit incorporating the chosen opto-isolator which provides effective voltage isolation and an efficient signal transfer. The resistor R1 at the cathode of the light emitting diode (LED) controls the quiescent current for the light emitting diode. The resistors R2 at the collector of the phototransistor and R3 at the emitter of the phototransistor control the collector current, the bias points of the phototransistor and the gain of the system. This design performs well down to zero Hertz. This DC coupling results, because the output signal is dependent on the intensity of the LED which depends on the current passing through the diode, which, in turn, is a function of the input signal.

2.3. ANALOGUE FILTERING AND PREEMPHASIS

This section outlines the active filters which were used to extract FBMs from raw maternal abdominal wall movements. Theoretical analysis of the analogue filters is not presented in this section as these are to be found in common text books on filtering[21, 22, 23].

Fetal breathing usually occurs in the range of 30 to 90 breaths/minute[3, 1, 16]. Talbert *et al* [1] suggested filtering the transduced signal in a frequency band of 0.5 - 2.0 Hz. This was achieved by cascading a high pass filter and a low pass filter, each with the appropriate cut off frequencies. In the course of this research, it was observed that the use of the high pass filter distorts FBM signals due to the non-linear phase characteristics of the high pass filter in the transition band[21, 22]. Consequently, only a low pass filter was used to highlight FBMs. Figure 2.3 depicts the second order Sallen-Key low pass filter which was used[22, 23]. The cutoff frequency is given as:

$$f_c = \frac{1}{2\sqrt{2}(\pi CR)} \tag{2.1}$$

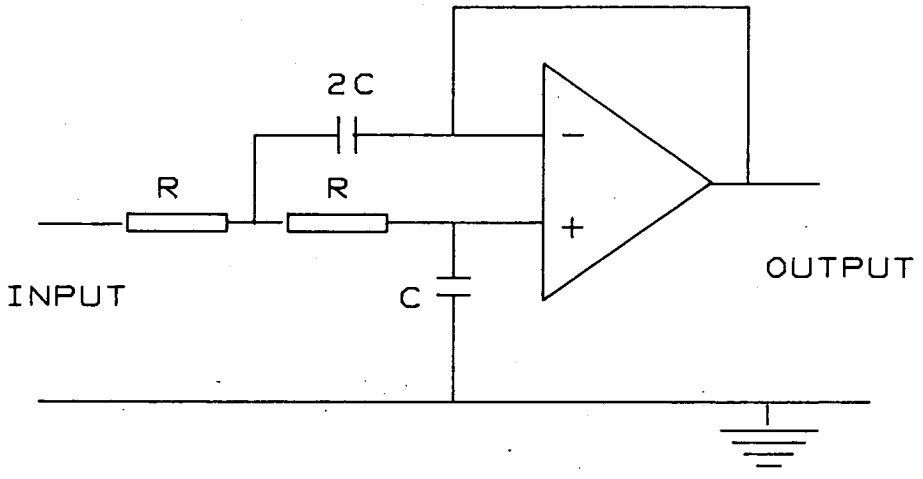

Figure 2.3: Second order low pass Sallen-Key filter.

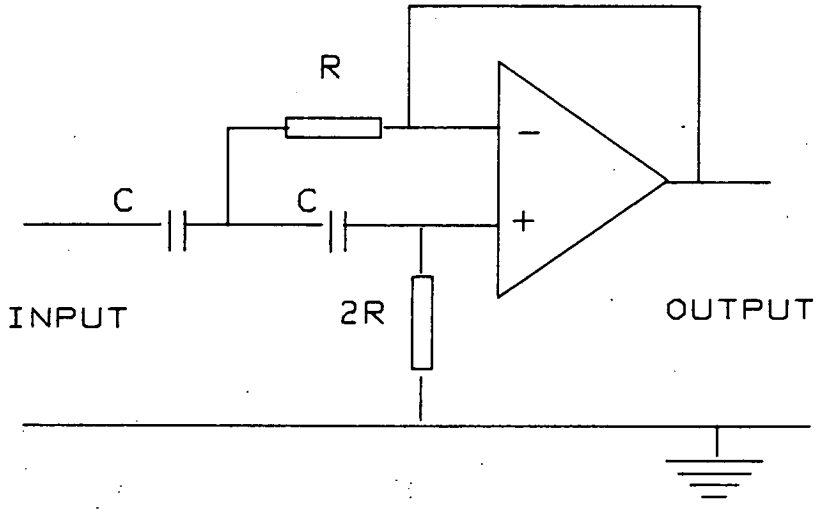

Figure 2.4: Second order high pass Sallen-Key filter.

Fetal heart sounds are also important parameters in fetal monitoring. Section 2.1, outlined the detection of fetal heart sounds using maternal abdominal wall movements. Colley *et al*[24] have detected fetal heart sounds by high pass filtering

maternal abdominal wall movements with a 50 Hz cutoff frequency filter. In this research, it was found that using a second order low pass filter with a cut off frequency at 60 Hz cascaded with a high pass filter with a cut off frequency of 40 Hz provides a clear record of fetal heart sounds. The amplitude of fetal heart sounds was found to be about 40 dB below that of FBMs. Figure 2.4 depicts the second order Sallen-Key high pass filter which was used. The cut off frequency of this high pass filter is similar to that given for the low pass filter (equation 2.1).

In order to provide FBMs and fetal heart sounds (FHS) with comparable amplitudes, some preemphasis is required. This preemphasis reduces the dynamic range requirement of the subsequent analogue to digital conversion. Figure 2.5 is a block diagram of the analogue filtering and the preemphasis.

2.4. ANALOGUE TO DIGITAL CONVERSION

So far the signal has been processed (filtering and preemphasis) in analogue form. However, there is a significant advantage offered by processing this continuous signal in discrete-time form. The processing of the discrete-time signal can be implemented using digital techniques which are potentially more stable and have more dynamic range than their analogue counterparts. The digitising process represents an analogue signal in a sequence of digital codes. The baseband signal, being maternal abdominal movements in this application, is in analogue form and contains desired and undesired information. Consequently, the digitising process comprises three basic steps: sampling, quantising and encoding (figure 2.6).

2.4.1. SAMPLING

Sampling is the process of representing signals by samples taken at appropriately spaced intervals. One of the conditions for proper sampling is that it must be possible to recover the continuous signal from the sampled data, without any loss of

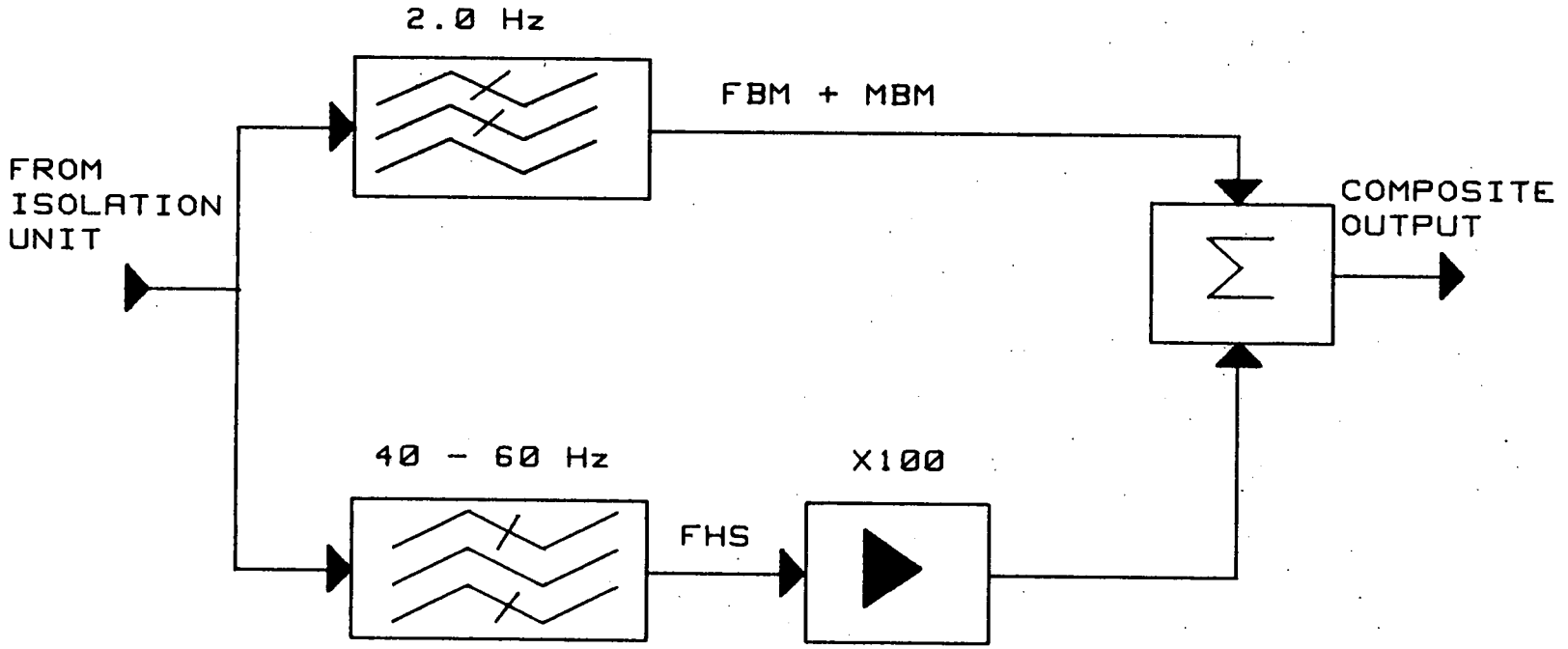

Figure 2.5: Analogue filtering and preemphasis

Figure 2.6: Digitising analogue signal.

information.

$$x_\delta(t) = x(t) \sum_{n=-\infty}^{\infty} \delta(t - nT_s) \tag{2.2}$$

Where $x(t)$ is the continuous signal, $x_\delta(t)$ is the sampled data, T_s is the sampling interval, and $\delta(\tau)$ is the dirac delta function which is a unit impulse and has the value of zero everywhere except at $\tau = 0$.

However, there are some restrictions imposed on the signal to ensure the successful recovery of the continuous data. The restrictions are stated in the *uniform sampling theorem*[25, 26]. This theorem requires that the signal does not contain any components above a certain frequency, W, and that the sampling interval must be less than 1/2W (the Nyquist interval). Therefore, prior to sampling, the continuous analogue signal must be low pass filtered with a lower stopband frequency of less than half the sampling frequency. The Fourier transform of equation (2.2) is[26, 25]:

$$\begin{aligned} X_\delta(f) &= X(f) * \left[f_s \sum_{n=\infty}^{\infty} \delta(f - nf_s) \right] \\ &= f_s \sum_{n=-\infty}^{\infty} X(f - nf_s) \end{aligned} \tag{2.3}$$

Where $X(f)$ is the Fourier transform of the bandlimited signal, $X_s(f)$ is that of the sampled signal and f_s is the sampling frequency.

Therefore sampling a band limited continuous signal results in a periodic repetition in the frequency domain of the signal $X(f)$ with spacing of f_s. When the sampling frequency is reduced, this results in the reduction in the frequency spacing of the periodic repetition. When sampling frequency is less than twice the maximum frequency content (2W) in the continuous signal, $f_s < 2W$, then the periodic repetitions of the spectrum $X(f)$ will overlap, which will result in aliasing. To alleviate distortion introduced by aliasing, an anti-aliasing filter must be used prior to digitisation, and in particular before sampling. In the previous section, low pass filters were used to separate the different frequencies of interest. The second order low pass filter with a cut off frequency of 60 Hz acts as an anti-aliasing filter for the sampling frequency of 200 Hz and the composite signal from the output of the preemphasis stage is sampled at 200Hz.

The FBMs which are contained in frequencies below 2 Hz may be separated by first filtering the sampled composite signal using a Kaiser windowed FIR digital filter [25, 26] with a 2 Hz cut off frequency. After digital filtering, the composite signal is undersampled at 10 Hz sampling frequency prior to FBM processing.

2.4.2. QUANTISATION

Quantisation constrains the sampled signal to conform to one of a finite set of fixed amplitude levels. If there are L quantisation levels, where $L = 2^k$ (k is a positive integer), then the quantisation process can at best resolve half a quantisation step, where a step size is 1/L. The conversion of sampled data from amplitudes of continuous value to a discrete set of amplitudes introduces quantisation noise. The mean-squared-error of quantisation noise $\overline{\epsilon_q^2}$ is given as [27]:

$$\overline{\epsilon_q^2} = \frac{q_l^2}{12} \tag{2.4}$$

Where q_l is the quantisation step.

This brief discussion of quantisation, explains one of the reasons why the preemphasis of FHS was carried out. The dynamic range of a quantiser is proportional to its number of levels, and as FHS are well below FBMs then in order to represent FHS data as well as FBMs, the dynamic range of the quantiser must be more than the signal dynamic range.

2.4.3. ENCODING

The specification of the continuous baseband signal is limited to a discrete set of values. The encoding represents the quantised signal in binary form suitable for computer processing. For L levels of quantisation the number of binary digits required is given by $\log_2 L$.

2.5. SUMMARY

This chapter has presented a brief description of the system layout used prior to digital processing. hence, emphasis has been on the analogue preprocessing. A second order analogue low pass filter was used to extract FBMs from the raw maternal abdominal signals. A second order band pass filter is also used to extract FHS from the raw maternal signal. Preemphasis was applied to the FHS component of the signal. This preemphasis was required to provide a composite FBM and FHS signals with comparable amplitudes of both components. Analogue to digital conversion was discussed and a commercially available digitising oscilloscope, HP 5183T, was used to digitise the analogue signal. The digitised signal was down loaded to a computer for digital processing using an HP 210 desk top computer.

CHAPTER 3

TRANSDUCER FOR DETECTING FETAL BREATHING MOVEMENTS

3.1. INTRODUCTION

It was discussed in early chapters, that movements of organs in the maternal abdomen results in the abdominal wall oscillating in sympathy. Any physical movement or deformation in an organ results in pressure variations in the medium, which will traverse to the surface. These waves will be refracted and reflected at discontinuities in refractive index of the medium. Their arrival at the skin surface will cause it to move. The magnitude of the resulting displacement is dependent on the size of the organ, the intensity of the physical activity and its distance from the surface.

Fetal activities i.e. fetal breathing, heart sounds and body movements may be detected by monitoring maternal abdominal wall displacements. These displacements are typically in the order of micrometers. Accordingly, a sensitive detection method is described which will transduce these activities to a voltage representation. The technique exploits the piezoelectric effect.

This chapter outlines two PVDF transducer designs used to monitor fetal breathing movements, and presents a performance comparison of the two PVDF transducer structures with that of a cantilever design. Finally, typical FBMs moni-

tored using the transducers are presented. It was also found that the same transducers are capable of monitoring fetal heart sounds.

3.2. PIEZO ELECTRICITY

"Piezo" is the Greek for "pressure". Piezoelectric phenomenon refers to the production of electrical charge in response to physical deformation. This phenomenon was first discovered by Pierre and Jacque Curie more than one hundred years ago. They observed that quartz crystals produce an electric charge when subject to physical stress or physical deformation; conversely the crystals changed in physical dimension when exposed to an electric field.

Piezoelectric activities exist in quartz and certain ceramics. These ceramics are polycrystalline in nature and therefore do not possess piezoelectric properties in their natural state. Piezoelectric behaviour is induced in these ceramics by polarising (poling), which aligns the polar axes of the individual crystallites. Poling is achieved by exposing the material to a strong electric field ($\sim$ 500 KV/cm.). Quartz and piezo electric crystals are stiff and brittle in nature, and they lack flexibility. In spite of these drawbacks these materials were used in diverse applications from sonar to medical signal measurement.

Further work was conducted in 1968[28] to investigate the piezoelectric properties in organic materials, such as wood and other biological substances. One of the fascinating findings was that the human skin, bone and tendon are piezoelectric. It was thought that our sense of touch may derive from electric charge on the surface of the skin as a result of touch stimulus, this charge being transferred to the brain by the nervous system. Kocharyan *et al* [28] subjected a number of polar and non-polar polymers to a high poling voltage. They discovered that the higher the polarity of the "unit cell " of the polymer, the higher the "induced" piezoelectric

effect. Polytriflouroethylene, plasticised polyvinyl chloride (PVC) and rigid PVC exhibited the highest piezoelectric activities. Kawai [29] discovered that polyvinylidene flouride could be poled to a level of piezoelectric activity, previously unattainable with other polymers.

3.3. EQUIVALENT ELECTRICAL MODEL FOR THE PVDF TRANSDUCER

In this section an equivalent electrical circuit model of the film is presented. When piezo film has undergone some physical deformation, the charge induced must be processed in order to provide a useful output which will faithfully represent the deformation. To understand the performance of the film, it is helpful to use its basic electrical circuit equivalent.

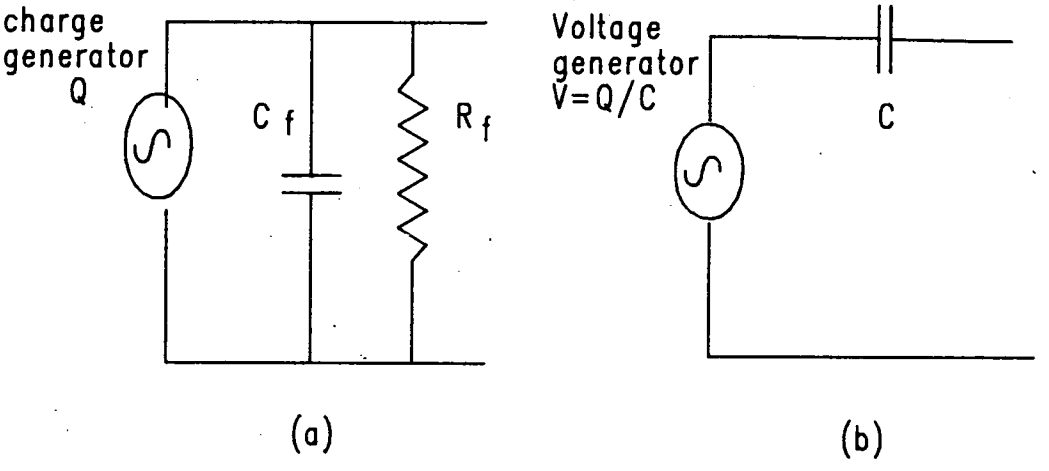

Figure 3.1: Equivalent electric circuit of PVDF piezo film

Figure 3.1(a) shows an equivalent circuit based on a charge generator, film capacitance C_f and internal film resistance R_f. The volume resistivity of the film is 1.5 GΩ-metre and the internal film resistance is very high and can be ignored. Figure 3.1(b) shows the simplified voltage mode equivalent circuit. The open circuit voltage output may be found from the film capacitance, $V = Q/C_f$. This equation indicates that a higher open circuit output voltage may be obtained with the same

applied force by using a thicker film and a smaller surface area (i.e. smaller C_f).

3.4. SIGNAL CONDITIONING

Many different circuits are available to interface electronically with the PVDF film. If the input resistance and input capacitance of the interface circuit is R_i and C_i respectively, then the induced charge on the film plates decays with a time constant given by:

$$time\ constant = R_i\ C_t$$

Where total capacitance is $C_t = C_f + C_i$

In most practical charge amplifier circuits R_i and C_i are very small, which results in a short time constant. This, in turn, makes the film suitable for dynamic measurements rather than static measurements. If the need arises, longer time constants may be obtained by using a circuit with a high input resistance and high input capacitance.

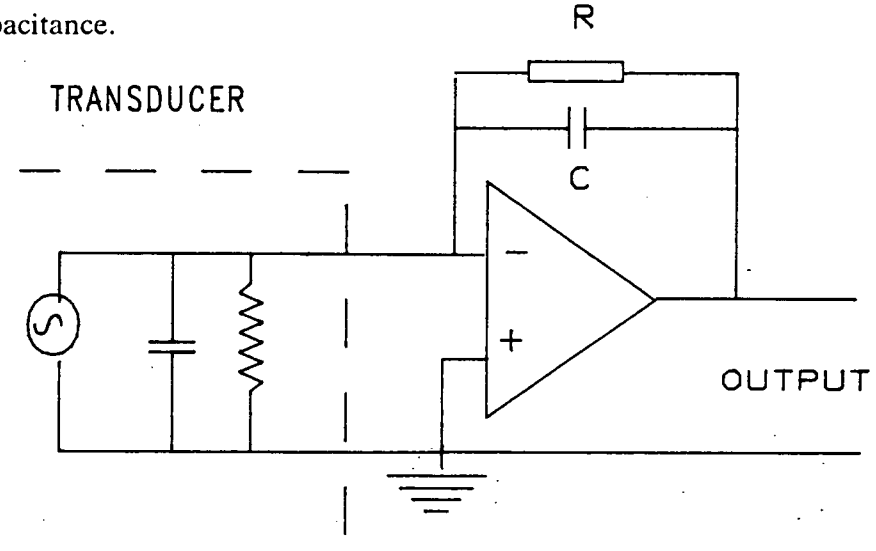

Figure 3.2. The charge amplifier

In small signal applications a charge amplifier is used to convert the induced charge to a voltage output. A charge amplifier is a current operated circuit with zero input resistance. It quickly removes the charge induced on the film plates,

resulting in zero voltage developing across the film. With the induced charge removed as soon as it is developed , and with nothing left across the plates, the system then exhibits time constant of zero seconds. A variety of circuits may be used as charge amplifiers. Figure 3.2 shows the film connected to an operational amplifier based charge amplifier. The transfer function (T.F.) of the above charge amplifier is given by:

$$T.F. = \frac{Voltage\ out}{Charge\ in}$$

$$\frac{V_{out}}{Q_{in}} = \frac{sT}{(sT + 1)} \cdot \frac{1}{c} \qquad (3.1)$$

where T = time constant = R . C for the charge amplifier.

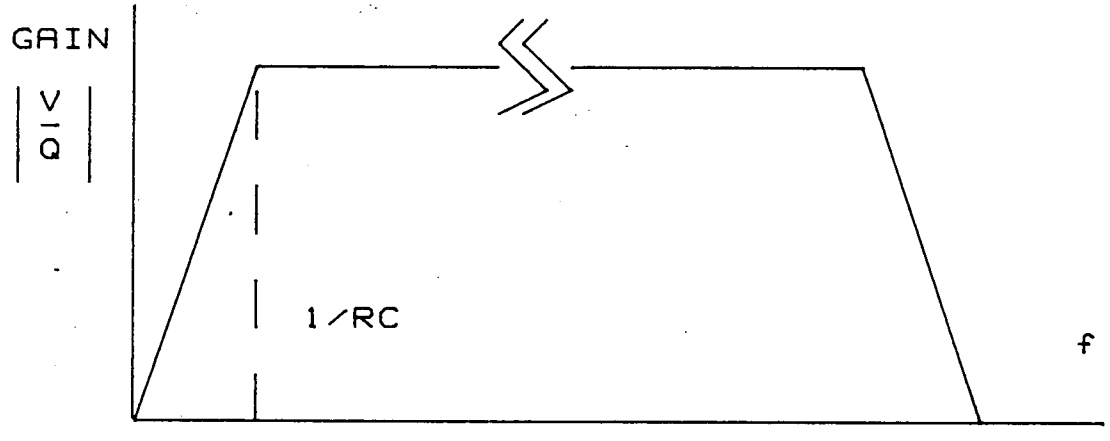

Figure 3.3: Frequency response of charge amplifier.

Figure 3.3 shows the frequency response of the charge amplifier. The low frequency breakpoint of the circuit is controlled by the amplifier and the high frequency breakpoint is controlled by the film's high frequency characteristics.

3.5. PVDF FILM MOUNTING

Any stress applied to a PVDF film will develop charge across the film plates. The stress constant of piezo film is maximum along axis 1 (appendix B), and hence

the PVDF film is used with force applied along this axis. The objective is to maximise the net stress generated and hence the charge developed. Extension along the film's length produces positive charge; compression produces negative charge. Figure 3.4(a) shows a PVDF film in a horizontal position. If the film is deflected then the output due to extension on one surface will cancel the equal and opposite output due to compression on the other surface. The neutral axis of the above case is along the centre of the film.

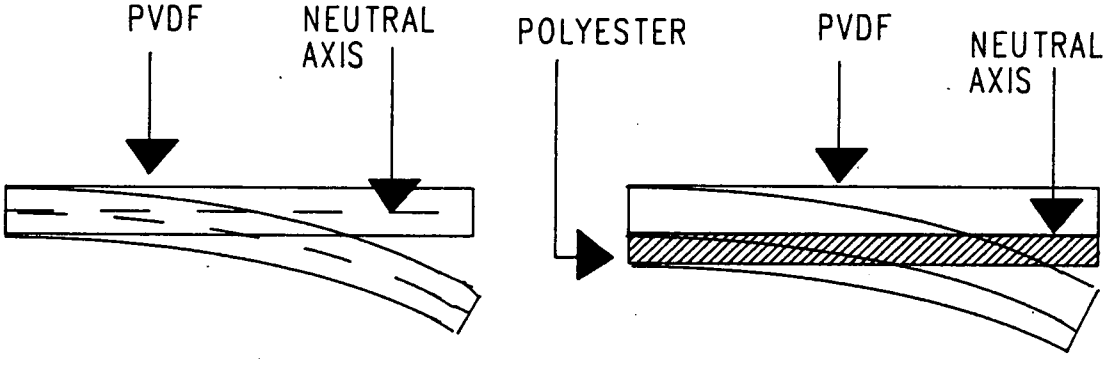

Figure 3.4: Neutral axis for (a) Unlaminated PVDF (b) Laminated PVDF

Mounting the PVDF film onto a polyester strip which does not expand nor contract will result in shifting the neutral axis towards the common surface of the film and the polyester. This results in a net extension or compression when deflected and the output is hence maximised, fig. 3.4(b). Therefore mounting PVDF film on a nonextendible substrate would invariably utilise the pizoelectric properties more effectively. Henceforth, the assumption that the film is laminated using a nonextendible substrate will be made.

Two transducer structures are described and compared below:

A) Horizontally mounted film.

B) PVDF film vertically mounted in a curvature.

Performance comparisons are made of the two types of transducers assuming a 10 μm vertical displacement of the maternal abdominal surface.

3.5.1. HORIZONTALLY MOUNTED FILM.

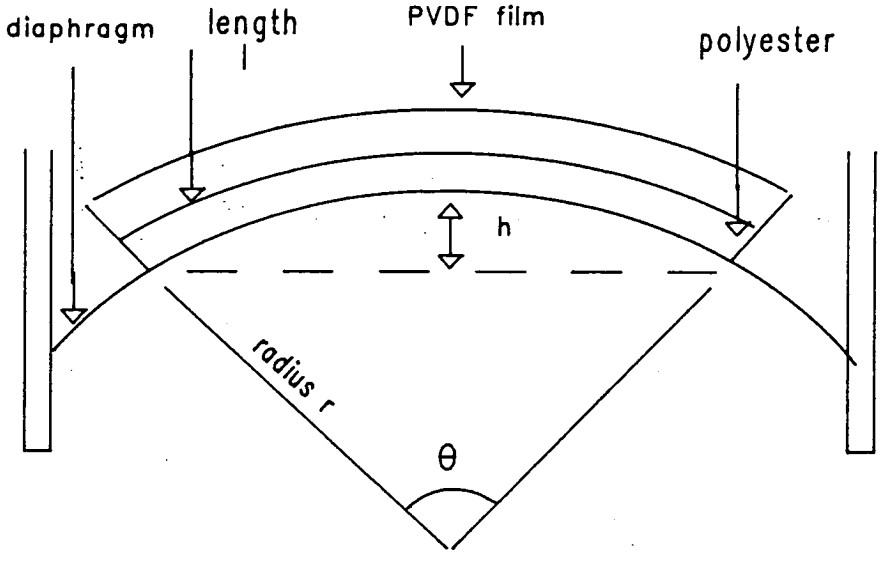

Figure 3.5: Horizontally mounted transducer.

The structure of this transducer is shown in figure 3.5. The film is placed horizontally on a diaphragm comprising an unstretched rubber balloon. As shown in appendix D, it is necessary to evaluate the stress on the film as a first step in the computation of charge developed due to a vertical displacement. When the transducer is strapped down to the maternal abdomen, the diaphragm, will assume a static curvature. From figure 3.5 it can shown that:

$$\Theta = \frac{l}{2r} \tag{3.3}$$

and the radius of the curvature is given by:

$$r = \frac{h}{(1-cos(\Theta))} \tag{3.4}$$

where l is the original length of the film. Using equations (3.3) and (3.4) then:

$$\frac{dr}{dh} = \frac{1}{(1 - cos\Theta - \Theta sin\Theta)} \tag{3.5}$$

Let t be the thickness of the film and let l_s be the length of the outer stretched surface of the film. The length of the outer surface of the film is stretched from l to l_s and hence:

$$\frac{l_s}{(r+t)} = \frac{l}{r} \tag{3.6}$$

Differentiating equation (3.6) yields:

$$\frac{dl_s}{dh} = (-\frac{tl}{r^2}) \cdot \frac{dr}{dh} \tag{3.7}$$

And therefore the change in strain with respect to the height h is given by:

$$\frac{dl_s/l_s}{dh} = \frac{l}{l_s}(-\frac{t}{r^2}) \cdot \frac{dr}{dh} \tag{3.8}$$

The change of the curvature radius with respect to the height, dr/dh, is shown plotted in figure 3.6 as a function of the height h. The function $dl_s/l_s/dh$ is also shown plotted in figure 3.7 as a function of the height h. From figure 3.7 it can be seen that over the expected range of static deflections, i.e. 0 to 0.75 cm, the sensitivity is approximately constant and of the order of 0.15×10^{-2} strain per cm.

Using the design calculation criteria presented in appendix D the charge developed is:

$$q = Cg_{31}\, t\, Y\, strain \tag{3.9}$$

$$\frac{dq}{dh} = Cg_{31}\, t\, Y\, \frac{d(strain)}{dh} \tag{3.10}$$

$$= 0.15 \cdot 10^{-2} \epsilon l\, w\, g_{31}\, Y$$

Where g_{31} is the piezoelectric constant (216×10^{-3}), ϵ is the dielectric constant of the piezoelectric material, w is the width of the film and Y is Young's modulus of elasticity. Using the constants presented in appendix B and using a sensor where l= 4 cm and w =1.5 cm yields:

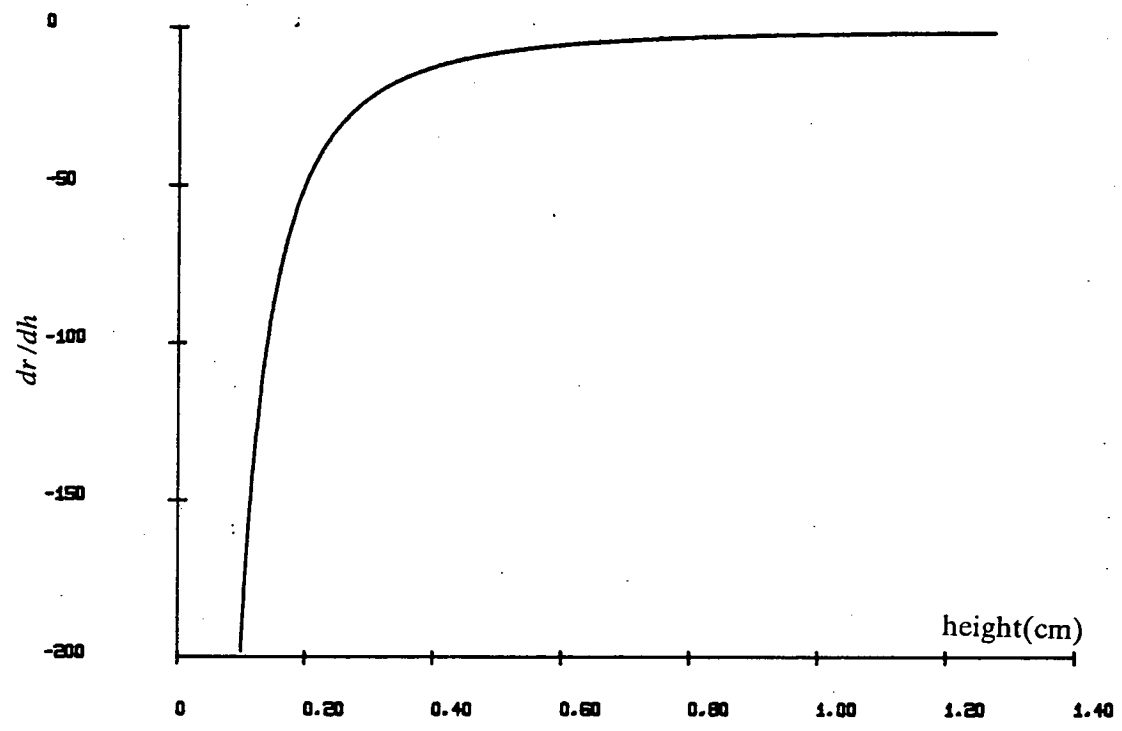

Figure 3.6: First derivative of the radius of curvature with respect to height (cm.) for the horizontal transducer.

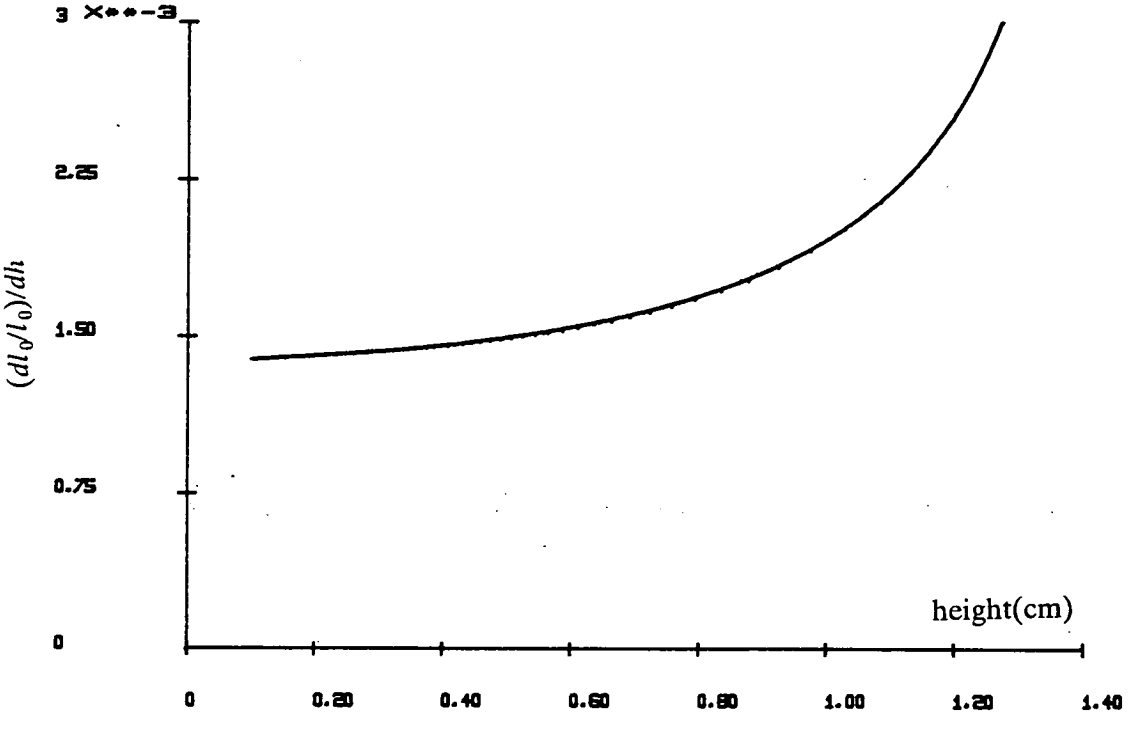

Figure 3.7: First derivative of strain with respect to height (cm.) for the horizontal transducer.

$$\frac{dq}{dh} = 3.21 \times 10^{-8} \ coulombs/cm$$

$$= 3.21 \ pC/micron$$

3.5.2. VERTICALLY MOUNTED FILM.

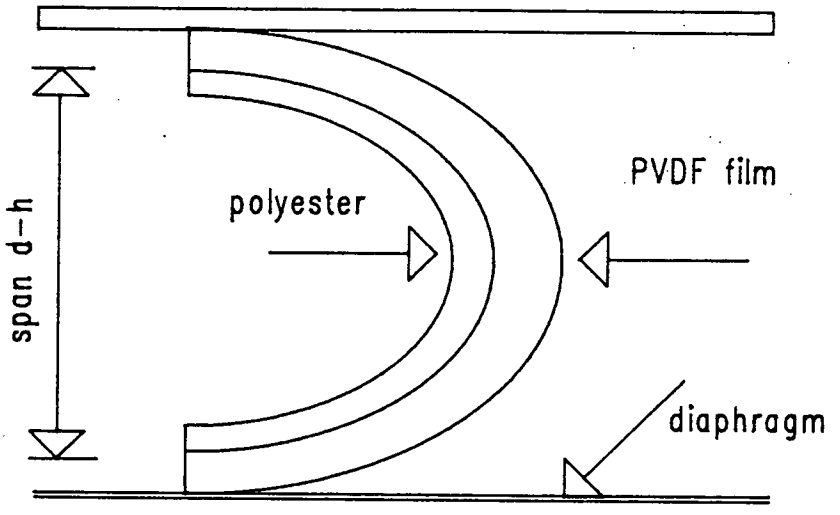

Figure 3.8: Vertically mounted transducer.

The structure of this transducer is shown in figure 3.8. The film is mounted on a substrate which forms a vertical curvature. One end of the film is connected to the metal case; the other end is connected to the diaphragm which also comprises an unstretched rubber balloon. The assumption here is that the curvature of the film will take the shape of a semi-ellipse. Any vertical displacement h, will result a change in the vertical span from d to $d-h$, which will in turn induce a strain on the film surface. The length of the film is of length l, and is fixed onto the neutral axis. The length of the outer stretched surface is:

$$\frac{l_s}{(d-h)} = \frac{l}{d} \tag{3.11}$$

And in a similar manner shown for the horizontal transducer in the previous sec-

tion:

$$\frac{(dl_s/l_s)}{dh} = \frac{2t}{(d-h)(d-h-2t)} \tag{3.12}$$

The sensitivity of the vertical transducer is shown plotted in figure 3.9. It is seen that the strain sensitivity for $d = 2$ cm is of the order of 0.25×10^{-2} strain per cm over the range of 0 to 0.75 cm.

3.6. PERFORMANCE COMPARISON

A film structured to operate as a cantilever possesses linear characteristics to displacement and is independent of static position. The voltage induced for a displacement of δ using a bimorph as a cantilever is:

$$V = \frac{\frac{3}{4} \cdot g_{31} \cdot Y \cdot t^2 \delta}{l^2} \tag{3.13}$$

Using the PVDF film in a bimorph structure and with dimensions, 4 cm. long 1.5 cm wide and 28 μm thick, will develop a charge of 0.6 pC for a vertical displacement of 10 μm. This charge is far less than that developed when using the same dimensions for horizontally mounted and or for the vertically curved transducer, each of which develop a charge in excess of 40 nC. Therefore the performances of both structures surpass that of the bimorph cantilever.

3.7. TRANSDUCER COUPLING

The energy of signals at the maternal abdomen due to fetal biological activities is low, and in monitoring these signals, the maternal wall surface should not be mechanically loaded. Interestingly, the simple Laennec tube stethoscope, which was introduced some hundred years ago does not load the surface. The shortcomings of this latter method was that the stethoscope needed to be close to a powerful source. The transducers designed in this project were found to operate satisfactorily as con-

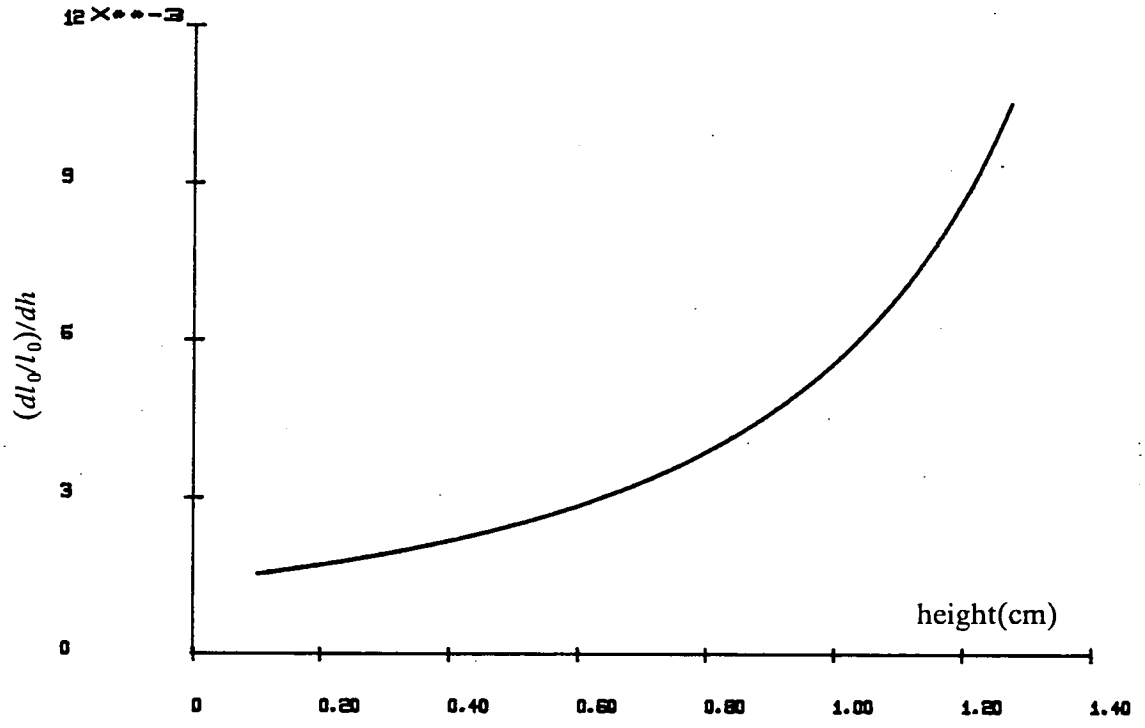

Figure 3.9: First derivative of strain with respect to height (cm.) for the vertical transducer.

tact and non-contact microphones. It is necessary to have an efficient mechanical coupling to ensure more efficient transduction of fetal signals. When the transducer is installed on the patient, the diaphragm is tightened, which exerts some force onto the abdominal wall. The transducers depend on displacement of the surface for their operation, therefore minimum force must be exerted by the transducer and diaphragm for faithful reproduction of the abdominal wall displacements. Talbert and Southall[1] approached this problem by compliance matching. The compliance of the transducer head was adjusted to approach that of the maternal abdomen, 10^{-2} m/N.

The force the transducer exerts on the maternal skin was experimentally measured for varying static positions of the diaphragm. Figure 3.10 shows the displacement versus the force exerted by the diaphragm. The force increases with increasing static position, but not in a linear fashion. Figure 3.11 depicts the compliance of the diaphragm with increasing displacement. The compliance of the diaphragm is far greater than the compliance of the skin(10^{-2} m/N), which indicates that the transducer head does not load the signals arriving to the maternal abdominal wall. The static position of the diaphragm is dependent on the characteristics of the maternal abdominal wall. The biggest factors determining the compliance of the maternal abdominal wall is the obesity of the mother and the gestational age of the fetus. The skin stretches and tightens as the fetus approaches term.

Physiological variabilities, including the above factors, render it pointless to attempt and match compliances, as this is patient dependent. If the transducer's compliance is kept high, and if possible, higher than that of the maternal abdomen then low energy fetal biological activities can be effectively monitored.

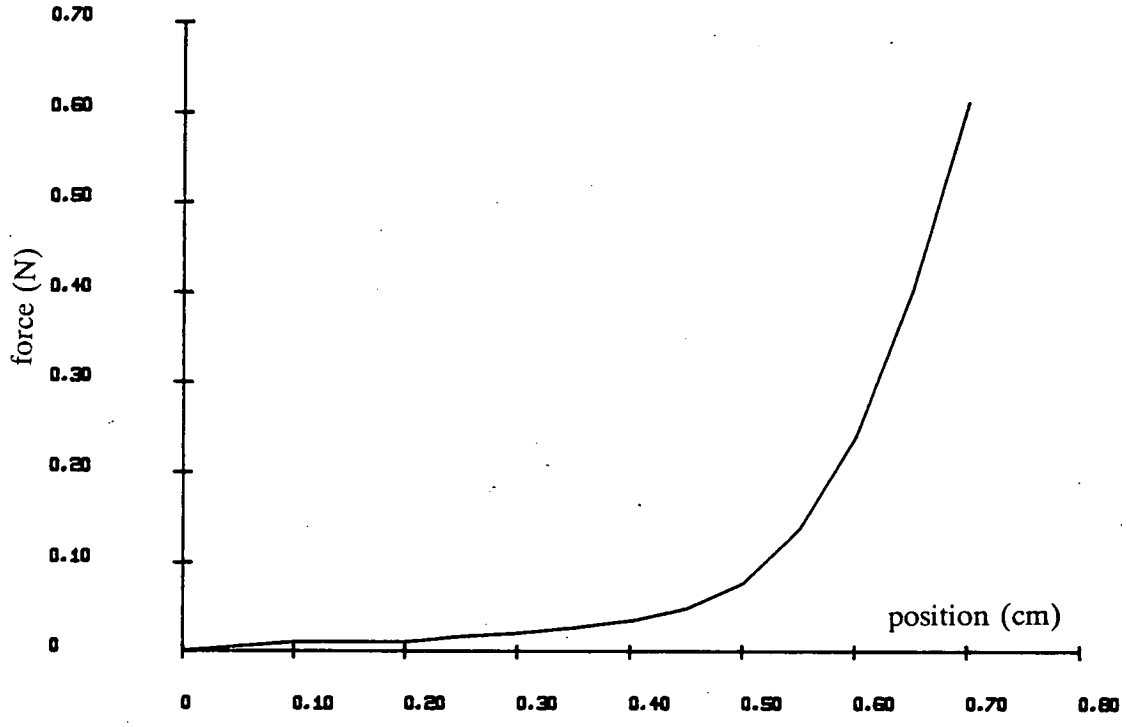

Figure 3.10: Force exerted by diaphragm.

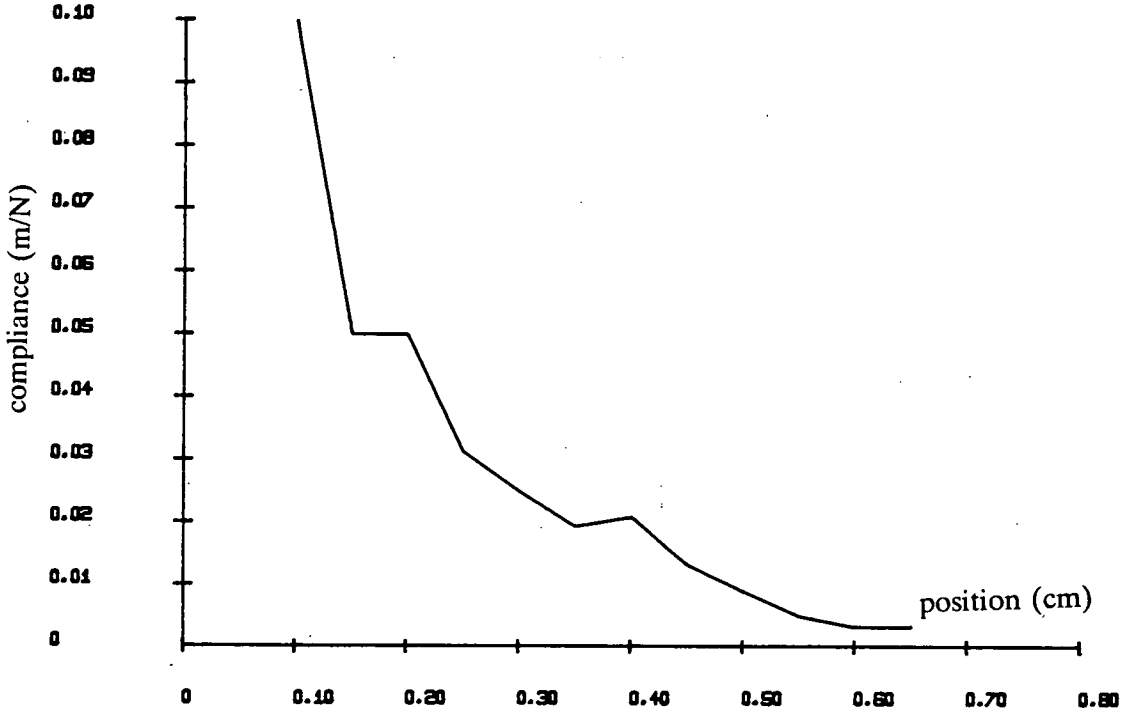

Figure 3.11: Compliance of diaphragm.

3.8. RESULTS

The transducers discussed were used to monitor maternal abdominal wall movements. Figure 3.12 shows maternal abdominal wall displacement. In figure 3.12 both maternal and fetal breathing movements can be seen clearly, but FHS can not be identified. This is due to the fact that the intensity of FHS is about 30 to 40 dB below fetal breathing movements.

Figure 3.13. shows FHS when the maternal abdominal signal is band pass filtered between 40 and 60 Hz and then amplified by a factor of 100. The 10 seconds of data shown in figure 3.13 displays clear fetal heart sounds, with each heart beat comprising two heart sounds. The first heart sound relates to the closure of the mitral and tricuspiad heart valves, while the second heart sound relates to the closure of the pulmonary and aortic valves. There are two large signals which look like spikes in figure 3.13. These two events are related to fetal movements. The detection of fetal movements in the same frequency band as that for FHS has advantages and disadvantages. There is the advantage of the detection of another fetal parameter using the same transducer; while the detection of fetal movements create a problem in the analysis of FHS. Nevertheless as can be seen from figure 3.13., the disrupting effect of the transient fetal (limb) movements is minimal although gross body movements could disrupt severly the FHS signal.

FBM can also be separated by bandpass filtering the MAM signal. In the analogue filtering a second order low pass filter with a cutoff frequency of 2 Hz was used. The resulting filtered waveform would be similar to the unfiltered waveform of figure 3.12 as FHS has relatively low intensity and does not create a significant visual impact on the signal. Passing the digital signal through a bandpass filter with upper and lower cutoff frequencies of 2.0 Hz and 0,5 Hz respectively, this separates FBM signals as shown in figure 3.14. The identification of these signals as a

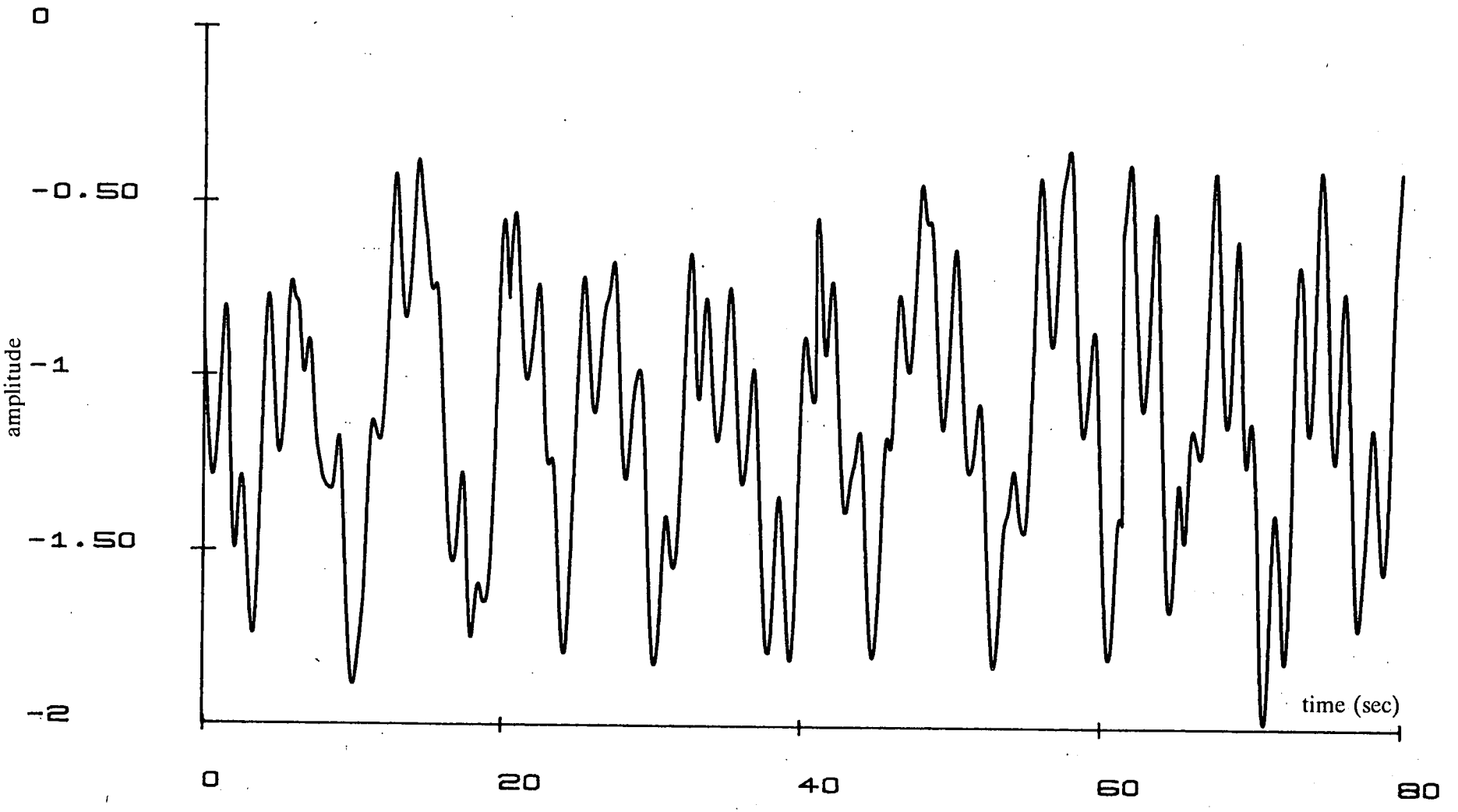

Figure 3.12: MAternal abdominal wall movement (MAM).

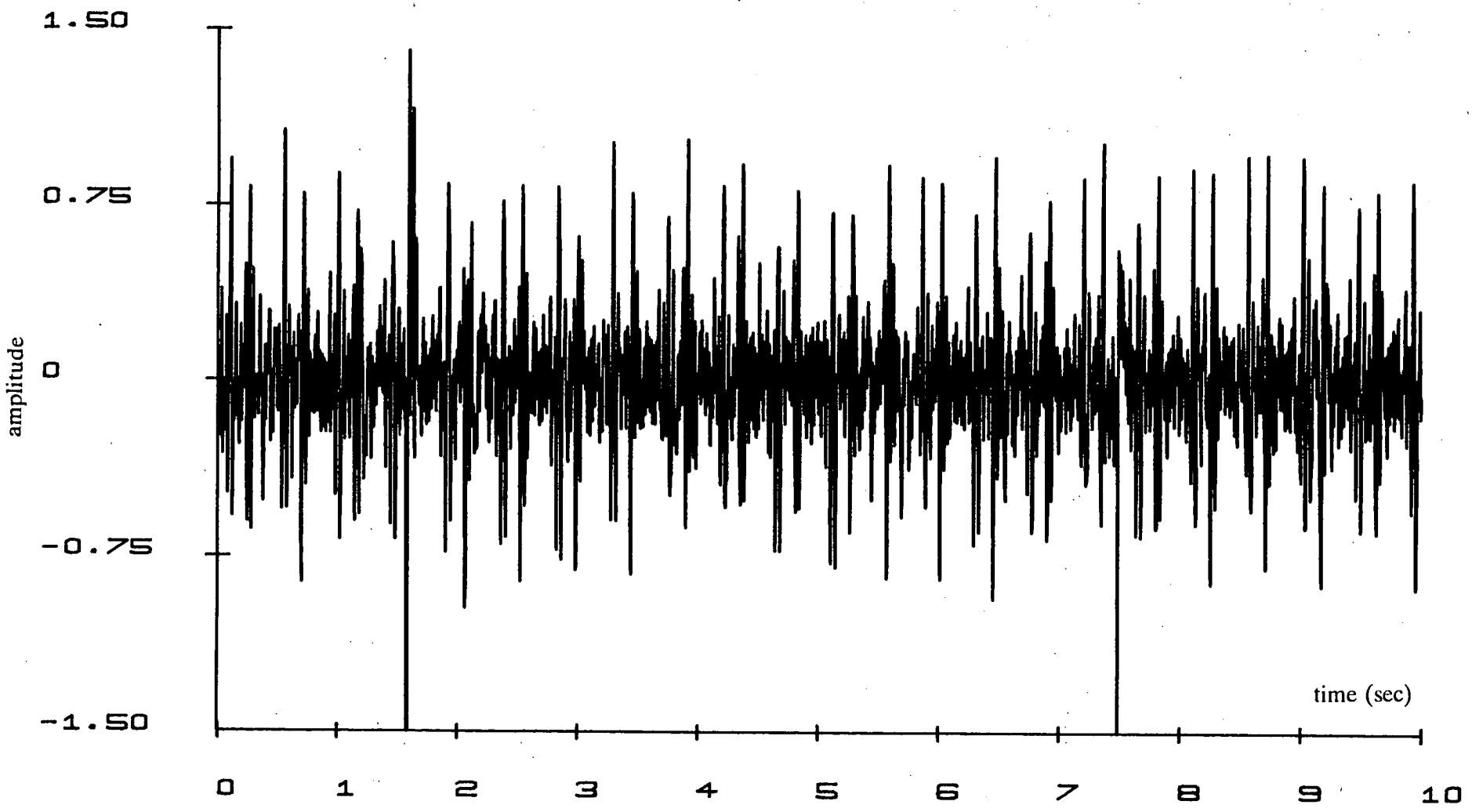

Figure 3.13: Fetal heart sounds (FHS).

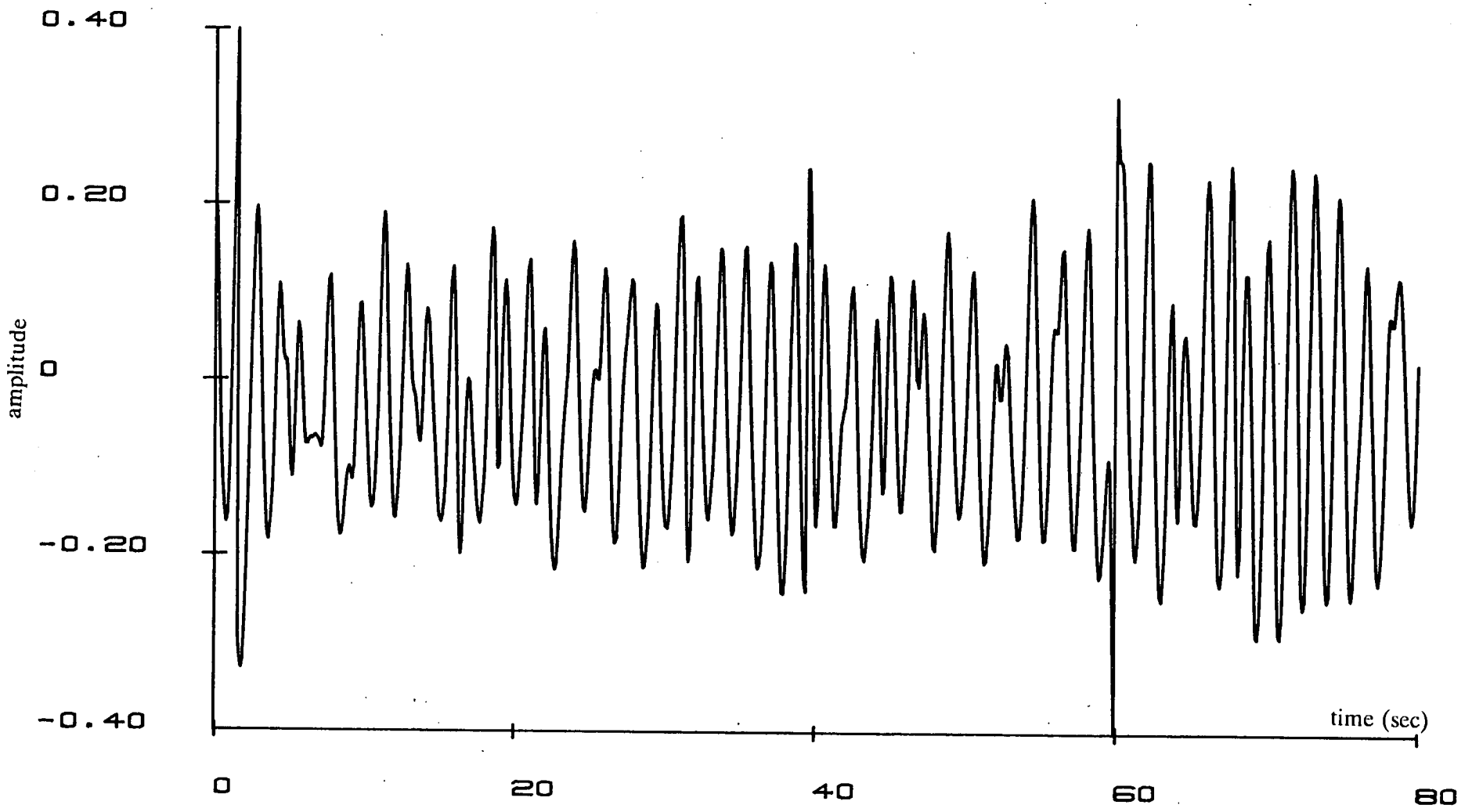

Figure 3.14: Fetal breathing movements (FBM).

representation of FBMs was corroborated by an obstetrician using a real time ultrasound imaging scanner and a switch to indicate every perceived breathing cycle.

3.9. DISCUSSIONS AND CONCLUSIONS

Many assumptions were made in the mathematical modelling of the transducers. The curvature of the horizontally mounted transducer was assumed to form an arc, the vertically mounted transducer was assumed to curve into a semi-elliptic form. The other assumption was that the neutral axis is at the common surface between the substrate and the film. In reality the position of the neutral axis is dependent on the elastic properties [30] of the two materials used. For the neutral axis to be positioned at the common surface of the two materials, then the thickness of the substrate for a given thickness of film is given by:

$$\frac{I_{subs}}{I_{PVDF}} = \frac{Y_{pvdf}}{Y_{subs}} \tag{3.14}$$

where I is the second moment of area of the cross section of each material about the neutral axis, and Y is Young's modulus of elasticity:

$$I = \frac{t^3 \cdot l}{3} \tag{3.15}$$

where l = length and t = thickness.

And the thickness of the substrate is :

$$\left(\frac{t_{subs}}{t_{pvdf}}\right)^3 = \frac{Y_{pvdf}}{Y_{subs}} \tag{3.16}$$

The Young's modulus of the substrate dictates the position of the neutral axis. But since this modulus is more than 20 times greater than that for the PVDF film, the change in length of the common surface will be small, and the opposing charge due to the neutral axis being at some distance from the common surface may be neglected.

The principles of piezo film were introduced and used to develop two different transducer structures for the detection of fetal biological activities observed at the maternal abdomen. The transducers can also be used to detect any displacement whether originating from a biological activity or any other physical phenomenon. The linearity of the transfer characteristic of the transducer for different displacement is presented in figure 3.15, which shows the output in millivolts with respect to displacement measured at 10μm and 100μm.

The transducers were used on a series of 10 patients totalling some sixty thousand breath cycles. In nine of these cases both fetal breathing and heart sounds were detected. In the one case, fetal breathing was detected, but fetal heart sounds were not. This patient was slightly obese and this could have contributed in blocking the low energy fetal heart sounds.

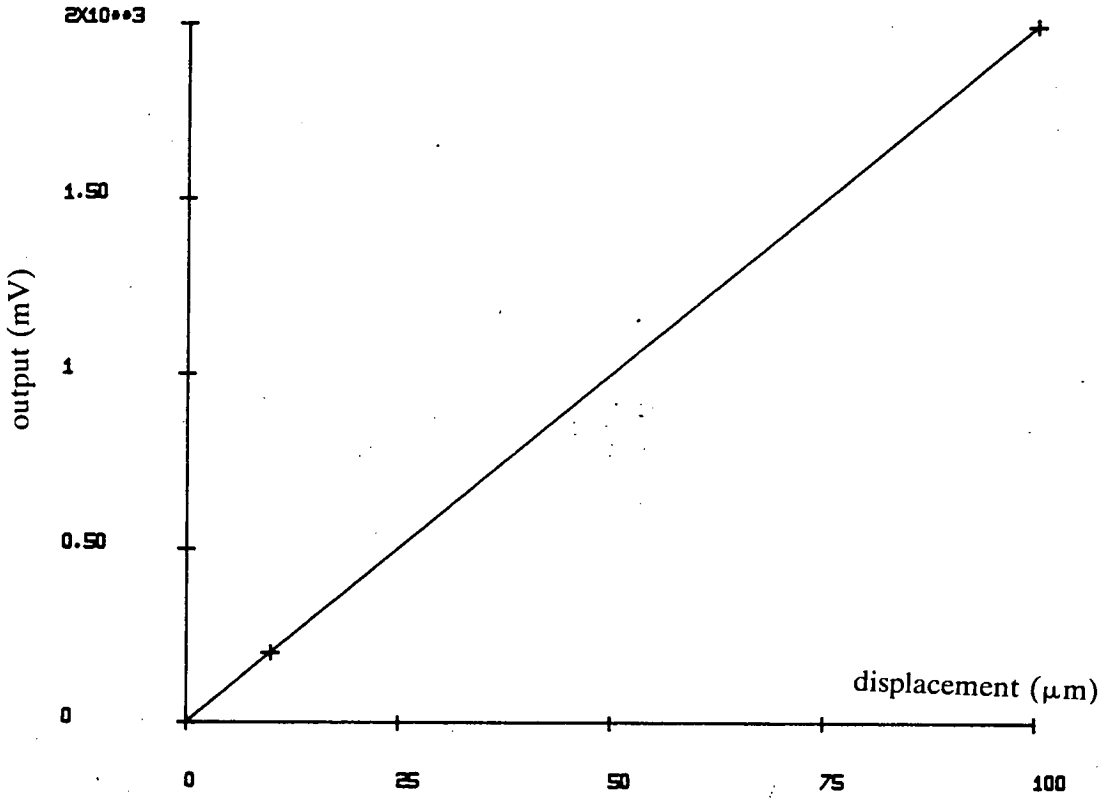

Figure 3.15:Calibration output of vertical transducer showing its linearity with displacement

CHAPTER 4

SPECTRAL ANALYSIS

4.1. INTRODUCTION

FBM data monitored and recorded in chapter 3 must be analysed to estimate FBM rate. In this chapter an outline of the principles of different signal processing algorithms is presented. Traditional spectral estimation, which uses the FFT algorithm is briefly discussed in section 4.2 and its properties outlined. Parametric modelling is presented in section 4.3 and in section 4.4 autoregressive spectral estimation and its properties are discussed. Section 4.5 presents different algorithms used to model and estimate the spectrum of given stochastic signals. These include the gradient LMS, Yule-Walker and the Burg algorithms. Section 4.6 presents a performance evaluation of the LMS and the optimum Burg algorithms. Finally the conclusion is presented in section 4.7.

4.2. TRADITIONAL SPECTRAL ESTIMATION

Spectral estimation of a signal may be achieved using traditional Fourier transforms. The power spectral density (PSD), $P_m(f)$, may be computed by taking the Fourier transform of the autocorrelation of the signal $R_{xx}(m)$[26, 31, 32, 33].

$$P_m(f) = \sum_{m=-M}^{M} R_{xx}(m)\, exp(-j2\pi fm\,\Delta t) \qquad (4.1a)$$

More direct spectral estimation can be obtained by taking FFT of N data,

$x_0, x_1, \ldots, x_{N-1}$, and squaring the coefficients.

$$P_m(f) = \left| \frac{1}{N} \sum_{n=0}^{n=N-1} x_n \exp(-j2\pi mn/N) \right|^2 \qquad (4.1b)$$

The problems of traditional spectral estimation are:

- Spectral resolution

- Spectral leakage

4.2.1. SPECTRAL RESOLUTION

The resolution of a given spectral estimation technique is its ability to discern closely spaced frequency components. In classical spectral estimation a rule of thumb is often used to define resolution:

$$Resolution = \frac{1}{NT} Hz$$

N = Number of the samples in the observation interval

T = Sampling interval.

For the discrete Fourier transform the frequency quantisation is also given by the same equation, which represents the spectral resolution limit at which a single peak in the spectrum may be located. By zero padding to M samples, the resolution due to quantisation interval reduces to $1/MT$. This artificial increase in the number of samples improves the frequency quantisation interval but does not effect the spectral resolution, since the total interval of observation has not changed from $1/NT$.

4.2.2. SPECTRAL LEAKAGE

The spectral leakage encountered in traditional methods can be traced to an assumption about the data outside the measurement interval. In all cases, the data is assumed to have infinite length which is multiplied by some form of a window, whose length is the measurement interval. This forces the data outside the window

to be zero, which is usually not the case. This multiplication in the time domain by a window is equivalent to convolution of the transform of the infinitely long data sequence with the transform of the window function. The transform of a rectangular window is a sinc function, and if the power of the unwindowed signal is concentrated in a narrow bandwidth, then windowing will spread the power into the adjacent frequency regions. This effect is known as leakage.

In addition to degrading the spectral estimates, leakage has detrimental impact on power estimation and on the detectability of multiple sinusoidal components. Sidelobes from adjacent components may add constructively or destructively. In extreme cases a sidelobe from a strong frequency component may mask the main lobe of a weak frequency component, or sidelobes of adjacent frequency components may add to present a significant power, hence inferring the presence of a frequency component which is absent.

So far, rectangular windowing, which is characterised by a sinc function in the frequency domain has been assumed. Other windowing functions may be applied [26, 34, 32] e.g. Hanning window, Hamming window, Bartlett window etc. . These alternate windows, which are tapered, reduce the magnitude of the sidelobes near the main lobe - the signal frequency - at the expense of increasing the width of the main lobe. The resolution defined in the previous section assumes a rectangular window and is the best which can be achieved using N data samples.

In summary, traditional spectral estimation has the following advantages:

(1) Computationally efficient.

(2) Power spectral density (PSD) magnitude is directly proportional to the power of sinusoidal component.

The disadvantages are:

1) Weak signals may be masked by strong signal sidelobes.

2) Introduction of distortion in the spectrum due to sidelobe leakage.

3) Frequency resolution is limited by the available data record length, independent of signal characteristics or signal-to-noise ratio (SNR).

4.3. PARAMETRIC SPECTRAL ESTIMATION

As mentioned in the previous section, classical spectral estimation based Fourier transforms is the most commonly used technique. This technique has shortcomings for short data blocks[32, 34], which make it inadvisable for use in the analysis of FBM signals. These shortcommings may be overcome by employing parametric techniques.

Parametric spectral estimation depends on the assumption that the PSD of the observed signal is the result of passing a white noise sequence through some filtering process. The white spectrum of the noise sequence may be shaped by the filter to provide the PSD of the observed signal. Figure 4.1(a) shows this signal generation model. Equation (4.2a) presents the Wiener-Kintchine equation relating the PSD of the observed signal $P(w)$ to the PSD of the driving noise $P_u(w)$ and the transfer function of the shaping filter $H(e^{(-jwT)})$.

$$P(w) = |H(e^{(-jwT)})|^2 P_u(w) \tag{4.2a}$$

The transfer function of the filter is not always known and in particular, its frequency characteristic is normally the subject of investigation. For example, we modelled the FBM signal as though the generating system is driven by a white noise sequence, and the purpose of the investigation is to determine the transfer function of the respiratory system. This assumption does not have any physical correlate.

In the parametric spectral estimation, the characteristics of the filter shaping the white noise sequence are achieved by passing the observed signal through a

whitening filter. This is shown in figure (4.1b). This whitening process is the inverse of the generating process, and hence, the transfer function of the whitening filter is assumed to be the inverse of the transfer function of the generating filter. Figure 4.1(b) shows a block diagram of the whitening process, and the transfer function $H^{-1}(e^{(-jwT)})$ of the filter which whitens the observed signal to a PSD of $P_e(w)$.

$$P_e(w) = |H^{-1}(e^{(-jwT)})|^2 \; P(w) \tag{4.2b}$$

The motivation for using these parametric techniques is the ability to produce better PSD estimates than by the classical approach previously outlined. Improved spectral resolution independent of data length is the main motivation. In classical techniques, PSD is estimated from a windowed set of data (eq. (4.1b)) or its auto-correlation sequence (ACS) (eq. (4.1a)). The data outside the window is assumed zero, which is an unrealistic assumption that leads to distortion in PSD estimates. *A priori* knowledge of the stochastic process generating the data is often available. This *a priori* knowledge may be used to construct a generating model with more realistic assumptions about the data outside the window. Degrees of improvement in spectral resolution and spectral fidelity over classical technique are determined by the selected model and its ability to fit the measured data.

4.3.1. AUTOREGRESSIVE MOVING AVERAGE (ARMA)

Figure 4.1c illustrates a causal rational model which assumes the time series x_n $\{n = 0,1,2.....N-1\}$ to be generated according to:

$$x_n = -\sum_{k=1}^{k=p} a_k x_{n-k} + G \sum_{m=0}^{m=q} b_m u_{n-m} \tag{4.3}$$

The excitation input time series, u_m, is assumed to be white noise with zero mean and variance one (i.e. the autocorrelation is a unit impulse at zero lag). From eq. (4.3) one can define the "output" of the model at time index n, as linear function of the past p "outputs" and a linear combination of the present and past

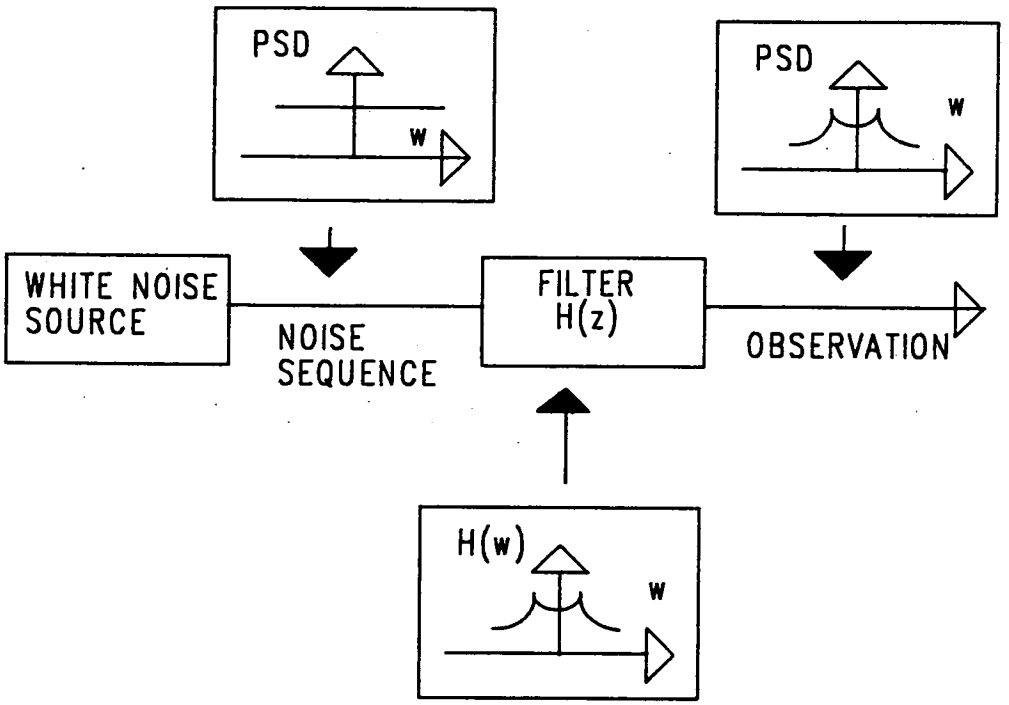

Figure 4.1a: Signal generation model.

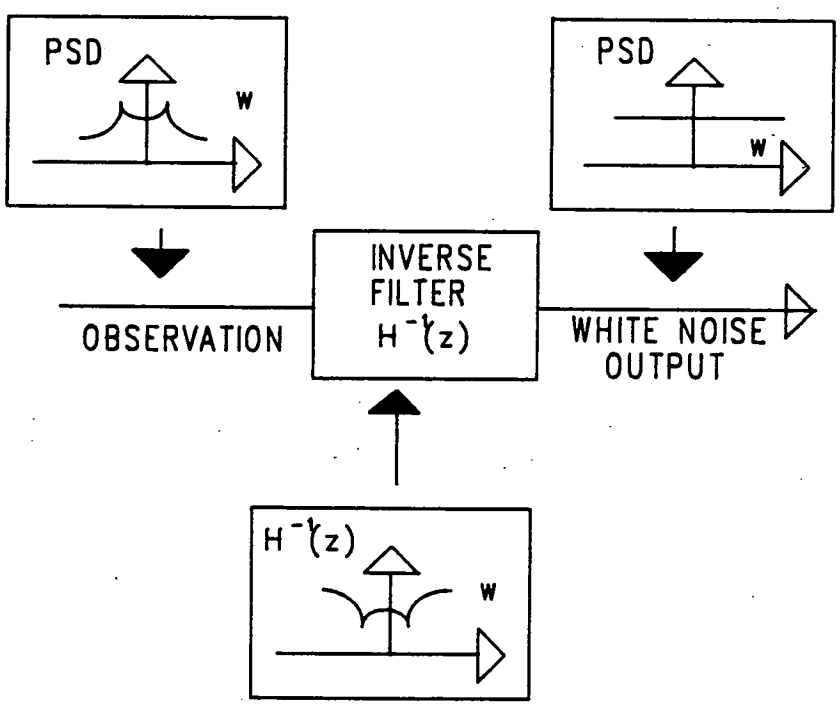

Figure 4.1b: Spectral analysis (whitening model).

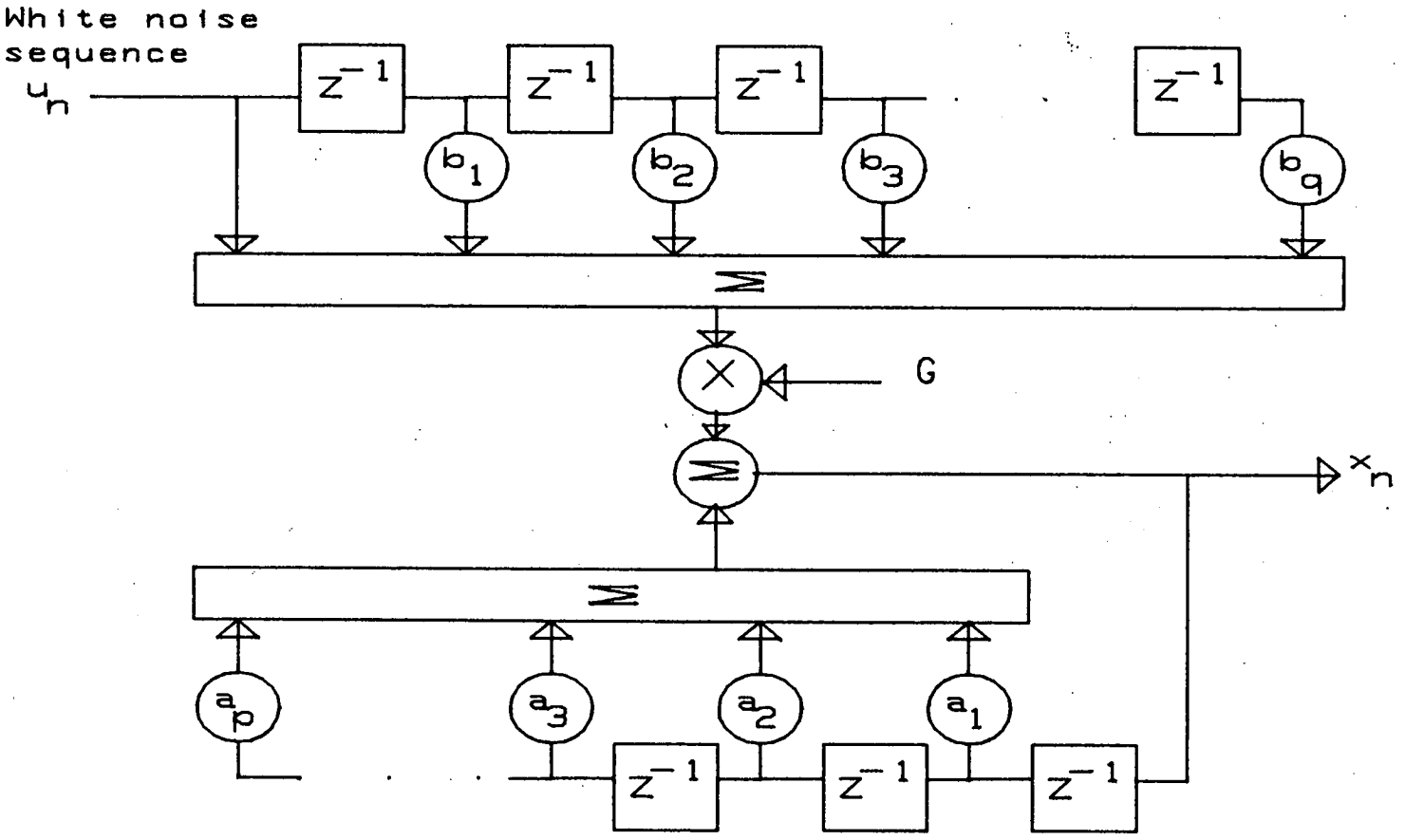

Figure 4.1c: Autoregressive Moving Average process

"input" samples (excitations). The constant G is the gain of the system.

The transfer function of the generating model is given by:

$$H(z) = G\frac{1 + \sum_{m=1}^{m=q} b_m z^{-1}}{1 + \sum_{k=1}^{k=p} a_k z^{-1}} \qquad (4.4)$$

$$= G\frac{B(z)}{A(z)}$$

Where

G = The gain

$B(z)$ = Moving average (MA) transfer function

$$= 1 + \sum_{m=1}^{m=q} b_m z^{-1}$$

$A(z)$ = Autoregressive (AR) transfer function

$$= 1 + \sum_{k=1}^{k=p} a_k z^{-1}$$

For equation (4.4) to be stable and causal, all its poles - determined by $a_1, a_2, a_3, \ldots, a_p$ and all its zeros determined by $b_1, b_2, b_3, \ldots b_q$ - must lie within the unit circle of the Z-plane.

the PSD for a real system is given by[32, 34]:

$$P(z) = H(z)\, H^*(1/z^*)\, P_u(z)$$

$$= \frac{B(z)\, B^*(1/z^*)}{A(z)\, A^*(1/z^*)} P_u(z) \qquad (4.5)$$

Where $P_u(z)$ = autocorrelation of the input driving sequence u_n.

PSD estimates from ARMA models, exhibit both poles due to AR modelling, and zeros due to MA modelling. PSD estimates based on ARMA models display good modelling and resolution properties, but the generation of the optimal AR parameters, a_k, and MA parameters b_m, necessitate the implementation of computationally complex nonlinear algorithms, with the possibility of convergence [32, 34] to

a local minima. There exist, however, relationships [32, 34] between ARMA, MA and AR model parameters. An ARMA or MA process may be represented by an AR process of generally infinite order and conversely an ARMA or an AR process may be represented by MA model of generally infinite order. Therefore an AR process of suitably high order may be a good approximation of an ARMA process[35, 36].

4.4. AR SPECTRAL ESTIMATION

An AR model assumes that a data sequence can be predicted from a weighted sum of its past samples.

$$x_n = -\sum_{k=1}^{k=p} a_k x_{n-k} + u_n \tag{4.6}$$

Where u_n is the driving source with zero mean and variance σ^2, p is the limit of regression (model order of the process), a_k:k=1,2,.....,p is the vector of parametric coefficients.

Rearranging eq. (4.6) and taking the Z-transform:

$$X(z) = \frac{\sigma}{\sum_{k=0}^{k=p} a_k z^{-1}} = \frac{\sigma}{A(z)} \tag{4.7}$$

The PSD of an AR process, $P_{AR}(f)$, can be evaluated on the unit circle[32].

$$P_{AR}(f) = \frac{\sigma^2}{|A(z)|^2_{z=e^{j\omega}}} = \frac{\sigma^2}{\left|\sum_{k=0}^{k=p} a_k \exp(-j\omega k)\right|^2} \tag{4.8}$$

Where a_0 is always 1.

Therefore the AR PSD can be evaluated after estimating the AR parametric

coefficients. Prior to outlining algorithms which estimate these coefficients, some general aspects pertaining to AR modelling are discussed.

(1) **SPECTRAL RESOLUTION:** In section 4.2.1 resolution using traditional spectral estimation was shown to depend totally on the observation interval, with the data outside this interval assumed to be zero. In an AR process no assumption is made for the signal outside the observation interval, and nonzero extrapolation is used for the autocorrelation sequence [32, 34] for lags beyond p. This extrapolation, although damped beyond lag p, effectively provides a long data interval. Resolution of the modelling process for two frequency components with equal powers is shown to depend[34] on signal characteristics and model order.

$$Resolution_{AR} = \frac{1.03}{Tp\,[SNR\,(p+1)]^{0.31}} \tag{4.9}$$

where

T = sampling interval.

p = model order.

SNR = Linear signal-to-noise ratio of a single sinusoid.

(2) **SPURIOUS PEAKS:** It is implied from the previous section that an increase in model order results in an increase in resolution. For particularly low SNR, the use of a high model order results in the modelling of noise as well as signal which then results in spurious spectral peaks which appear to represent nonexistent signal components.

(3) **SPECTRAL LINE SPLITTING:** This occurs when the PSD spectrum represents a single frequency as two distinct adjacent components. This has different causes with different algorithms, but, in general, it is the result of:(1) Too high a model order, as discussed in the previous section.

(2) The data comprise some phase shift along its observation interval. (3) The initial phase of the sinusoidal component is an odd multiple of $\pi/4$. (4) The interval duration is an odd number of quarter wavelength. (5) AR model order is a high percentage of the number of data samples used.

(4) **BIAS OF SPECTRAL ESTIMATES:** An estimate is biased if the estimated expected value differs from the true expected value. All estimates have bias of different quantities. The causes of bias may be attributed to the length and initial phase of the data sequence, in addition to the algorithm used in estimating the parametric coefficients.

(5) **MODEL ORDER SELECTION:** Selection of correct model order is a controversial issue. The best choice of filter model order p is not generally known *a priori*, since the exact AR process generating the data is not generally known *a priori*. Some criterion is required to indicate the correct choice of model order. Too low a model order results in a smoothed spectral estimate; too high a model order results in an increase in resolution which could introduce spurious peaks into the spectrum. Akaikie [37, 32, 34] and Parzen [32, 34, 38] have proposed postulates for correct model order selection, which are based on the prediction error criterion. Ulrych and Clayton[39] showed that for short data blocks, the performances of these criteria were unsatisfactory. Ulrych and Ooe[40] determined, experimentally, that model order selection of 1/3 to 1/2 of the data block length would perform satisfactorily. This presumes that the data block is itself a good representation of the signal.

(6) **NOISY AR PROCESS:** Noisy observations produce smoothed AR PSD estimates[32, 31], which manifests itself as bias and limits the practical

utility of AR PSD estimation. An AR process embedded in white noise is an ARMA process, and therefore, the bias due to smoothing in an AR model could be reduced if large model orders were used, but choosing a high model order may result in spurious peaks, as discussed earlier. Choice of model order according to Ulrych and Ooe[40] provide acceptable PSD estimates. In high noise conditions, the traditional periodogram method can be superior to AR modelling[32].

4.5. AUTOREGRESSIVE ALGORITHMS

In order to develop the AR PSD, the parametric coefficients of the model (eq. 4.8) must be estimated. As stated earlier, the current sample of an AR process may be estimated from a linear combination of its past p samples.

$$\hat{x}_n = -\sum_{k=1}^{p} a_k x_{n-k} + u_n \tag{4.10}$$

An error signal is generated due to the difference between the estimated value, $\hat{x}_n$, and the true value x_n.

$$\begin{aligned} e_n &= x_n - \hat{x}_n \\ &= x_n + \sum_{k=1}^{p} a_k x_{n-k} - u_n \end{aligned} \tag{4.11}$$

In a random process, The mean-squared-error (MSE), ξ is:

$$\begin{aligned} \xi &= E\{e_n^2\} \\ &= E\{(x_n + \sum_{k=1}^{p} a_k x_{n-k} - u_n)^2\} \end{aligned} \tag{4.12}$$

Where $E\{*\}$ denotes the expectation function.

The parametric coefficients are estimated for minimum mean-squared-error (MMSE) in eq. (4.12)

There are a number of algorithms which estimate these parametric coefficients. These may take a sequential form[41, 42, 43, 44], or block form[31, 45, 34]. The

following algorithms are discussed in the proceeding sections:

1 Least-mean-squared (LMS) gradient algorithm.

2 Yule-Walker algorithm.

3 Burg algorithm.

4 Weighted Burg algorithms:

(a) Energy weighted.

(b) Optimum weighted.

(c) Data-adaptive weighted.

4.5.1. LEAST-MEAN-SQUARED (LMS) GRADIENT ALGORITHM

This is one of a number of algorithms that may be used for system identification and AR coefficient estimation, and is one of the simplest to implement. Expressing eq. (4.11) in matrix form we have:

$$\xi = E\{(x_n - \sum_{k=1}^{p} a_k x_{n-k})^2\} \tag{4.13}$$
$$= E\{(x_n - \mathbf{A}_n^T \mathbf{X}_n)^2\}$$

Where $\mathbf{A}_n$ is the coefficient vector, $\mathbf{A}_n^T = [a_{n1}, a_{n2}, \ldots, a_{np}]$ and $\mathbf{X}_n$ is the data vector of past p samples, $\mathbf{X}_n^T = [\, x_{n-1}, x_{n-2}, \ldots, x_{n-p} \,]$. Expanding eq. (4.13)

$$\xi = E\{x_n^2\} + \mathbf{A}_n^T E\{\mathbf{X}_n \mathbf{X}_n^T\}\mathbf{A}_n - 2E\{x_n \mathbf{X}_n^T\}\mathbf{A}_n \tag{4.14}$$
$$= E\{x_n^2\} + \mathbf{A}_n^T \mathbf{R} \mathbf{A}_n - 2\mathbf{P}\mathbf{A}_n$$

Where $\mathbf{R} = E\{\mathbf{X}_n \mathbf{X}_n^T\}$ = Autocorrelation matrix.

$\mathbf{P} = E\{x_n \mathbf{X}_n^T\}$ = Cross correlation vector.

For a stationary stochastic signal, the MSE is a quadratic function of $\mathbf{A}_n$, the parametric coefficients. In the gradient method, the first derivative of the error performance surface, ξ, is minimised to get the optimal solution of $\mathbf{A}^*$.

$$\nabla = \frac{\partial \xi}{\partial \mathbf{A}_n} = 2\mathbf{R}\mathbf{A}_n - 2\mathbf{P} \qquad (4.15)$$

$$= 0$$

If $\mathbf{R}$ is non singular, the optimal solution is:

$$\mathbf{A}^* = \mathbf{R}^{-1}\mathbf{P} \qquad (4.16)$$

Equation (4.16) is the Wiener optimal solution for the coefficients vector (weights).

In the method of steepest descent, a recursive estimate of the filter coefficients is given by[42]:

$$\mathbf{A}_{n+1} = \mathbf{A}_n + \mu(-\nabla_n) \qquad (4.17)$$

where ∇_n = The gradient of iteration n.

μ = A constant which regulates the step size.

Thus an estimate of the gradient ∇_n is required. This involves computation of the autocorrelation vector (eq. 4.16). The LMS algorithm takes e_n^2 as an estimate of ξ_n. This makes the estimate of the gradient $\hat{\nabla}_n$:

$$\hat{\nabla}_n = \frac{\partial(e_n^2)}{\partial \mathbf{A}_n} = 2e_n \frac{\partial \mathbf{e}_n}{\partial \mathbf{A}_n}$$

$$= -2\mathbf{e}_n\mathbf{X}_n \qquad (4.18)$$

Hence, for the LMS algorithm, the recursive estimate of the filter coefficients is given by:

$$\mathbf{A}_{n+1} = \mathbf{A}_n + 2\mu\mathbf{e}_n\mathbf{X}_n \qquad (4.19)$$

The convergence of eq. (4.19) towards the Wiener optimal solution is only guaranteed [42] if the input data is a stochastic stationary signal and provided the adaptation gain μ is in the range:

$$0 < \mu < \frac{1}{\lambda_{max}} \qquad (4.20)$$

Where λ_{max} is the largest eigenvalue of the autocorrelation matrix **R**. μ has the dimension of the reciprocal signal power. Linkens [46] and Griffiths[47] have presented an adaptive method for computing the gain μ:

$$\mu = \frac{\alpha}{tr(\mathbf{R})} = \frac{\alpha}{p\ r(0)} \qquad 0 < \alpha < 2 \tag{4.21}$$

Where tr(**R**) is the trace of the autocorrelation matrix, p is the filter length and r(0) is the mean power of the data in the filter. The selection of α and subsequently μ determines the convergence rate of the LMS algorithm. The gain μ also determines the misadjustment M which is defined as:

$$M = \frac{\text{Excess MSE}}{\text{minimum MSE}}$$
$$= \mu\ tr(\mathbf{R}) \tag{4.22}$$

The adaptation time constant which is measured in iterations, is defined as[47, 46, 42] as:

$$\tau_a = \frac{-1}{ln(1 - \frac{\alpha}{p})} \tag{4.23}$$

Therefore by choosing the required adaptation time constant and the filter length p, α is given by:

$$\alpha = p(1 - e^{-1/\tau_a}) \tag{4.24}$$

The adaptive choice of α and hence the gain constant μ, guarantees the convergence of the LMS and greatly improves the robustness of the algorithm.

4.5.2. YULE WALKER ALGORITHM

Differentiating eq. (4.11) with respect to the coefficients, and setting the derivative to zero gives:

$$\xi = \sum_n (x_n + \sum_{k=1}^{k=p} a_k x_{n-k})^2 \tag{4.25}$$

$$\frac{\partial \xi}{\partial a_i} = 2\sum_n (x_n + \sum_{k=1}^{k=p} a_k x_{n-k}) x_{n-i} \tag{4.26}$$

$$= 0 \qquad 1 < i \leq p$$

$$R_{xx}(i) = \sum_n x_n x_{n-i} = -\sum_{k=1}^{k=p} a_k \sum_n x_{n-k} x_{n-i} \tag{4.27}$$

Solving eq. 4.26 gives:

$$R_{xx}(i) = -\sum_{k=1}^{k=p} a_k R_{xx}(i-k) \quad \text{for } i > 0 \tag{4.28a}$$

By substituting eq. (4.27) into the expanded form of eq. (4.25)

$$R_{xx}(0) = -\sum_{k=1}^{k=p} a_k R_{xx}(k) + \kappa \quad i = 0 \tag{4.28b}$$

If the noise is white and gaussian then κ is its variance (σ^2).

Equations (4.28) are the Yule-Walker equations. The coefficients can be estimated by solving a set of p linear equations. The Gauss elimination method for solving eq. 4.28 requires $p^2/3 + O(p^2)$ operations. If the summation in eq. (4.27) is taken over a finite data interval, then this would result in the covariance expression and an efficient solution for the coefficients could be achieved using the Cholesky decomposition, which requires $p^2/6 + O(p^2)$ operations. The summation in eq. (4.27) was taken over an infinite duration and the coefficients were expressed in terms of the autocorrelation function of the data. In practice, analysis is carried out using data of finite duration. The finite duration case is equivalent to having data of infinite duration which is multiplied by a window whose length is the observation interval N.

For a stationary stochastic signal, the autocorrelation matrix is Hermitian and Toeplitz[34, 32, 45, 48, 31]. The matrix representation of equations (4.28) is:

$$\begin{bmatrix} R_{xx}(0) & R_{xx}(-1) & \cdots & R_{xx}(-p) \\ R_{xx}(1) & R_{xx}(0) & \cdots & R_{xx}(-(p-1)) \\ R_{xx}(2) & R_{xx}(1) & \cdots & R_{xx}(-(p-2)) \\ \cdot\cdot & \cdot\cdot & \cdots & \cdot\cdot \\ \cdot\cdot & \cdot\cdot & \cdots & \cdot\cdot \\ \cdot\cdot & \cdot\cdot & \cdots & \cdot\cdot \\ R_{xx}(p) & R_{xx}(p-1) & \cdots & R_{xx}(0) \end{bmatrix} \begin{bmatrix} 1 \\ a_1 \\ a_2 \\ \cdot\cdot \\ \cdot\cdot \\ \cdot\cdot \\ a_p \end{bmatrix} = \begin{bmatrix} \sigma^2 \\ 0 \\ \cdot \\ \cdot \\ \cdot \\ 0 \end{bmatrix} \tag{4.29}$$

The Levinson-Durbin algorithm[31, 32, 34, 45, 48, 33] provides an efficient order recursive solution to the Yule-Walker eq. (4.29) requiring $O(p^2)$ operations only. The Levinson-Durbin algorithm solves for coefficients of order p from the predictor coefficients of order $(p\text{-}1)$. Hence, a byproduct of the Levinson-Durbin solution for model order p is a set of coefficients and residual predictor output power for the lower model orders. If $a_m[n]$ denotes the n^{th} coefficient of the m^{th} order linear predictor then:

$$a_m[n] = a_{m-1}[n] + a_m[m]a^*_{m-1}[m-n] \qquad (4.30)$$
$$m = 1,2,\ldots,p$$
$$n = 1,2,\ldots,m$$

The superscript ($*$) denotes complex conjugate and:

$$a_m[m] = \frac{-\sum_{k=0}^{k=m-1} a_{m-1}[k]R_{xx}[m-k]}{\sigma^2_{m-1}} \qquad (4.31)$$

The procedure for solving eq. (4.30) and (4.31) up to model order p is as follows:

$$\sigma_0^2 = R_{xx}[0]$$
$$a_{m-1}[0] = 1 \qquad m = 1,2,\ldots,p$$
$$a_1[1] = -\frac{R_{xx}[1]}{R_{xx}[0]}$$
$$\sigma_1^2 = (1 - a_1^2[0])R_{xx}[0]$$
$$\sigma_m^2 = (1 - a_m^2[m])\sigma^2_{m-1}$$

In an AR process, the residual error power, σ_m^2, is progressively reduced as it approaches the correct model order p. For the AR process to be stable and minimum phase, the coefficients $a_m[m]$ must satisfy

$$|a_m[m]| \leq 1 \qquad m = 1,2,\ldots,p \qquad (4.32)$$

Lattice formulation of the prediction error filter is also possible, fig. 4.2. Two prediction errors are presented, the forward error ef_m and the backward error eb_m.

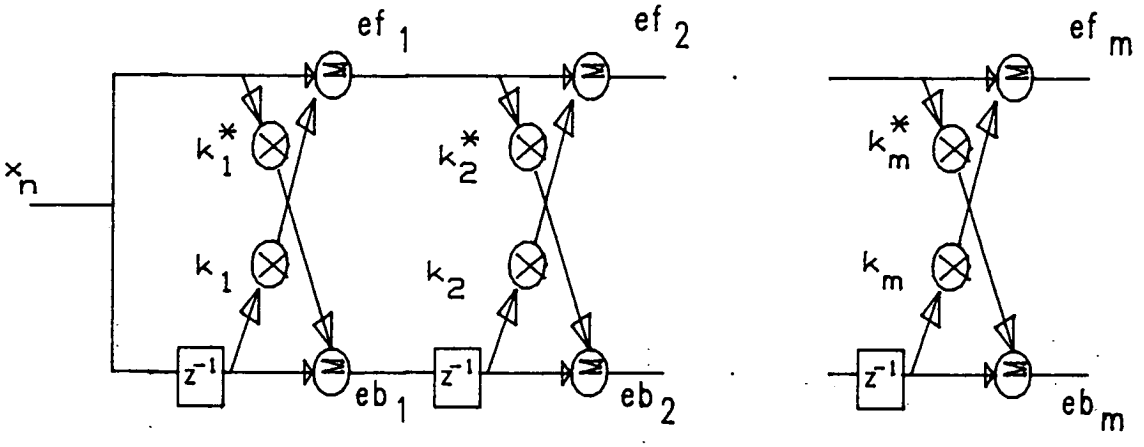

Figure 4.2: Lattice filter structure.

The latter attempts to predict the sample $x[n-m]$ form knowledge of samples $x[n-m+1]$, $x[n-m+2]$,.....,$x[n]$

$$ef_m[n] = x[n] + \sum_{k=1}^{k=m} a_m[k]x[n-k] \tag{4.33}$$

which reduces to:

$$ef_m[n] = ef_{m-1}[n] + a_m[m]eb_{m-1}[n-1] \tag{4.34}$$

$$eb_m[n] = x[n-m] + \sum_{k=1}^{k=m} a_m[k]^* x[n-m+k] \tag{4.35}$$

In a similar fashion eq. (4.35) can be reduced to:

$$eb_m[n] = eb_{m-1}[n-1] + a_m^*[m]ef_{m-1}[n] \tag{4.36}$$

The intermediate coefficients, $a_1[1],a_2[2],\ldots,a_m[m]$ are termed the reflection coefficients from transmission theory, or PARCOR (PARtial CORrelation) coefficients k[m]. These coefficients are considered as the negative partial correlation between x_n and x_{n+m} with the intermediate values $x_{n+1},\ldots,x_{n+m-1}$ being fixed.

$$k[m] = a_m[m] \tag{4.37}$$

4.5.3. BURG ALGORITHM

The Burg algorithm uses the lattice structured filter discussed in sec. 4.5.2 where the forward and backward errors and total error power P_e are expressed as:

$$ef_m[n] = ef_{m-1}[n] + k[m]eb_{m-1}[n-1] \tag{4.38}$$

$$eb_m[n] = eb_{m-1}[n-1] + k^*[m]ef_{m-1}[n] \tag{4.39}$$

Where k^* denotes the complex conjugate of the reflection coefficient.

$$P_e = E\{ef^2[n] + eb^2[n]\} \tag{4.40}$$

Burg minimised eq. (4.40) with respect to the PARCOR coefficients and found the solution for $k[m]$[32, 33]

$$k[m] = \frac{2\,E\{ef_{m-1}[n]\,eb_{m-1}[n-1]\}}{E\{ef^2_{m-1}[n] + eb^2_{m-1}[n-1]\}} \tag{4.41}$$

$$= \frac{-2\sum_{n=m}^{N-1} ef_{m-1}[n]eb_{m-1}[n-1]}{\sum_{n=m}^{n=N-1}(|ef_{m-1}[n]|^2 + |eb_{m-1}[n-1]|^2)} \tag{4.42}$$

The procedure for solving the Burg algorithm is to initialise the forward and backward errors:

$$ef_0[n] = eb_0[n] = x[n] \quad n = 0,1,2,\ldots,N-1$$

and then solve recursively for m = 1 to p (equations 4.38 and 4.39) using the reflection coefficient given by eq. (4.42).

The Burg algorithm may be viewed as computing the PARCOR coefficient of the lattice filter by taking the harmonic mean of the forward and backward prediction error. Other functions of error power are possible eg. geometric mean and arithmetic mean, but the Burg algorithm is guaranteed to produce a stable minimum phase filter[32, 34]

4.5.4. WEIGHTED BURG ALGORITHMS.

The Burg algorithm discussed previously exhibits line splitting[49, 32, 34] and some bias in estimation of sinusoidal frequencies. The Burg algorithm may be regarded as windowing the squared error power by a rectangular function $W_m[n]$. The total error power P_e using a window is given by:

$$P_e = E\{W_m[n]\,(ef^2[n] + eb^2[n])\} \tag{4.43}$$

Which changes the estimate of the reflection coefficient (eq. (4.42)) to:

$$k[m] = \frac{-2\sum_{n=m}^{n=N-1} W_{m-1}[n]ef_{m-1}[n]eb_{m-1}[n-1]}{\sum_{n=m}^{n=N-1} W_{m-1}[n](ef^2_{m-1}[n] + eb^2_{m-1}[n-1])} \tag{4.44}$$

Where $W_{m-1}[n] = 1/N$.

Variations of the above windowing function have been proposed by many researchers to mitigate estimation bias and line splitting. Swingler [49] showed that a Hamming window can reduce the estimation bias:

$$W_m[n] = 0.54 - 0.46\cos\left[\frac{2\pi(n-m)}{N-m} + \frac{\pi}{N+m}\right] \tag{4.45}$$

$$n = m, m+1, \ldots, N-1$$

Scott[50] proposed a data adaptive window which uses the power in the prediction error filter in order to weight the forward and backward PARCOR coefficients separately.

$$\text{Forward weights} = Wf_m[n] = \sum_{i=1}^{i=m} x^2_{n+m-i} \tag{4.46}$$

$$\text{Backward weights} = Wb_m[n] = \sum_{i=1}^{i=m} x^2_{n+i} \tag{4.47}$$

$$\text{for} \quad n = m, m+1, \ldots, N-1$$

The final reflection coefficients are obtained as the harmonic mean of the forward and backward PARCOR coefficients:

Kaveh[51] proposed a parabolic window, which is close to the theoretical optimum. This windowing function alleviates spectral splitting and also minimises frequency estimation bias. The weighting function is given by:

$$W_m[n] = \frac{6(n-m+1)(N-n)}{(N-m)(N-m+1)(N-m+2)} \qquad (4.48)$$
$$n = m, m+1, \ldots N-1$$

The weights can be recursively computed as:

$$W_m[m-1] = 0$$
$$W_m[m] = (N-m)\frac{\lambda_m}{2}$$
$$W_m[n] = 2W_m[n-1] - W_m[n-2] - \lambda_m \quad n = m+1, .., N-1$$
$$\lambda_m = \frac{12}{(N-m)(N-m+1)(N-m+2)}$$

Helme[52] proposed data adaptive weighting which depends on the common data energy in the forward and backward prediction errors.

$$W_{m-1}[n] = \sum_{k=n-m+1}^{k=n-1} |x_k|^2 \qquad (4.49)$$

4.6. PERFORMANCE EVALUATION

In this section the relative performance of the gradient LMS and the optimum tapered Burg algorithms are presented. The gradient LMS algorithm is one of the most popular algorithms used for system identification and channel equalisation. This popularity arises from its relative simplicity. In the analysis of LMS[42, 53, 43] the convergence time is a function of the eigenvalues of the autocorrelation matrix. For the LMS to converge, the adaptation gain μ must be less than the inverse of the largest eigenvalue[42, 47, 53]. Therefore, the greater the eigenvalue spread, the more coloured the input signal and the longer the algorithm takes to converge to the solution. The OTB algorithm is more computationally complex. Similar to the LMS, the autocorrelation matrix for the OTB is assumed to be Toeplitz and

semidefinite, but its performance is not dependent on the eigenvalue spread of the input autocorrelation matrix. OTB is a block data algorithm which models the input signal using a lattice filter.

The frequency tracking of the LMS and OTB algorithms are evaluated below using two types of nonstationary signals:

Type 1: **A Frequency modulated signal (FM).** Carrier frequency f_c = 1 Hz, FM modulating frequency $f_{m(FM)}$ = 0.1 Hz and frequency deviation Δf = 0.5 Hz.

Type 2: **Combined frequency modulated (FM) and amplitude modulated (AM) signal.** This is AM modulation of the FM signal of type 1 (fig. 4.3). AM modulating frequency $f_{m(AM)}$ = 0.1 Hz, with modulation index of 60%.

The signal presented by type 2 above is more representative of real FBM signals.

4.6.1. RESULTS AND DISCUSSIONS

Figure 4.4 through to figure 4.7 show the tracking performance of the algorithms for the FM signal case (type 1). Figure 4.4 depicts the tracking performance of the OTB algorithm with a data block of 20 samples (2 seconds) and model order of 8. The performance of the OTB algorithm is dependent on the data block length used and on the model order. In the case of the LMS algorithm, its performance is depicted in figure 4.5 through to figure 4.7. The tracking performance of the LMS algorithm is dependent on many criteria as discussed in section 4.5.1. for example, if the filter is lengthened then the filter would tend to span more nonstationarities of the signals. This degrades the tracking performance. The spurious spikes in tracking (most evident in figure 4.5) may be alleviated by increasing

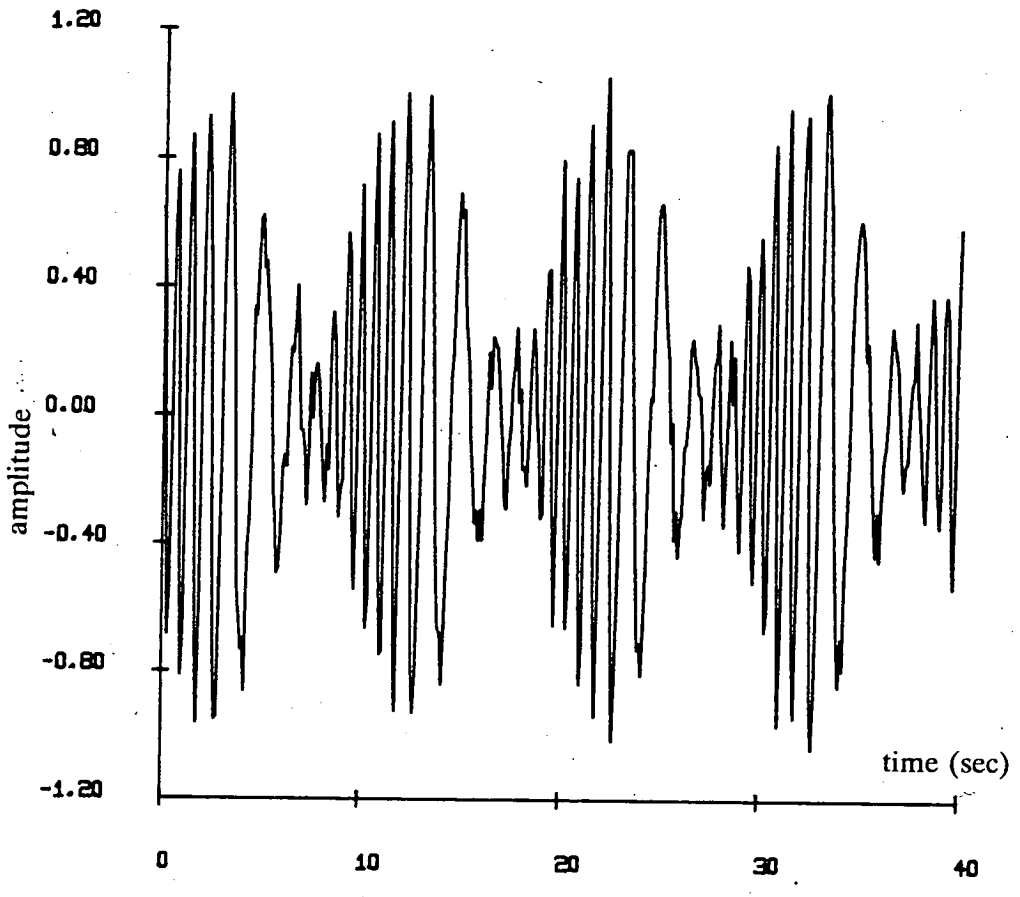

Figure 4.3 FM-AM modulated time series for performance evaluation.

the adaptation time. However, signal type 1, which comprises FM modulation only is not a close representation of real FBM signals as FBM signals may have variations in both the amplitude and the frequency.

Signal type 2, which is a combined FM and AM modulated signal, is more representative of real FBM signals, and the difference in performance of the two algorithms is more obvious. Although the frequency deviation has remained the same as that for type 1, introduction of the AM signal has added an extra degree of nonstationarity. Figure 4.8 through to figure 4.13 show the performance for tracking the FM-AM signal case (type 2). Figure 4.8 shows the performance using the

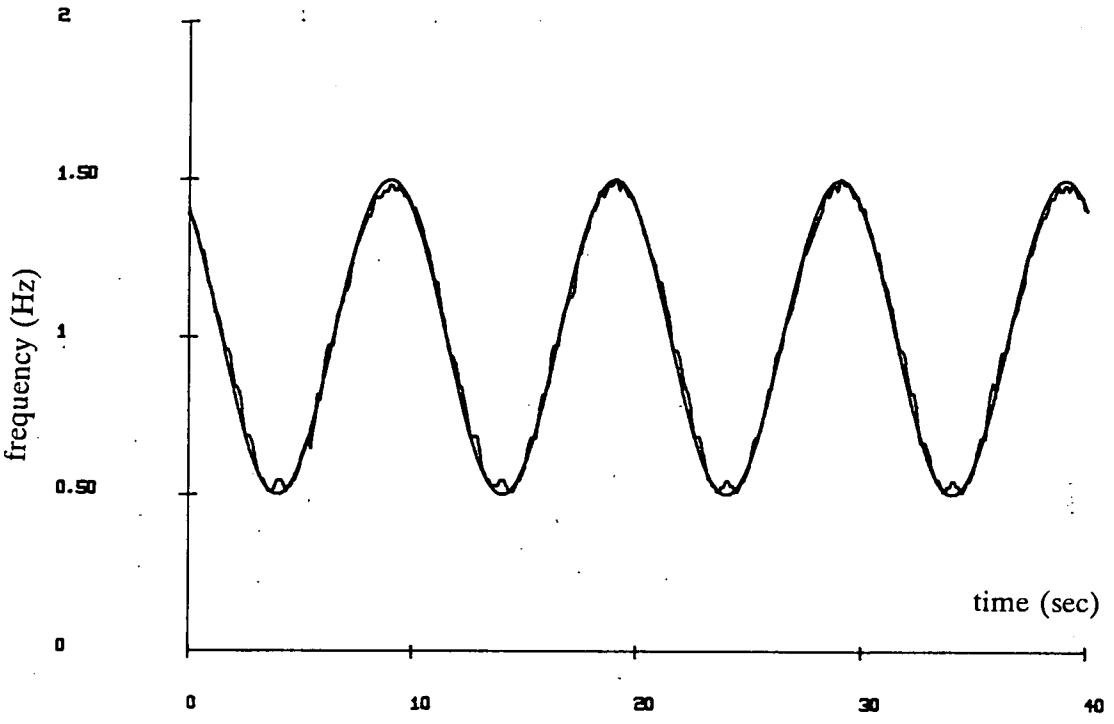

Figure 4.4 Tracking performance for FM signal using OTB algorithm

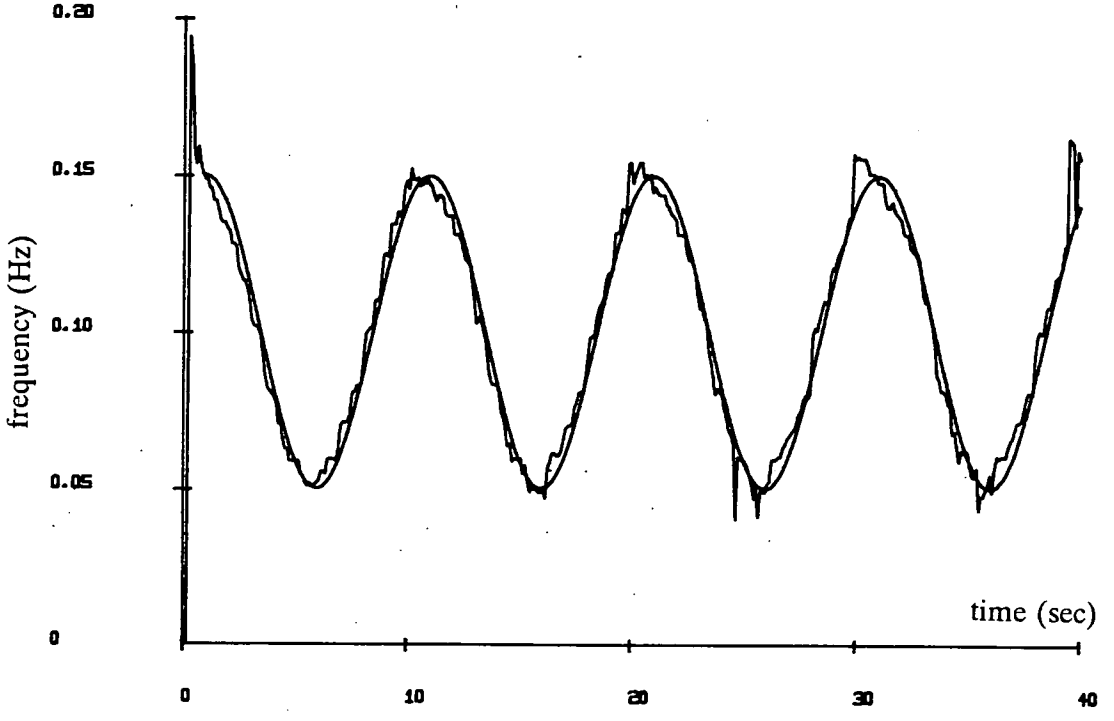

Figure 4.5 Tracking performance for FM signal using LMS algorithm with filter length = 20, adaptation time = 30

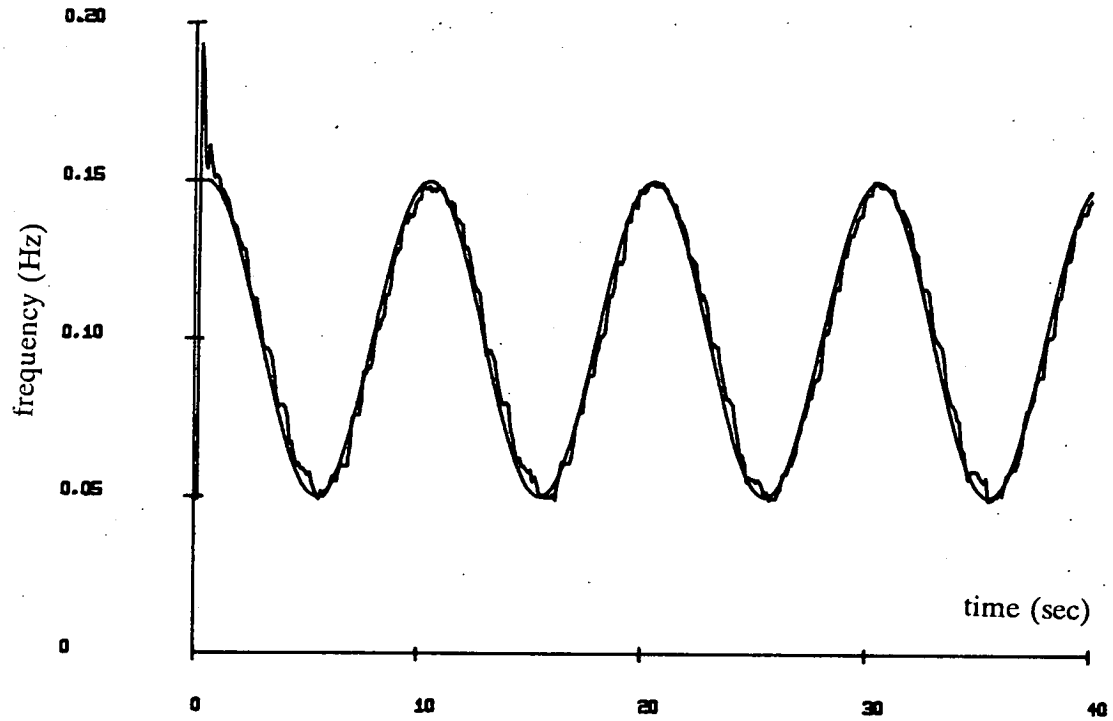

Figure 4.6 Tracking performance for FM signal using LMS algorithm with filter length = 10, adaptation time = 20

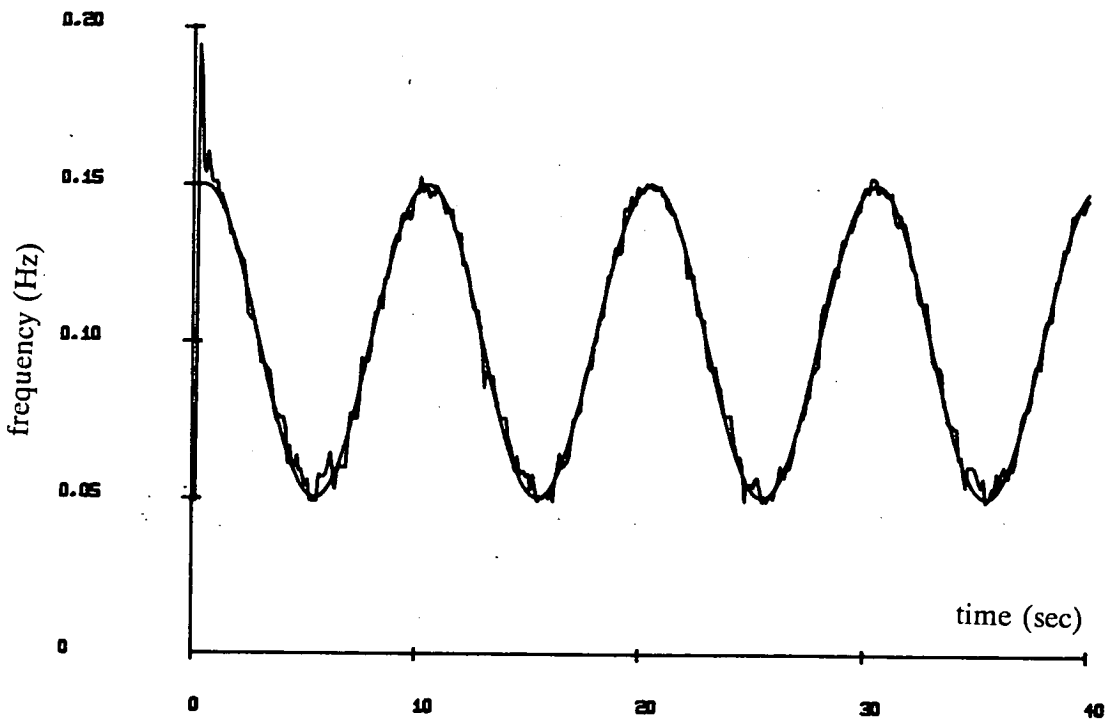

Figure 4.7 Tracking performance for FM signal using LMS algorithm with filter length = 6, adaptation time = 10

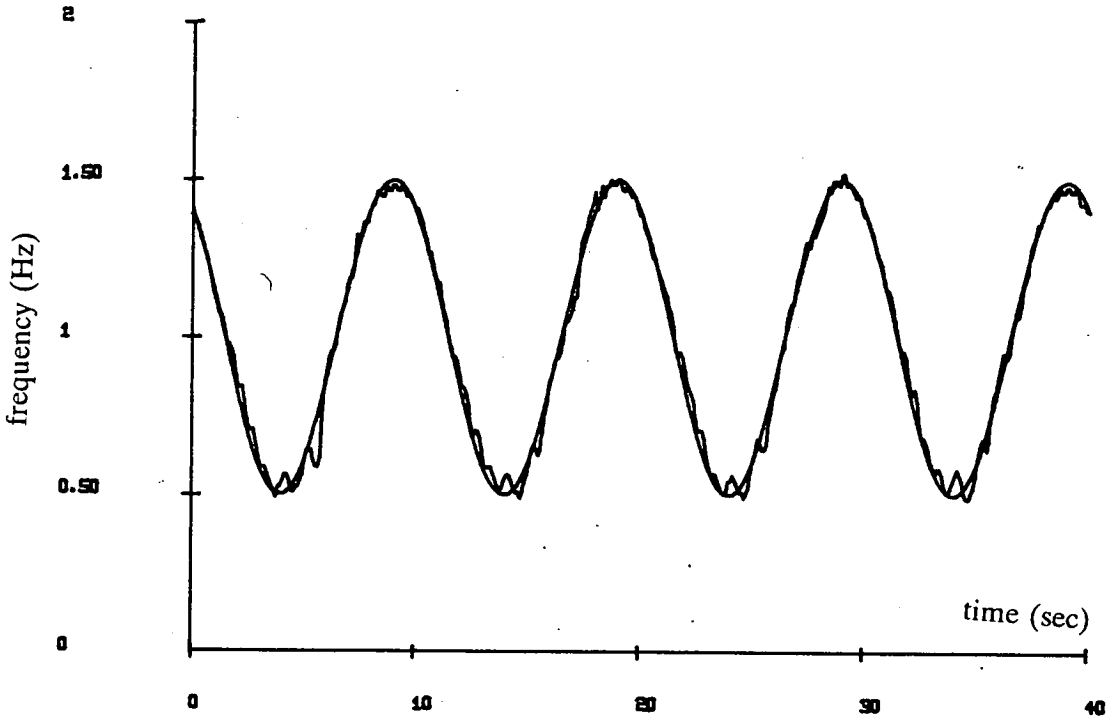

Figure 4.8 Tracking performance for FM-AM signal using OTB algorithm

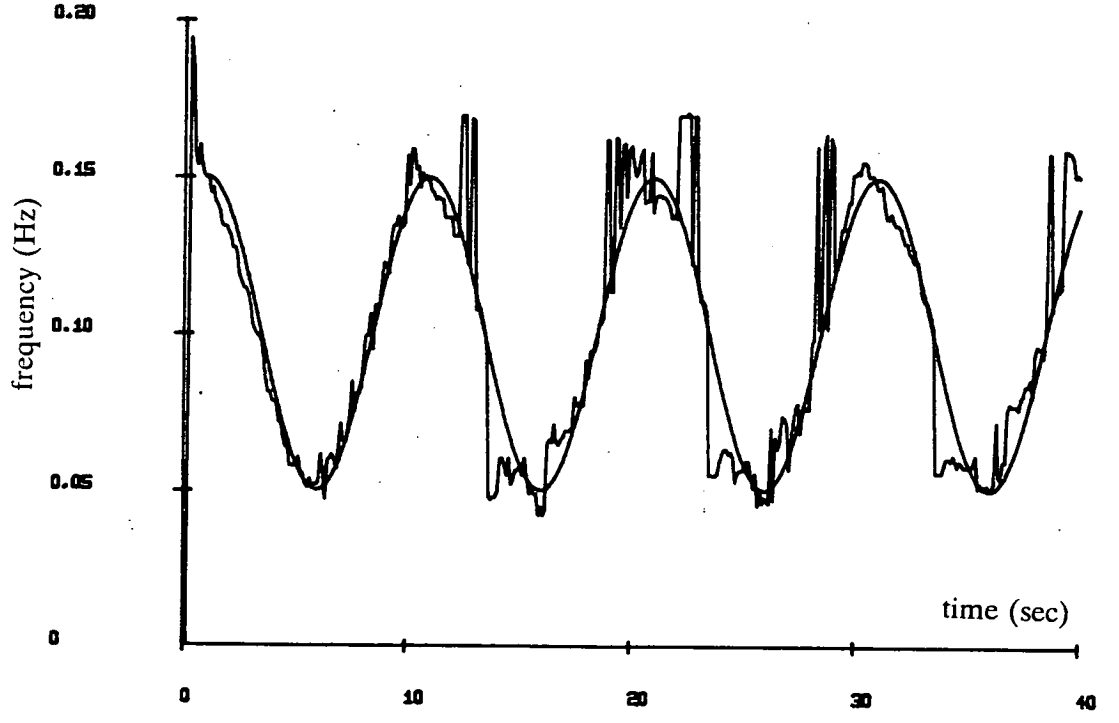

Figure 4.9 Tracking performance for FM-AM signal using LMS algorithm with filter length = 20, adaptation time = 30

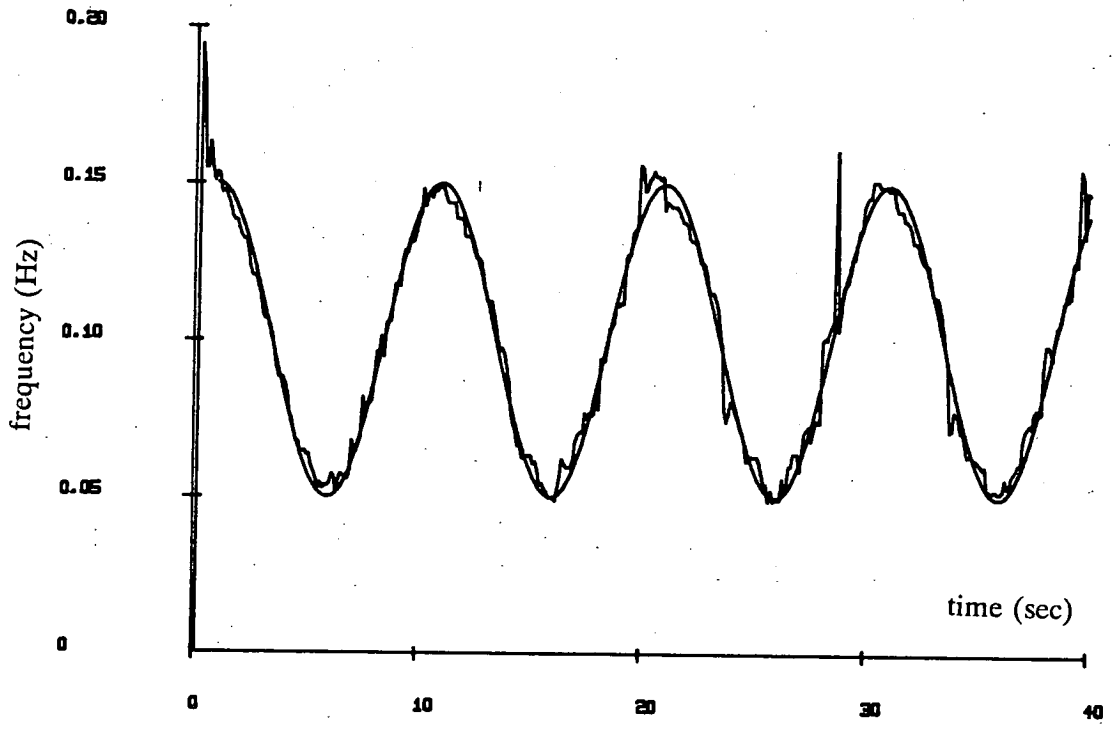

Figure 4.10 Tracking performance for FM-AM signal using LMS algorithm with filter length = 20 adaptation, time = 50

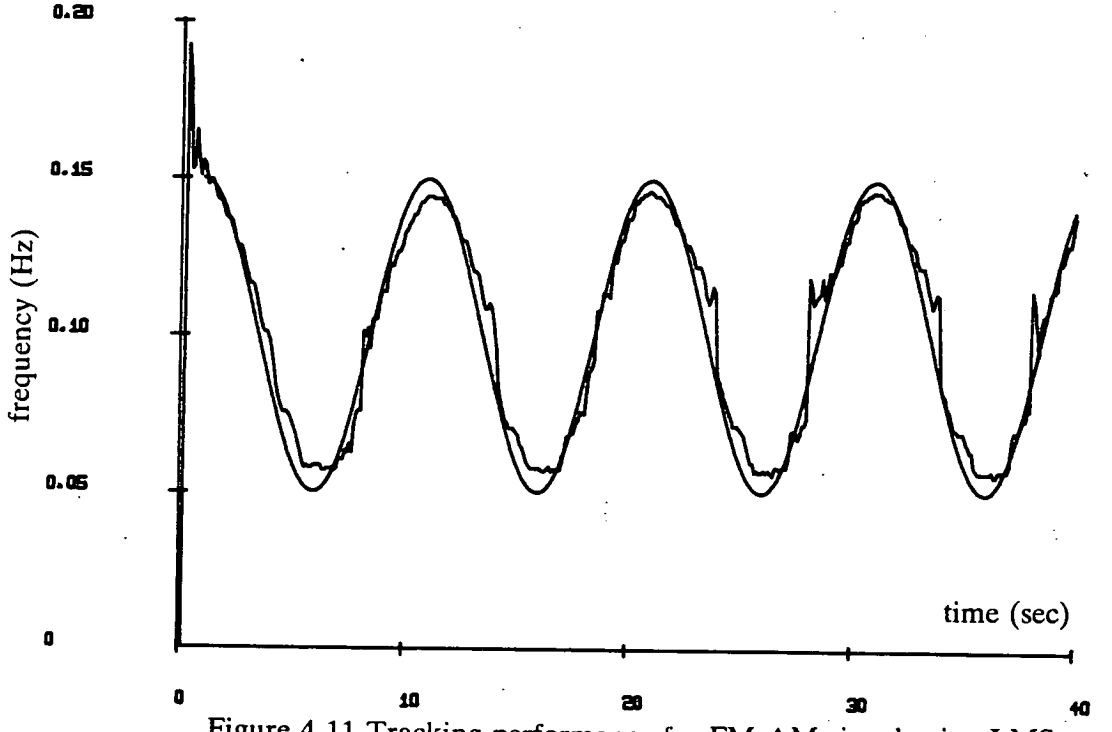

Figure 4.11 Tracking performance for FM-AM signal using LMS algorithm with filter length = 20, adaptation time = 100

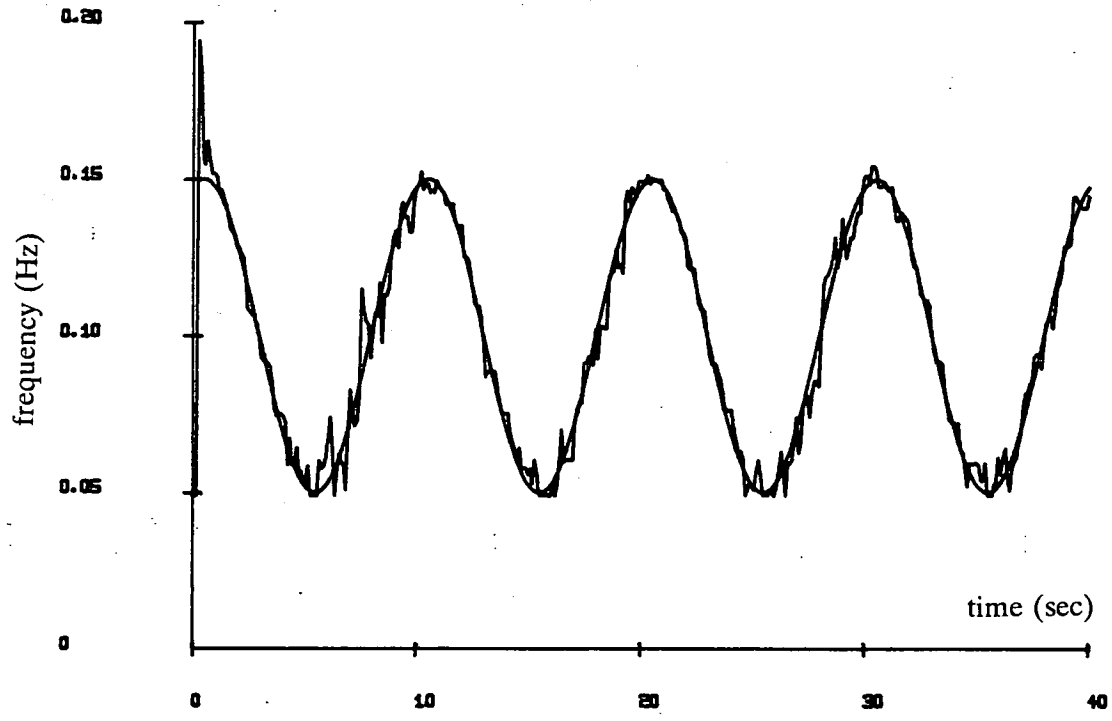

Figure 4.12 Tracking performance for FM-AM signal using LMS algorithm with filter length = 6, adaptation time = 10

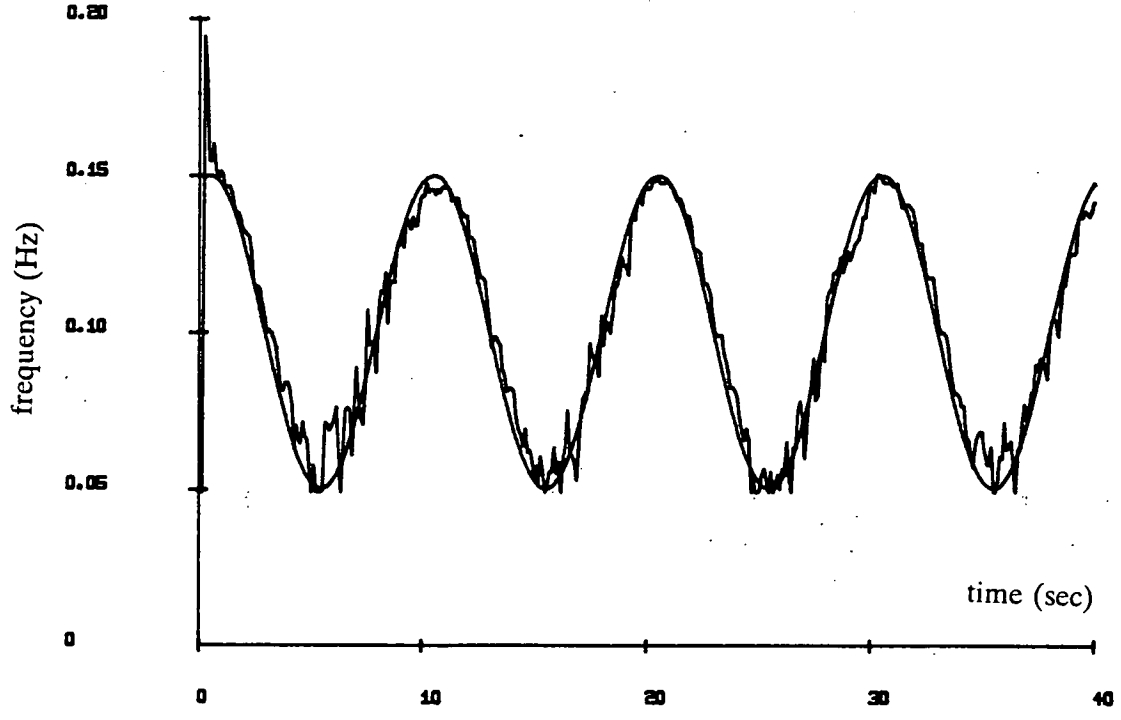

Figure 4.13 Tracking performance for FM-AM signal using LMS algorithm with filter length = 4, adaptation time = 10

OTB algorithm, while figure 4.9 through to figure 4.13 show the racking performance of the LMS algorithm. From these results it can be seen that the performance of the LMS algorithm is worse than for type 1. Again the performance of the LMS algorithm depends on the choice of filter length and adaptation time. As the filter length is decreased and the adaptation time is increased the presence of spurious peaks in the tracking is alleviated. This is seen is figure 4.11. However, the tracking ability is degraded in the regions of high nonstationarity, as reflected in the amount of frequency and amplitude variations within the filter length.

The OTB algorithm provides an acceptable tracking capability for the combined FM-AM signal model. The LMS algorithm's performance is dependent on the filter length, as shorter filter lengths will make the filter content more stationary. Spurious peaks in tracking are reduced with increased adaptation time which consequently decreases the convergence rate μ (eq. (4.21)). Unfortunately, however, increased adaptation time also smooths the tracking of sudden variations in frequency (figure 4.11).

From the results presented, one may conclude that, for time varying frequency components, the tracking ability of the OTB algorithm is much better than that of the LMS algorithm. For best results both the LMS and the OTB algorithms must have a stochastic stationary input signal, which makes the autocorrelation matrix Toeplitz. A stochastic signal is one that is governed by probabilistic laws, and it must be pointed out that the FBM signal which was analysed was found not to be strictly stochastic nor stationary. However, although the algorithms discussed were originally developed for stochastic signal, they performed acceptably for non-stochastic signal sinusoidal in nature, and the OTB algorithm has shown more tolerance to departure from the Toeplitz conditions.

4.7. SPECTRAL ESTIMATION OF FETAL BREATHING MOVEMENTS

The OTB algorithm was used to model fetal breathing movements as detected in maternal abdominal wall movements, using a passive, non-invasive, transducer (discussed in chapter 3). FBM signals were obtained by filtering MAM signals using a low pass filter with a cutoff frequency of 2.5 Hz cascaded with a high pass filter with a cutoff frequency of 0.5 Hz. The filtered signals are depicted in figures 4.14a and 4.14b. FBM signals are nonstationary and may be modelled as frequency and amplitude modulation of a carrier which may not be sinusoidal, but which will at least have a dominant fundamental.

In this chapter we discussed the properties of the OTB algorithm for short data blocks and found its performance favourable to other algorithms. Hence the OTB algorithm was chosen for the analysis of FBMs. The data block length in the analysis was of two second duration (20 samples). This data block length was long enough to ensure that a full wavelength of the lowest frequency of FBM was present; while being short enough to permit a quasi-stationary data assumption. These conditions lead to a Toeplitz autocorrelation matrix, which is necessary for the Levinson-Durbin decomposition[45, 31, 34, 48].

An 8^{th} order AR spectral model was assumed in the analysis of FBMs. This choice of model order was based on the observations of Ulrych and Ooe [40] and has proved satisfactory. Figures 4.15 and 4.16 depict waterfall representations of the AR spectral estimates, each of 100 seconds duration. In figures 4.15 and 4.16 time traverses along the vertical axis with one second between each estimate and frequency traverses along the horizontal axis from 0 Hz to 3 Hz. The boxed waveform represents the 100 seconds of filtered MAM signal used in the analysis shown in each figure. The analysis uses a 2 second sliding window with 50% over-lap (1 second shift). This demonstrates the ability of the OTB algorithm, applied

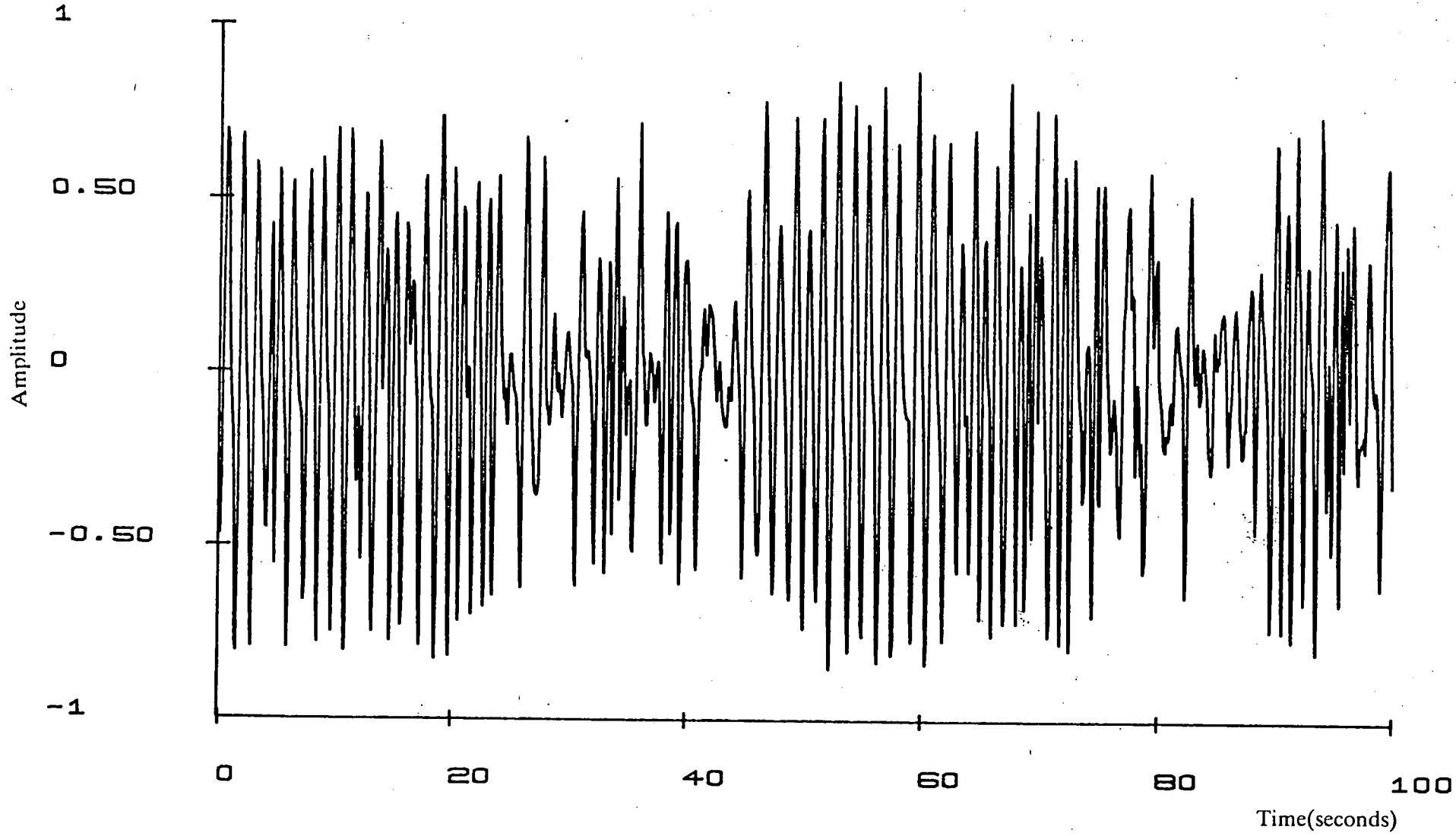

Figure 4.14a 100 seconds of FBM signal.

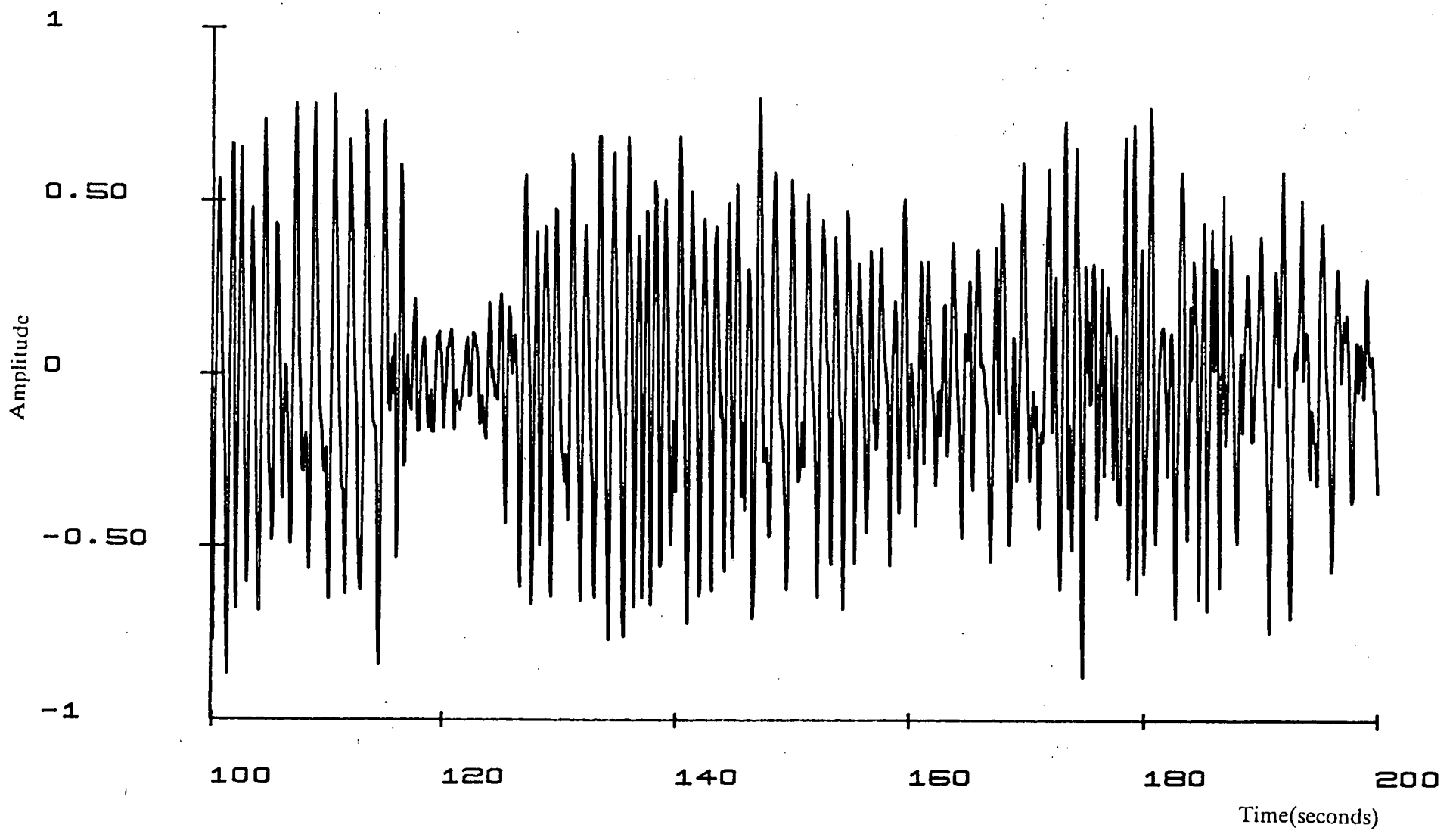

Figure 4.14c 100 seconds of FBM signal.

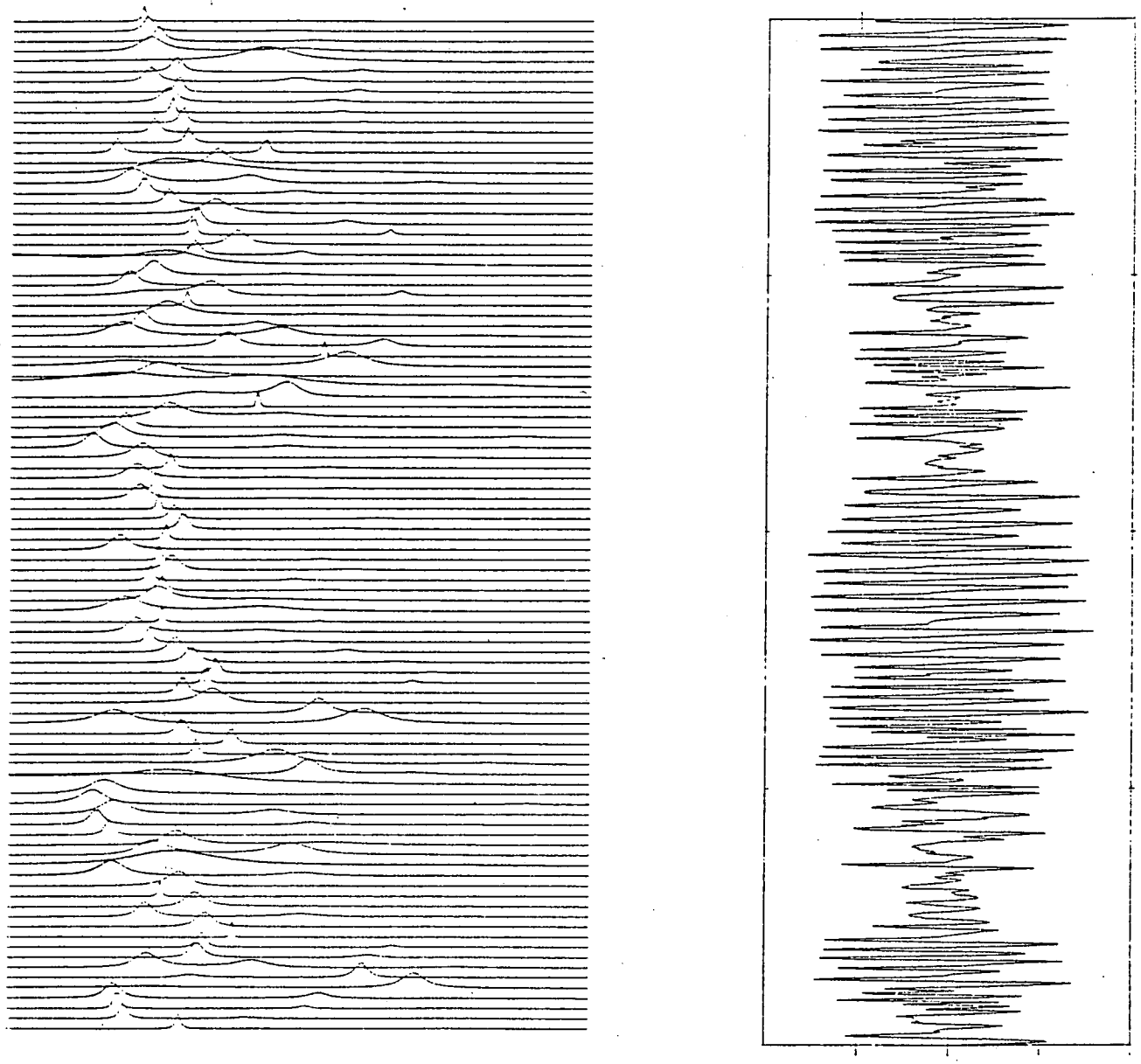

Figure 4.15 Waterfall diagram showing spectral content of 100 seconds of FBM signal.

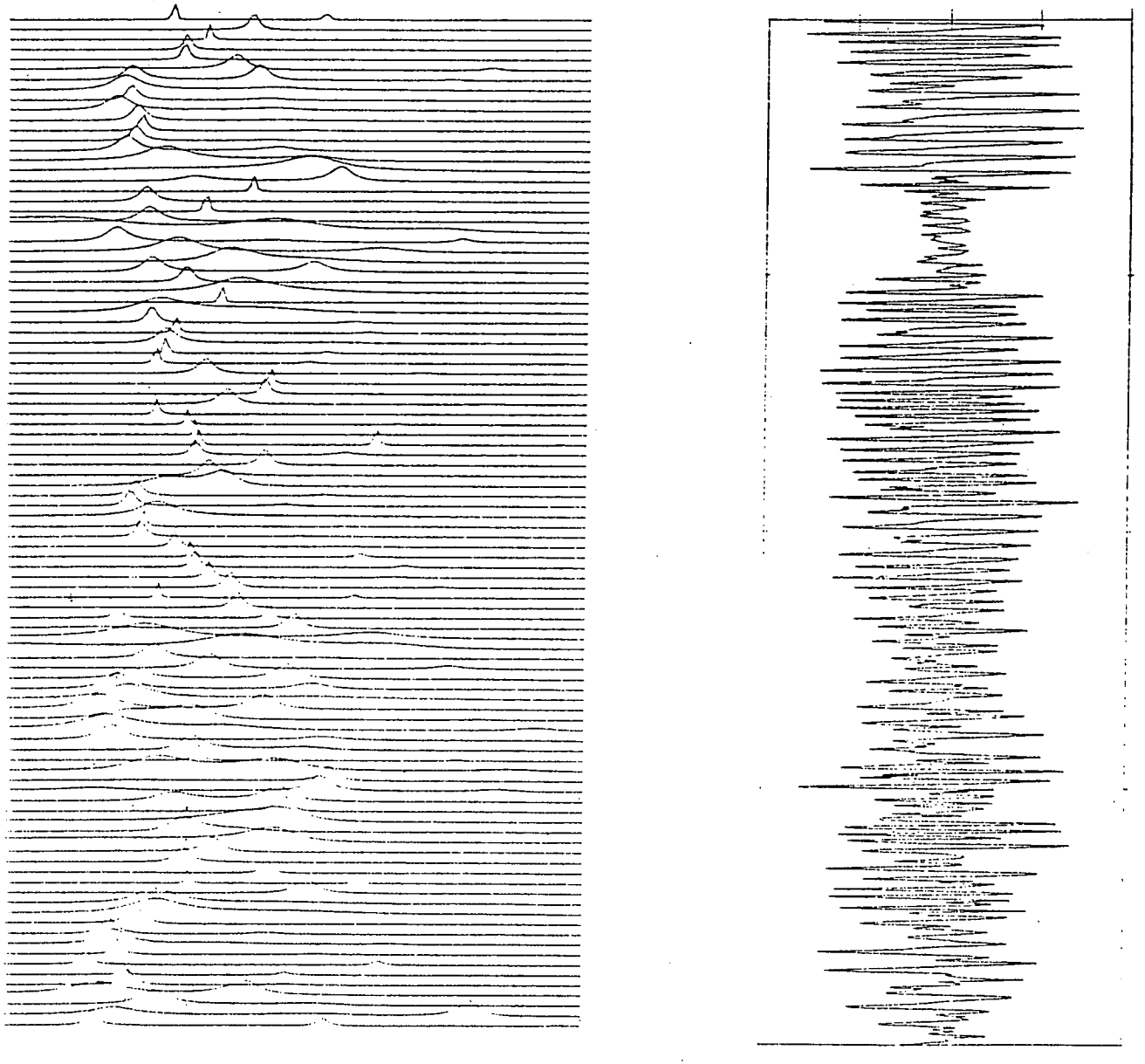

Figure 4.16 Waterfall diagram showing spectral content of 100 seconds of FBM signal.

to typical clinical FBM signal, results in a stable model which reflects the coherence properties of the original time domain signal.

4.8. CONCLUSIONS

In the previous section AR spectral estimation was used to provide spectral information pertaining to fetal breathing movements. The waterfall diagram was used as a tool for visual representation of spectral estimates of overlapped data blocks. In the previous section, the OTB algorithm was used to produce waterfall diagrams from a two second sliding window with 50% overlap (10 samples shift).

One of the advantages offered by AR estimation is that spectral information is abstracted from the temporal data irrespective of amplitude, provided the signal is not below the noise floor. Even in this latter case, algorithms do exist which enhance the coherent signal in a background of white Gaussian noise, and to some extent against a background of coloured noise.

Figure 4.17 and figure 4.18 are waterfall digrams following AR analysis of an FBM signal using a two second sliding window with a 95% overlap (19 samples). The data shift between each analysis is a single sample (0.1 second). The two waterfall diagrams shown in figure 4.17 comprises contiguous data, and similarly for figure 4.18.

From visual inspection of figures 4.17 and 4.18, two interesting observations may be made:

1- The continuing presence of FBM throughout this record segment is confirmed clearly by the spectral coherence in the waterfall diagrams. This coherence is seen even when the temporal data drops to a level that makes it difficult to confirm the presence of FBMs by visual inspection of the time domain.

2- In both figures 4.17 and 4.18 underlying oscillations in FBM rate are visible. These oscillations are similar to those observed in FHR. This physical phenomenon does not appear to have been reported in the literature. The underlying periodicities in FBM rate is discussed further in the following chapter.

Therefore, transferring the temporal data into a different domain (in this case the frequency domain) the above observations have been facilitated. This is a good example why we must employ transformations in signal processing to improve the interpretation of the signal of interest.

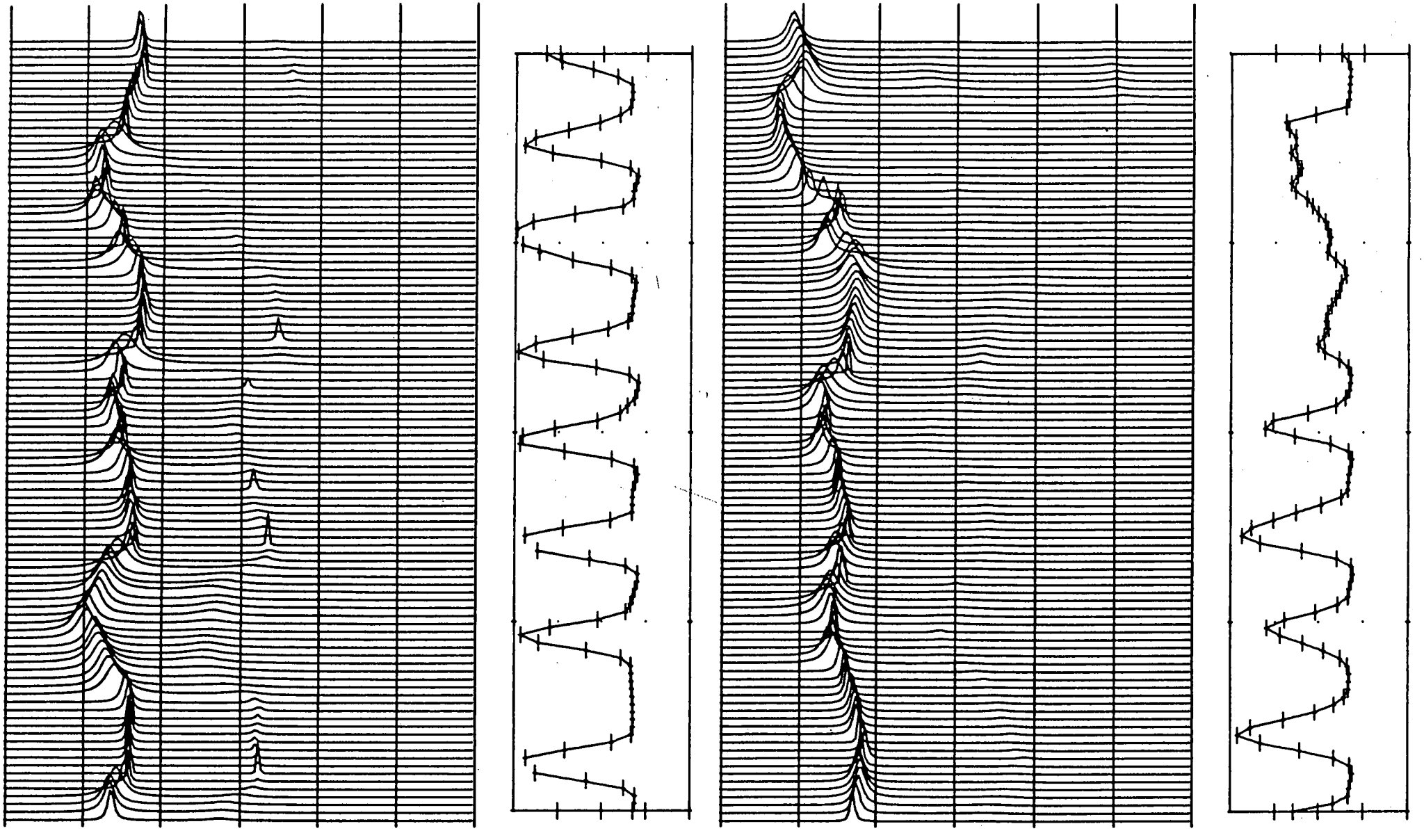

Figure 4.17: Waterfall diagram for 95% overlap.

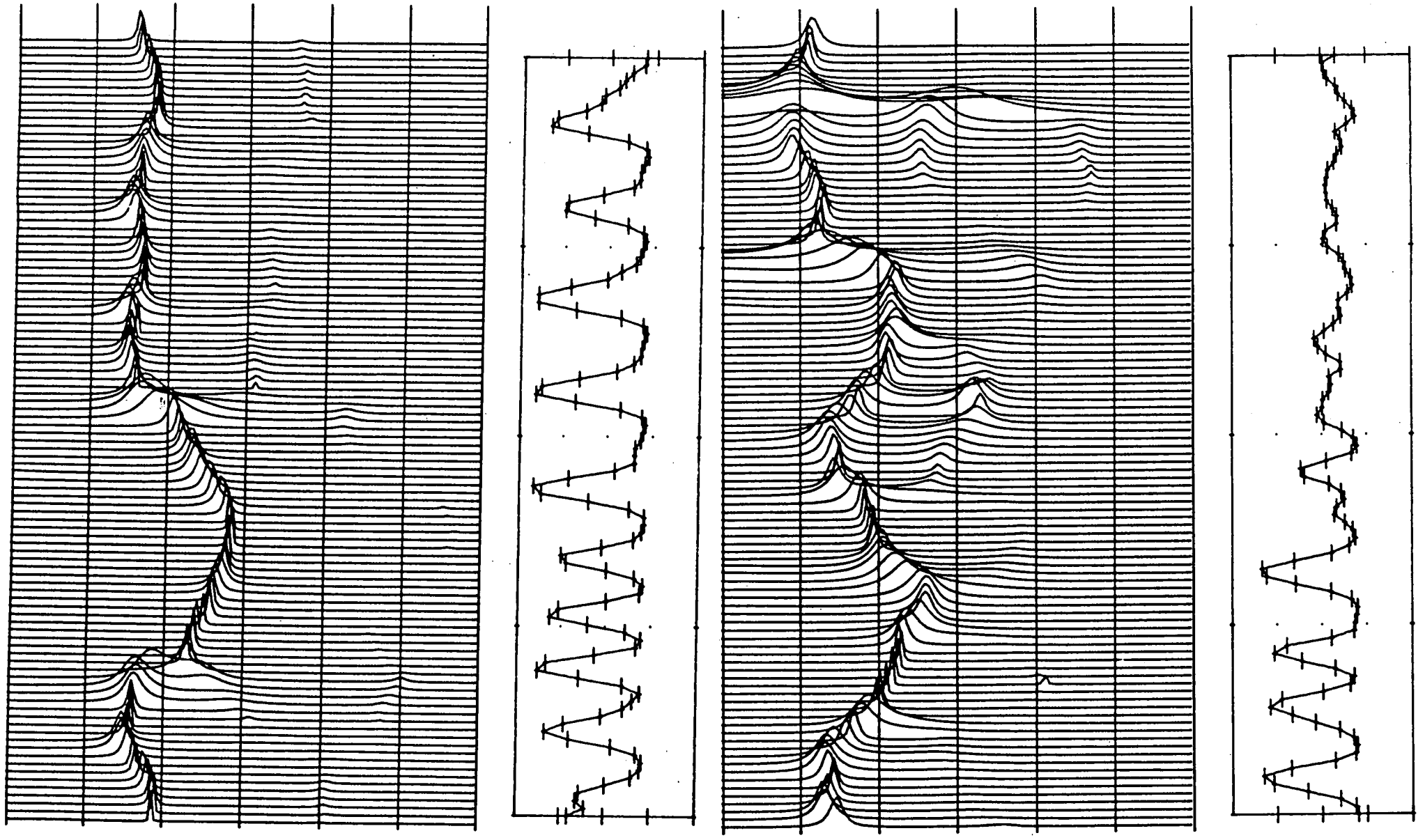

Figure 4.18: Waterfall diagram for 95% overlap.

CHAPTER 5

EXPERT SYSTEM FOR THE ESTIMATION OF FETAL BREATHING RATE

5.1. INTRODUCTION

In the previous chapter, spectral modelling of FBM was performed using short data. In the absence of noise and other corrupting signals (e.g. maternal breathing etc.) it is easy to identify the peaks from which fetal breathing rate may be derived. This ideal condition seldom occurs, and noise degrades the integrity of spectral modelling. Therefore some decision making algorithm must be deployed which is capable of discerning the relevant peaks and estimating FBM rate. FBM rate is non-deterministic and cannot be modelled by a closed form mathematical expression. A heuristic approach is needed to select the pertinent peak. An expert system was used to perform this task of identifying and tracking the FBM peaks. Such a system uses the expertise of a trained observer or a domain expert to perform the required task. Algorithms used in expert systems are only capable of performing tasks which may be carried out by human experts, but they are often faster more accurate and more consistent.

In the following sections, an insight into expert system and knowledge representation is provided. The steps and principles of the rules and reasoning used to track FBM peaks is outlined, with graphical representation of the results.

5.2. EXPERT SYSTEMS

The majority of computer programmes are designed to perform some "simple" reasoning tasks. These tasks may be performed by adhering to some conventional well established mathematical formulae which describe the problem, e.g. interest rate calculation, salaries, mathematical formulae etc.. When writing such simple reasoning tasks, an inside knowledge of the underlying problem is not essential. The traditional structure of these types of programmes may be defined as :

DATA + ALGORITHM = PROGRAMME

In certain circumstances, and in certain applications, such well established mathematical formulae and algorithms which accurately model the problem and provide a solution may not exist. Such problems may be solved by exploiting heuristic knowledge acquired by a human expert as a results of many years of experience. This type of programme, which is called an expert system, stipulates an in-depth knowledge of the problem . The expert system may be defined as:

DATA + KNOWLEDGE + REASONING = SYSTEM

The structure is also depicted in figure 5.1. The characteristics and objectives of expert system are:

a) The main objective of the expert system is to solve the problem encountered.

b) An expert system is problem-oriented. Its knowledge base is dedicated to the domain of the particular problem.

c) In some applications, explanation of the steps leading to the solution are required. These may be required for two reasons:

   1- If the user is an expert in the domain, then he may require the pathology of reasoning which led to the solution. This is necessary, since well

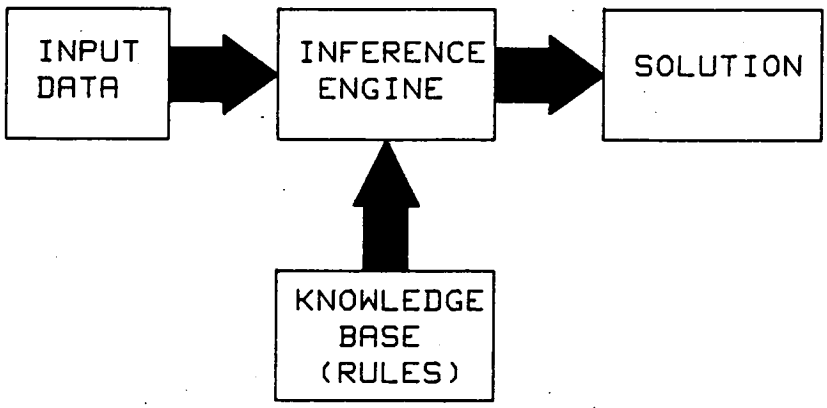

Figure 5.1: Block structure of an expert system.

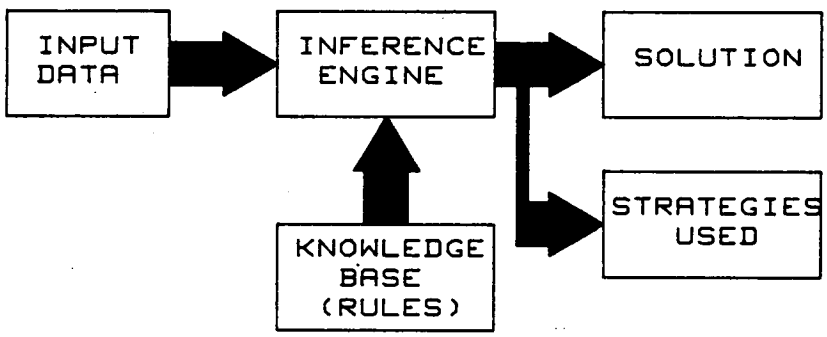

Figure 5.2: Verbose expert system.

established formulae do not exist, and the the expert is required to check the reasoning and strategies used to develop the solution(figure 5.2).

2- If the user is not an expert in the domain, then the system is required to train the user in order to enhance his knowledge in the domain by explicitly explaining the steps of reasonings used (figure 5.2).

d) Some expert systems use a dynamic knowledge base which automatically updates its own knowledge to improve its performance. These expert systems

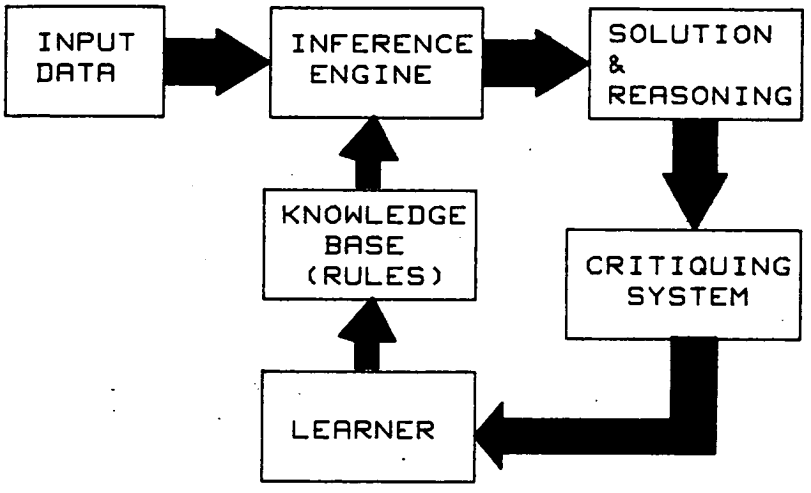

Figure 5.3: Machine learning system.

are sometimes called "machine learning systems". They attempt to emulate the expert by updating the knowledge base as a result of feedback from some critiquing system which can judge the success of the expert system's decision (figure 5.3). The need for this type of an expert system arises from the difficulty of extracting all the relevant information from the domain expert during the formulation of the system.

5.3. THE STRUCTURE OF AN EXPERT SYSTEM

Expert systems have different structures for different applications, but they all contain the basic elements shown in figure 5.1.

5.3.1. KNOWLEDGE BASE

The knowledge base is the knowledge that is specific to the domain of application. Such knowledge is extracted from the domain expert.

The knowledge base may take many forms such as:

1- Production rules: These are statements which encapsulate rule of thumb knowledge of the problem. Each rule comprises patterns that determine the

applicability of the conditions and the action to be performed if the conditions are true. The rule may be represented in the familiar IF - THEN format e.g.

IF (number of peaks > 1) THEN (check for maternal)

IF (maternal component) THEN (remove maternal fundamental and harmonics)

Production rules in the knowledge base are basic relationships and conditions between the different aspects of data. In general, there are no mathematical formulae to replace the knowledge represented in the above rules.

2- Structured networks:

a) Associative networks: In this type of knowledge base, it is required to locate knowledge which is not explicitly mentioned in the data. Data could state some action e.g " **X** flew to Paris" and the question might be "did **X** catch the plane ?". The knowledge base should have the different meanings of the same word according to context.

b) Semantic networks: Knowledge is represented by a set of nodes, linked to one another by arcs which describe the relationship between each node. The nodes may stand for objects, concept or events; the arcs are the agents which put the nodes in perspective.

Both semantic and associative networks represent knowledge in conceptual structures. They attempt to represent knowledge in a similar fashion to the human brain.

3- Representation using logic.

Using logic relationships to represent knowledge is a powerful tool to derive answers to questions and to make mathematical deductions. Logic representations take many forms:

a) Propositional logic.[54]: In propositional logic, facts can be represented as logical propositions which may be used to deduce answers to questions. The rules apply directly to the facts.

"B may be deduced given A is true" is denoted by $A \rightarrow B$

Propositional logic is attractive because it is simple to construct and use.

b) Predicate logic[54]: Currently this is the most popular form of logic. It has a "mechanistic" way of dealing with "truth" and "falsehood". It is widely used in natural language processing. It comprises a functor which describes the property of the object, and a predicate which is the object.

c) Probabilistic logic.[54, 55]: So far it has been assumed that some conditions are either "true" or "not-true". Unfortunately the world is not so clearly dichotomised, and there are situations where knowledge is "probably true". This type is applicable where the relevant outcome is random, or in some cases, where enough data are not available to establish a proper model. In such cases one has to resort to probabilistic reasoning.

d) Fuzzy logic[56, 57]: Thus far, an attempt has been made to outline some basic forms of knowledge representation, where information is represented in a precise form. There exist cases, where information may not be represented in a precise form. Such cases fall in the more subjective realm of human judgement, e.g. tall - very tall, far - very far etc.. The question 'How far is far?' may not be quantified in a precise fashion. Fuzzy sets and logic - sometimes called 'possibilistic logic' _ provide a method of representing these imprecisions. Objects in Fuzzy sets are mapped into some continuous scale from 0 to 1 (figure 5.4). The function which describes the fuzzy object is not universally defined, but is

rather chosen by the expert and the knowledge engineer.

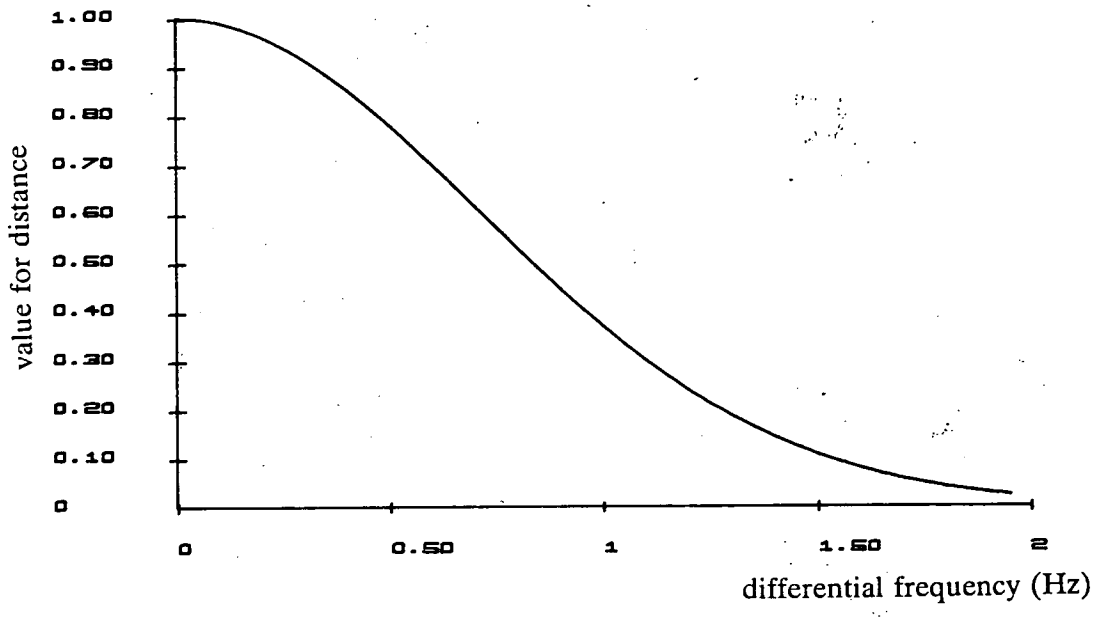

Figure 5.4: Mapping differential frequency to a measure of Nearness.

Figure 5.4 depicts a function which describes 'the nearness of a peak'. The differential frequency is the difference in frequency of the peak in question from some running mean. The mapping function used here is a Gaussian function. This same function may be used to describe nearness of different dimension. For example, 0.75 near might be 50 miles distance between cities in small countries and hundreds of miles in large countries, or even millions of miles if one is looking at the stars.

Often, there are no rational grounds for choosing a particular mapping function to quantify an imprecision. These mapping functions are chosen by the expert as a result of experience. The final appraisal of the function which has been chosen is based on "as long as it performs satisfactorily" then it is acceptable. There are some expert systems which allow the user to modify the mapping function to suit the user's beliefs and experience.

A procedure is also required to manipulate the information provided by this fuzzy representation. Boolean logic deals with integer truth values. To deal with fuzzy truth which has non-integer truth values - multi levelled truth values - an extension of the classical Boolean logic is used[56]:

Suppose the truth value for a proposition is x_1 and for another proposition is x_2, where x_1 and $x_2 \in [0,1]$.

$$x_1 \text{ AND } x_2 \text{ is } \min(x_1 , x_2)$$

$$x_1 \text{ OR } x_2 \text{ is } \max(x_1 , x_2)$$

$$\text{NOT } x_1 \quad \text{is} \quad 1 - x_1$$

Where min() denotes minimum value and max() denotes maximum value.

5.3.2. INFERENCE ENGINE

The inference engine[58, 54, 59, 56] is that part of the system which manipulates knowledge in order to solve problems. It uses preassigned strategies for knowledge manipulation. The inference engine could be considered as the thinking part of the system and the knowledge base is what the inference engine thinks about. This analogy equates an expert system to the 'human expert'.

There are many possible strategies which may be used for example:

a) Forward chaining: This involves reasoning through knowledge to find the hypothesis that satisfies the observed data. It starts from the data and some base facts which are available, and attempts to match these, in search of the solution, by invoking new rules.

b) Backward chaining: In this reasoning strategy, the goal - the solution - is hypothesised. The system is asked to find the data which proves the given hypothesis or generates the solution provided.

c) Rule value approach: This strategy uses neither forward nor backward chaining. It considers each item of evidence and then assigns a value to each rule and attempts to form a hypothesis using the evidence with the highest value first.

5.4. PEAK TRACKING

The basic structure of expert systems was outlined in section 5.2. This section describes the rule-based and fuzzy logic knowledge based approaches used to track FBM peaks. The rule-based approach is currently the most commonly used knowledge base for implementing diagnostic expert systems. Peak tracking, although not a diagnostic system in the true sense, may be considered as a psuedo diagnostic system. This is because in peak tracking all the peaks in a spectrum are taken into consideration. Peaks which do not fit in a pattern - or the ones which constitute potentially erroneous FBM rate - are eliminated. Fuzzy logic is used to measure the "nearness" of the peaks to some running mean. This measure of "nearness" must be defined in a continuous multivalued logic, in this case fuzzy sets.

In general, rule based systems require a great deal of "expertise" knowledge in the domain of application. The final rule based system provides an acceptable performance and an understandable solution which will be in agreement with the actual human expert, provided knowledge had been successfully acquired and properly defined.

Special expert system shells are available which use Prolog, LISP etc.. These shells provide fast tools for producing and testing prototypes. They are very useful in testing some hypotheses, but have no arithmetic capabilities. Daku and Grant [60] developed an expert system to determine the correct model order selection for

linear prediction filters using C- language to perform the mathematical manipulations, and a Prolog blackboard shell to reason through the results.

This chapter describes a peak tracking algorithm for FBM rate estimation which was implemented using C- programming language. The rules were generated through "expert knowledge" of the problem in hand. This knowledge was used to define the conditions for accepting or rejecting a peak as being due to FBM.

5.4.1. RULE GENERATION

In chapter 4, FBMs were modelled using a two second sliding window with 50% overlap. During periods of FBM, the spectrum of each data block included a fundamental FBM Fourier component and, possibly harmonics. It also also included maternal breathing movements and harmonics and components relating to other fetal and maternal activities. The significance of maternal and other corrupting components were dependent on the intensity of FBMs. The main objective is to discern peaks pertaining to FBMs, despite the presence of these corrupting components.

There are some basic facts and underlying characteristics, some of which were discussed in chapter 1 and 2, which must be stated:

a) FBM rate lies mainly in the range of 30 - 90 breaths/minute. Although rates below and above this range have also been observed.

b) Maternal breathing movements (MBM) and its harmonics may be present and may corrupt FBMs.

c) MBM rate normally lies below 20 breaths/minute.

d) Fetal and maternal heart components, which may lie in the same range as

FBM rate do not contribute to the noise. This is because their intensities are normally of the order of 40 dB below FBMs.

The rules which were used in the peak tracking algorithm are presented in the form of a decision table. The table may be partitioned to four sections (figure 5.5): Condition section and the condition values, the action section and the action entries.

Condition section	Condition values
Action section	Action entries

Figure 5.5: Decision table.

A decision table may have both deterministic and non-deterministic conditions. Deterministic conditions conform to fixed predetermined values such as the current number of peaks or the presence of MBM; non-deterministic conditions take values which reflect a subjective measure of the parameter, such as the current distance of a peak from the running mean. The combination of the two types is more representative of an expert tracking the peaks manually. Once nondeterministic condition entries are used in the decision making, then the system becomes sensitive to subjective evaluation, which is introduced by subjective definition of the imprecise information. A sensitivity index (SI) provides a measure of the extent of subjectivity embedded in the reasoning and judgements.

$$SI = \frac{C \quad R}{\sum M \quad TR}$$

Where C is the number of nondeterministic conditions used; R is the number of rules which deal with nondeterministic conditions; M is the number of possible values which a condition value can take. For nondeterministic conditions the possi-

ble number of values is taken 1; TR is the total number of rules in the table.

This gives an index SI $\in$ [0,1], where 0 index implies that decisions are totally the result of deterministic conditions and index of 1 implies decisions are completely dependent on the user's subjective judgements.

RULE	1	2	3	4	5
No. of peaks	.	1	1	>1	>1
MBM	.	T	F	F	T
DC Component (x_1)	$f_1(x_1) > 0.4$	.	.	.	.
NO FBM Possible	(1)	(1)	.	.	.
Extract FBM Rate	.	.	(1)	.	.
Remove Maternal & Harmonics	.	.	.	.	(1)
CALL(RATE)	.	.	.	(1)	(2)
EXIT	(2)	(2)	(2)	.	.

Figure 5.6: Decision table for peak tracking algorithm.

Figure 5.6 and 5.7 represent the decision tables used to track the peaks. The rules were processed in order from left to right in the table. The numbers in the action entries represent the order of execution of the routines to satisfy the associated rule. Figure 5.6 is the top level decision table, and within this top level decision table second level table is called - e.g. CALL(RATE). Figure 5.7 depicts the rules in decision table RATE. Figure 5.8 and 5.9 depict the main top level and the second level decision tables in tree chart form respectively.

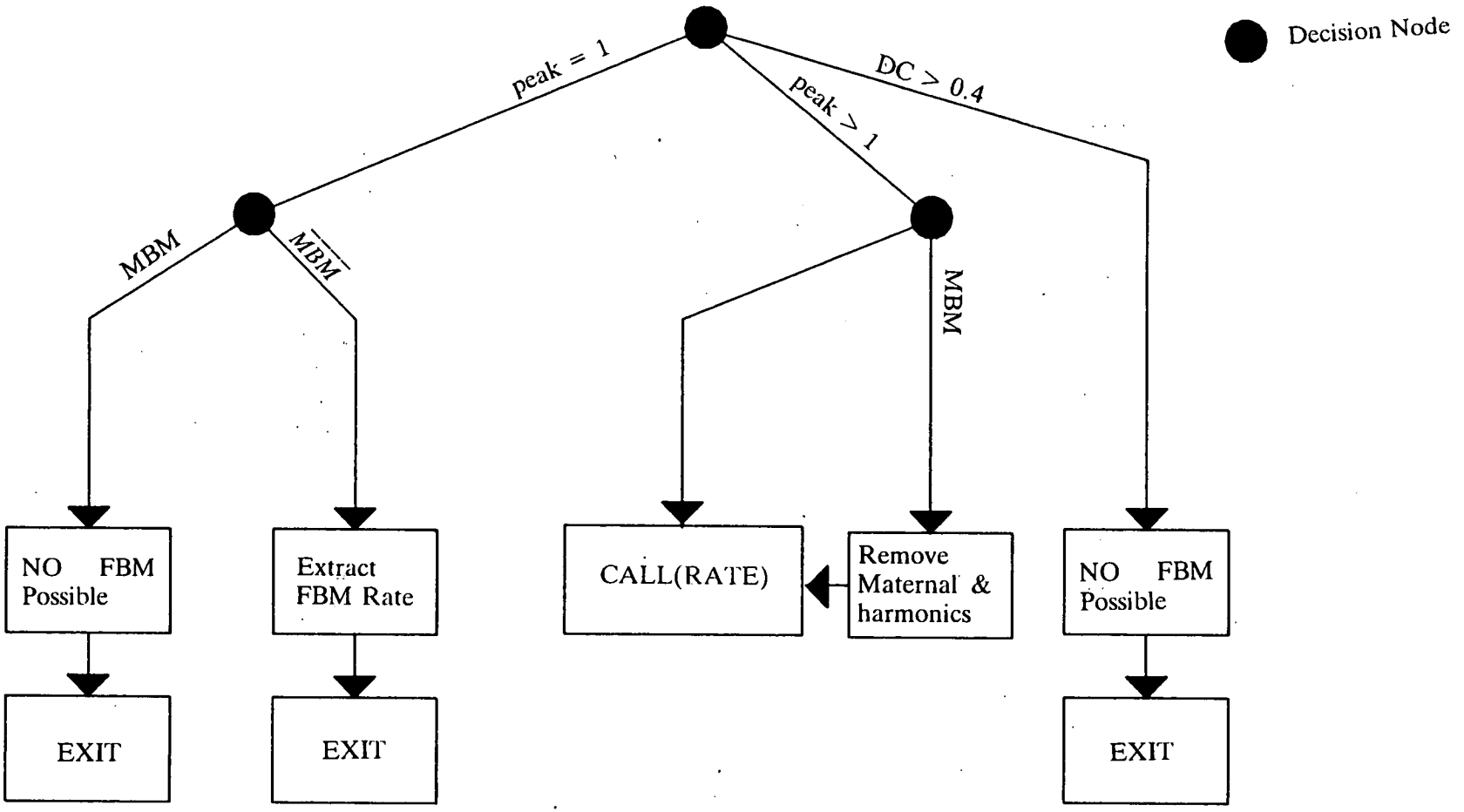

Figure 5.8: Reasoning tree for top level decision table.

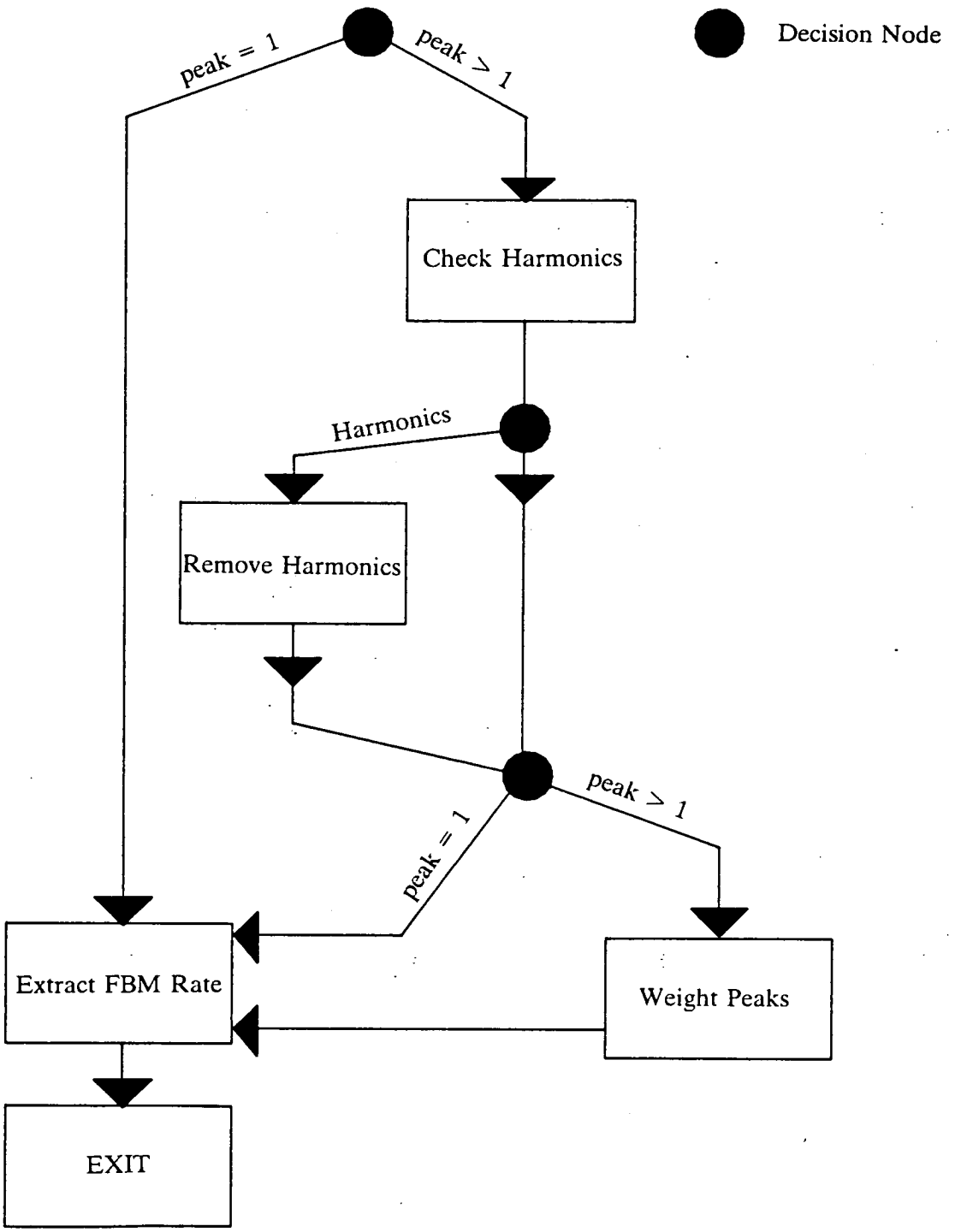

Figure 5.9: Reasoning tree for the second level decision table (RATE)

RULE	1	2	3	4	5
No. of peaks	1	>1	.	1	>1
Harmonics	.	.	1	.	.
Weight Peaks	.	.	.	.	(1)
Extract FBM Rate	(1)	.	.	(1)	(2)
Check Harmonics	.	(1)	.	.	.
Remove Harmonics	.	.	(1)	.	.
Check No. of Peaks	.	.	(2)	.	.
EXIT	(2)	.	.	(2)	(3)

Figure 5.7: Decision table for RATE.

Fuzzy representations used in the algorithm are:

a) DC component: Despite the fact that the mean in the analysis window is cancelled prior to applying optimum tapered Burg modelling, there are cases where complete cancellation of the DC component from the temporal data is not possible. This results in a large component around 0 Hz in the spectrum. The presence of this large DC component in the spectrum may reduce or in some adverse cases obliterate other peaks. In addition, the presence of large DC components may reduces the confidence in the estimates of the spectral peaks.

b) Weighting of Peaks: After removing the maternal breathing fundamental component and its harmonics, the remaining peaks are weighted using a Gaussian function centered on the current estimated running mean (see figure 5.4). The previous 10 second estimates of FBM rates are used as the running mean.

The deterministic conditions are:

a) Number of peaks: Although the number of peaks in the spectrum may be represented in a fuzzy set, such representation will not serve any purpose in this application. There are two conditions either one peak exists in the spectrum or more than than one peak exists.

b) Presence of maternal breathing movements: The presence of MBM is investigated before the inferencing is started. Its existence is either TRUE or FALSE. The presence of a strong maternal fundamental Fourier component of breathing will provide a method of removing higher harmonics due to maternal breathing.

The expert system was developed and tested on the spectral model of the MAM signal. The spectral modelling of the MAM signal was discussed in chapter 4. As mentioned previously, this data was corroborated as comprising FBM and MBM. The condition stub was built to suit this type of recording. The output of the peak tracking mechanism is presented in figure 5.10.

5.5. PERIODICITIES IN FETAL BREATHING RATE

Estimates of FBM rate using the autoregressive analysis and the peak tracking algorithm are shown in figure 5.10. Although this provides second-by-second estimates of FBM rate, it presents a noisy representation of the rate, as far as seeing underlying rate patterns is concerned.

Estimation of a signal which is corrupted by additive noise may be achieved by passing the signal and noise through an adaptive filter that suppresses the noise while leaving the signal relatively unchanged. Such filters are designed in the domain of optimal filtering[42, 33]. If *a priori* knowledge of both signal and noise

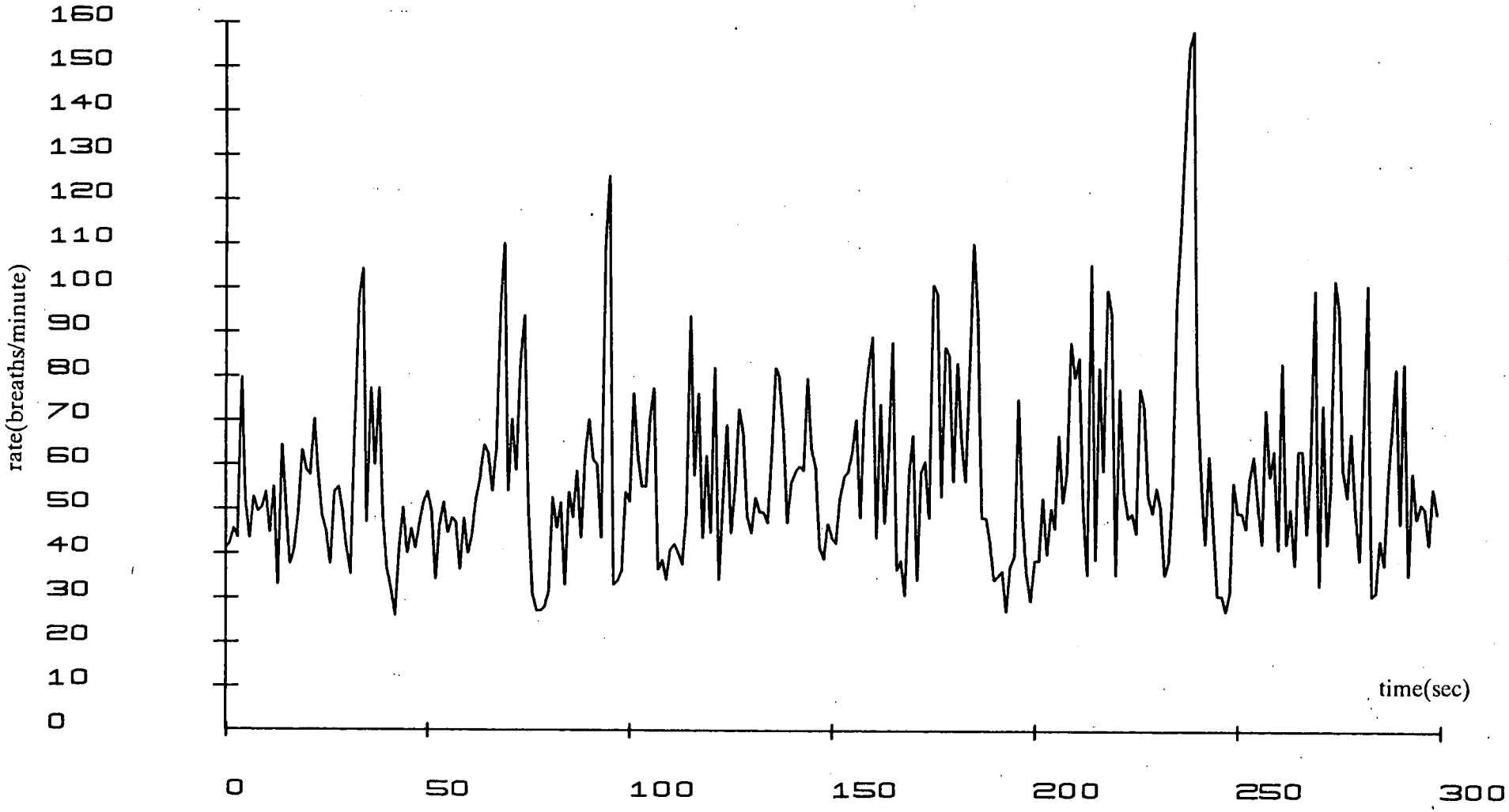

Figure 5.10: Estimated fetal breathing rate.

characteristics exist then fixed filters may be used, otherwise the filter must have the ability to change its parameters adaptively. The enhancement of signal in presence of broad band noise is called adaptive line enhancement (ALE). ALE is performed using the LMS algorithm[61, 62, 42].

Basically, the ALE structure decorrelates the broad band noise by using a delayed version of the desired signal as the reference signal, figure 5.11. When trying to reveal the presence of long term rate variations, the short term variations which are visually predominant (figure 5.10) may be regarded as noise added to the long term variations.

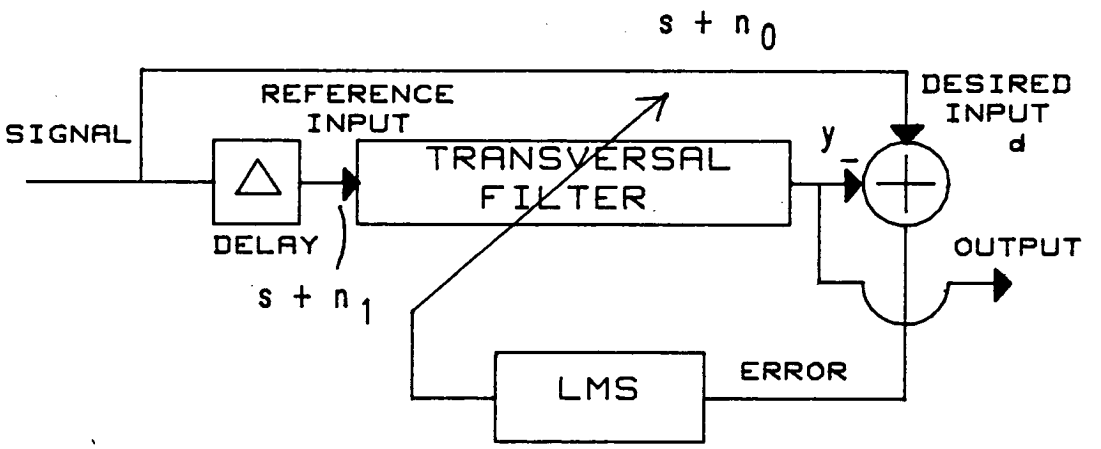

Figure 5.11: Adaptive line enhancer (ALE).

The input comprises the signal s and n_1. The noise at the desired input n_0 is the decorrelated input noise. The assumption is made that s, n_0, n_1 and y are statistically stationary with zero mean and that the noise is white. Then due to the delay, we can also assume that s is uncorrelated with n_0 and n_1, and s is correlated with y. Also n_0 and n_1 are uncorrelated as a result of the noise being white. The error output of the filter was shown in equation 4.11 to be the difference of the signal estimate and the desired signal input.

$$\epsilon = s + n_0 - y \tag{5.1}$$

$$\epsilon^2 = n_0^2 + (s-y)^2 + 2n_0(s-y) \tag{5.2}$$

Taking expectation of both sides for mean-squared-error and realising that the noise component n_0 is uncorrelated with s and y yields:

$$\begin{aligned} E\{\epsilon^2\} &= E\{n_0^2\} + E\{(s-y)^2\} + 2E\{n_0(s-y)\} \\ &= E\{n_0^2\} + E\{(s-y)^2\} \end{aligned} \tag{5.3}$$

Minimising the MSE does not affect the first term of eq. (5.4) which is the power of the input noise, σ_0^2.

$$E_{\min}\{\epsilon^2\} = \sigma_0^2 + E_{\min}\{(s-y)^2\} \tag{5.4}$$

When the second term of eq. (5.4) is minimised, then the filter output y is a best least-squares estimate of the input signal s. The filter tap adjustments for the ALE configuration (fig. 5.8) are achieved using the LMS algorithm discused in chapter 4.

The value of the delay, in the ALE structure, must be large enough to ensure decorrelation between the noise components at the reference and desired inputs of the filter. Only a unit delay is really necessary if the noise is white.

5.6. RESULTS AND DISCUSSIONS

Figure 5.10 presents the output of the peak tracking algorithm for a 300 second duration block of data. FBM varied from about 30 breaths per minute up to 120 breaths per minute. On one occasion FBM rate is seen to go up to 160 breaths per minute. FHR is known to vary between 90 and 200 beats per minute with a signal intensity about 40 db below the intensity of the FBM signal. During this episode of high FBM rate the intensity of FBM was high which discounts the possibility of confusing the two activities.

Figure 5.12 depicts the spectral density of the estimated FBM rate. This reveals the presence of many peaks which may be due to short term fluctuations in

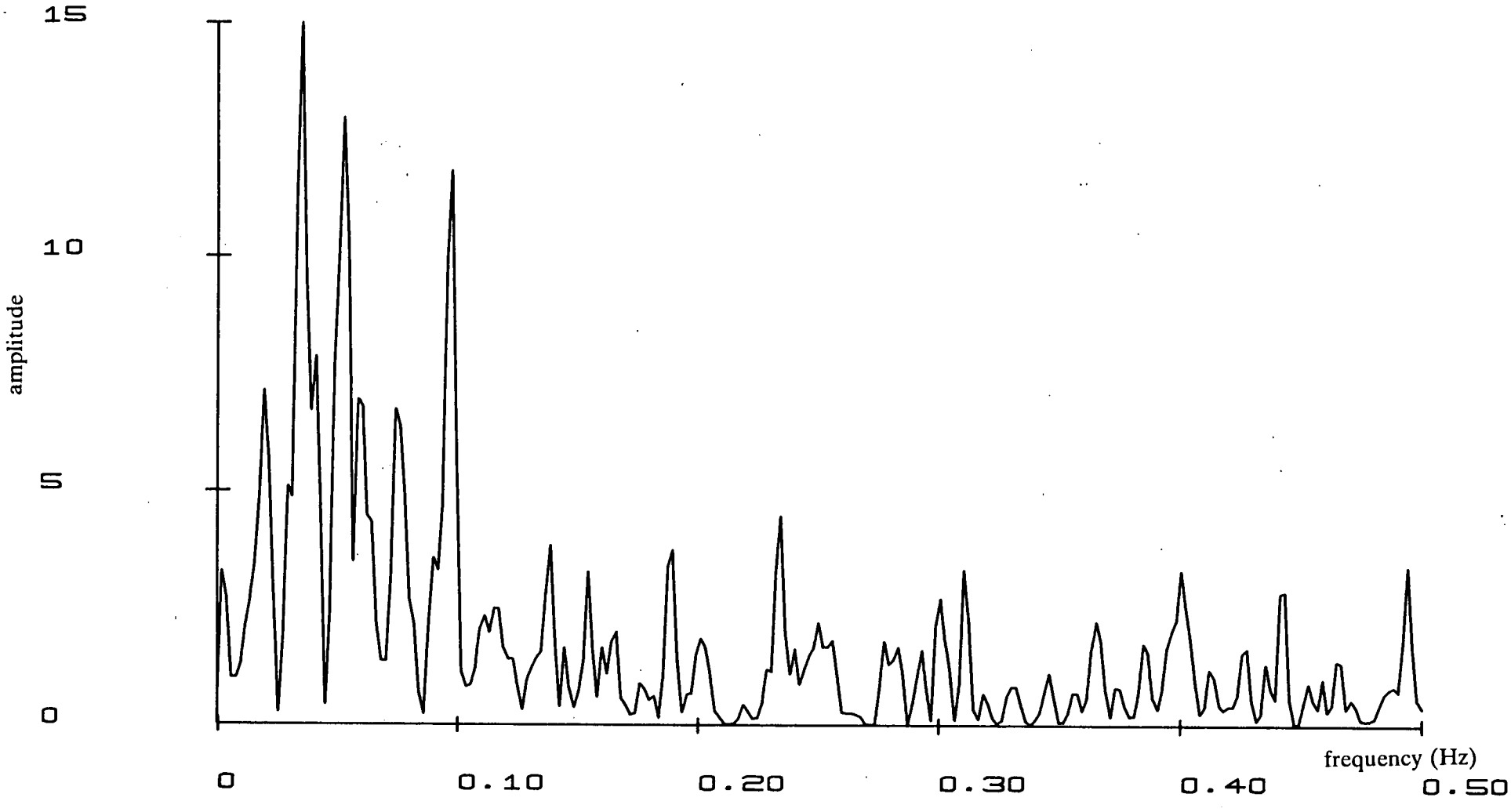

Figure 5.12: FFT of the unfiltered estimate of FBM rate.

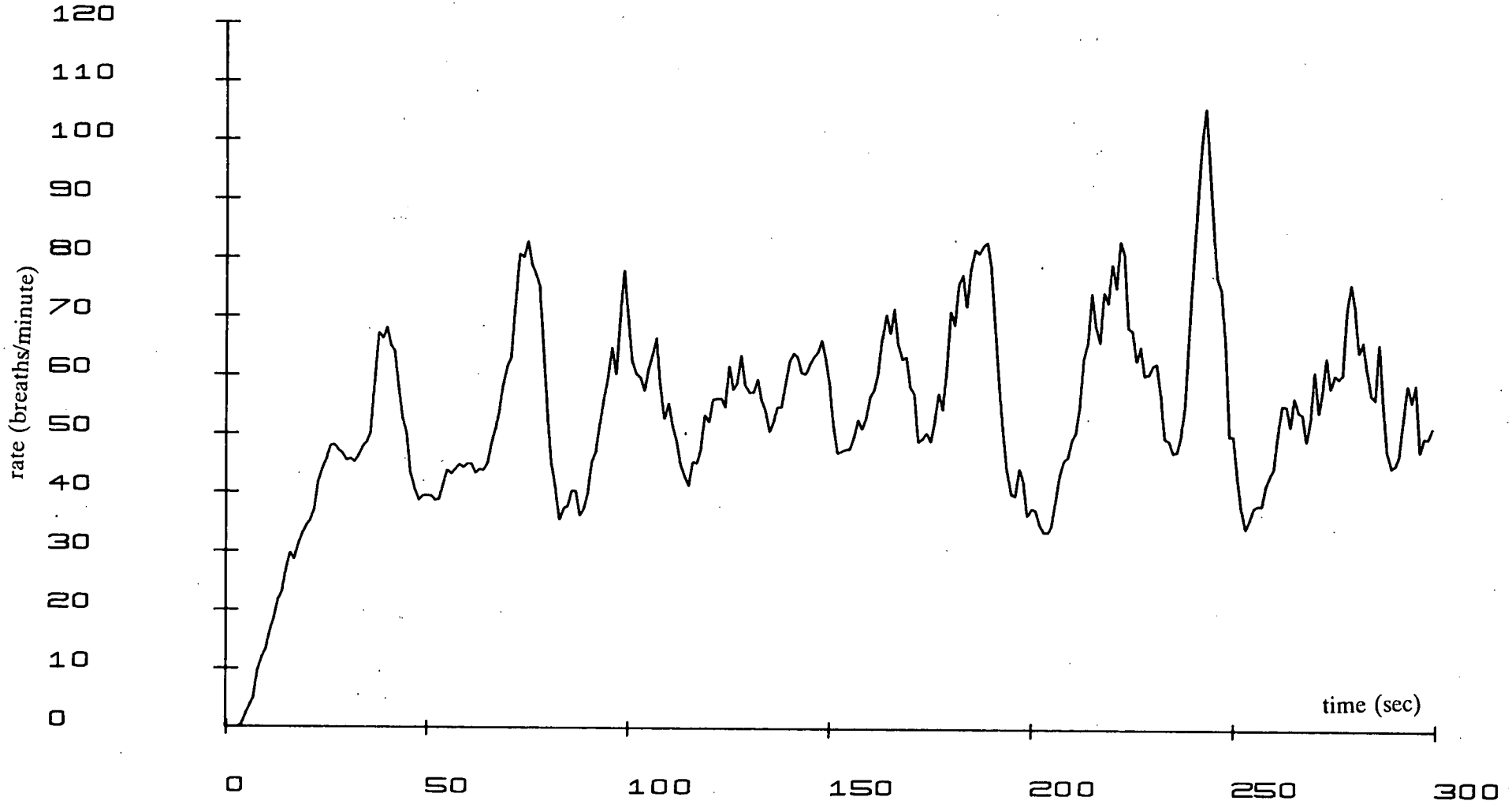

Figure 5.13: Filtered FBM rate using ALE, filter length = 10, adaptation time = 20, delay = 5

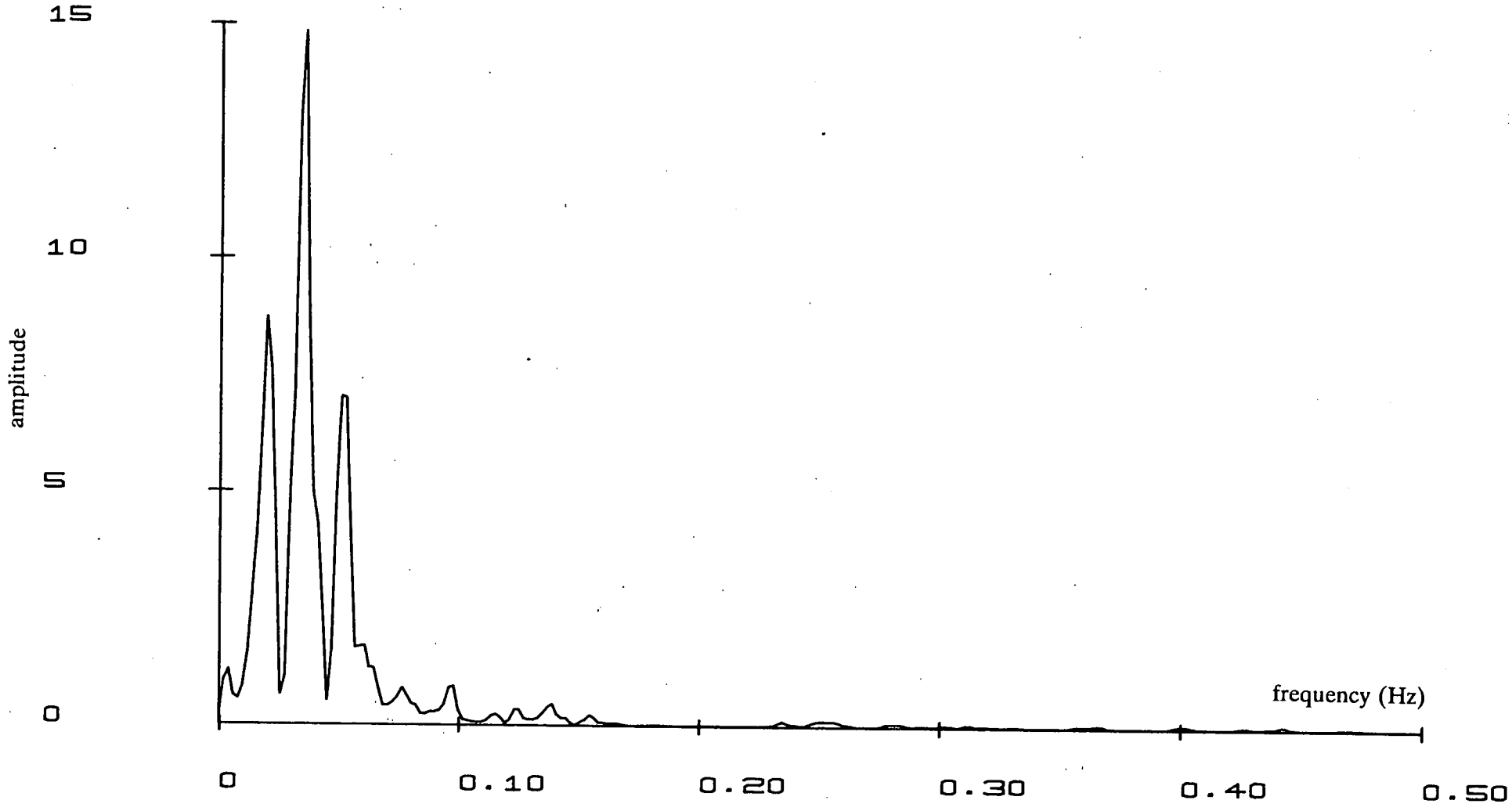

Figure 5.14: FFT of the filtered estimate of FBM rate.

FBM rate or due to noise. Filtering the 'raw' FBM rate signal which is represented in figure 5.10 using adaptive line enhancement techniques, cancels the effect of noise and short term fluctuations from the signal. The result is shown in figure 5.13. The adaptive line enhancement reveals underlying periodicities in the signal as shown in figure 5.14. Short term periodicities of 0.04 Hz (25 seconds) can be measured from figure 5.14. This periodicity does not appear to have been reported previously in the literature.

5.7. SUMMARY

This chapter has outlined the general principles and structures of expert systems. Specifically the expert system is used to track peaks pertinent to FBM rate in the presence of noise. The expert system was developed on the basis of rule based knowledge having also fuzzy sets and logic.

Estimates of FBM rate were successfully achieved using the expert system and results were presented. Adaptive line enhancement of the output of the peak tracking algorithm illustrated the presence of underlying periodicities in FBM rate similar to periodicities in FHR[63].

CHAPTER 6

RECOGNITION OF NORMAL AND DEVIANT FETAL BREATHING PATTERNS

6.1. INTRODUCTION

In the last chapter, an expert system was used to estimate FBM rate by spectral peak tracking based on overlapping data blocks of two second duration. The knowledge base of the expert system was built to estimate FBM rate for normal breathing patterns. These normal breathing patterns comprise inspiratory movements followed by expiratory movements. During the course of this research, a new fetal breathing pattern was identified. This new pattern was observed to have a short breathing cycle instantiated in the inspiratory and expiratory movements of the main breathing cycle. The intensity of this intermediate cycle was observed to be less than that of the main cycle. These patterns were named "deviant breaths" or "deviant patterns". If one looks at fetal breathing in the same light as adult breathing or neonatal breathing, then it is possible to think of these deviant FBM patterns as being "augmented breaths". In this chapter, detection of these new patterns is outlined.

Pattern recognition algorithms are used here to classify fetal breathing patterns as "normal" or "deviant". In this chapter the principles of pattern recognition are outlined. Statistical classification using multivariate statistical analysis, and classifica-

tion using neural network are discussed in detail.

Finally, the performances of the different classification techniques are compared and presented in tabulated form.

6.2. PATTERN RECOGNITION

Pattern recognition [64, 65, 66]. may be divided into two application categories, recognition of concrete objects e.g. pictures, shapes, music etc. and recognition of abstract objects e.g. an argument or a solution etc. This chapter is only concerned with the recognition of concrete objects, in this case fetal breathing movements.

The recognition of concrete objects by humans may be regarded as a psychophysiological problem which involves certain interdependences between the person carrying out the recognition and the physical stimulus generated by the object. When a person perceives a visual pattern, an inductive inferencing process is carried out which relates the perceived object with some general concept derived from past experience. In reality, human pattern recognition is a matter of decision making and classification of an object to one of a number of predetermined population groupings.

This chapter is concerned primarily with automatic pattern recognition systems. The operation of the system may be divided into three tasks: data acquisition (transduction), feature extraction and selection, and finally classification. Data acquisition was discussed in chapter 3 and was achieved using a PVDF transducer. The PVDF transducer converted physiological movements to electrical signals, which were represented in the computer by a sequence of numbers. In this chapter, feature extraction, selection and classification techniques are discussed.

6.3. THE REPRESENTATION OF A PATTERN IN A FEATURE SPACE

An observation is a set of measurements containing relatively large amounts of data describing a given pattern. Often, the information content of such observations is much smaller than the relative size of the data vector used to describe the pattern. Certain key features pertaining to the pattern can often be abstracted in order to increase the ratio of the amount of information to the size of the data. Feature selection is a mapping process of the observation from a higher-dimension to a lower dimension, with minimal loss of information. This reduction in dimensionality (vector length) makes the classification process computationally faster and less complex. The feature vector comprises several different attributes which are characteristics of the individual object it represents. This type of data representation and analysis is classed as multivariate data analysis. Multivariate analysis simultaneously considers with equal importance each variate within the multivariate structure.

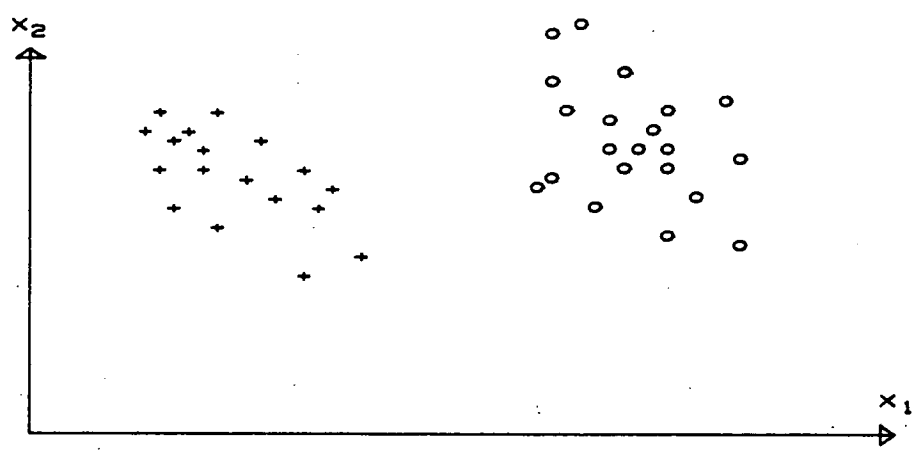

Figure 6.1: Two dimensional feature space.

A feature vector may be regarded as representing a point in an n-dimensional Euclidean space, where n is the number of attributes in the feature vector. A set of feature vectors belonging to the same group correspond to an ensemble of points

scattered within a confined region of feature space. Figure 6.1 shows a 2-dimensional feature space with two groups and two attributes (x_1 and x_2). For representation purposes, two dimensional feature space is considered, because this is easier to represent and visualise than higher dimensions.

The ultimate objective in feature extraction is to minimise the number of attributes representing an object, while making sure information loss is acceptable and kept to a minimum. Feature vectors must have the following characteristic:

a) Discriminant qualities: Features should have significantly different characteristic values for patterns belonging to different classes, and similar characteristic values for patterns belonging to the same class. Each vector is a point in an n-dimensional space, and the discriminant qualities would ideally result in disjoint sets (figure 6.1). In reality, such neatly disjoint sets may not be possible.

b) Independent features: Features which are used to describe a pattern should be uncorrelated with each other. Using two or more highly correlated features will not add much new information, and either one of these features could provide essentially the same information. An example of this could be the voltage amplitude and the power of an FBM signal. These are highly correlated, and the use of either of these attributes would provide the information regarding signal intensity. The performance of a classifier is generally degraded when correlated features are used.

c) Reduction in dimensionality: The complexity of an automatic pattern recognition system increases with the size of the feature vector. Hence, the size of the feature vector for a given pattern should represent a significant reduction in the dimensionality of the original data.

Feature extraction and selection have received considerable attention. Algorithms exist which may be used to guide the system designer in the extraction of pertinent features [65, 67]. Unfortunately, there is no clear set of rules to guide the selection of these features. However, there are commonly used features [66] that may be used to describe length, width, perimeter, shape, rectangularity, circularity etc., but in general, the selection of features are based on intuition. The general tendency is to extract a large number of features where some are not independent. These dependent features increase the dimensionality of the feature space and in most cases degrade the performance of the system. Therefore, it is necessary to identify the independent features in the vector. It is also necessary to identify the most relevant features. Feature reduction techniques are well documented[68, 69, 65], and generally use principal component and factor analysis, which are the eigenvalue and eigenvectors, to map the feature onto a new space.

6.3.1. FEATURE SELECTION FOR FBM PATTERNS

Prior to selecting features for the two fetal breathing movement patterns discussed, the characterising features of the deviant pattern must be defined. In the absence of a definition for these deviant patterns, the following definition was used:

> *A normal breathing pattern comprises an inspiratory movement followed by an expiratory movement. The relative expanse of the two movements should be approximately equal. A deviant breath is one that has two breathing patterns augmented to form a single breathing cycle. The intensity of the intermediatory pattern, must be less than that for the main breathing cycle. In other words, a deviant breathing pattern comprises four movements with the expanse of the two consecutive movements in the middle being significantly smaller than the outer two.*

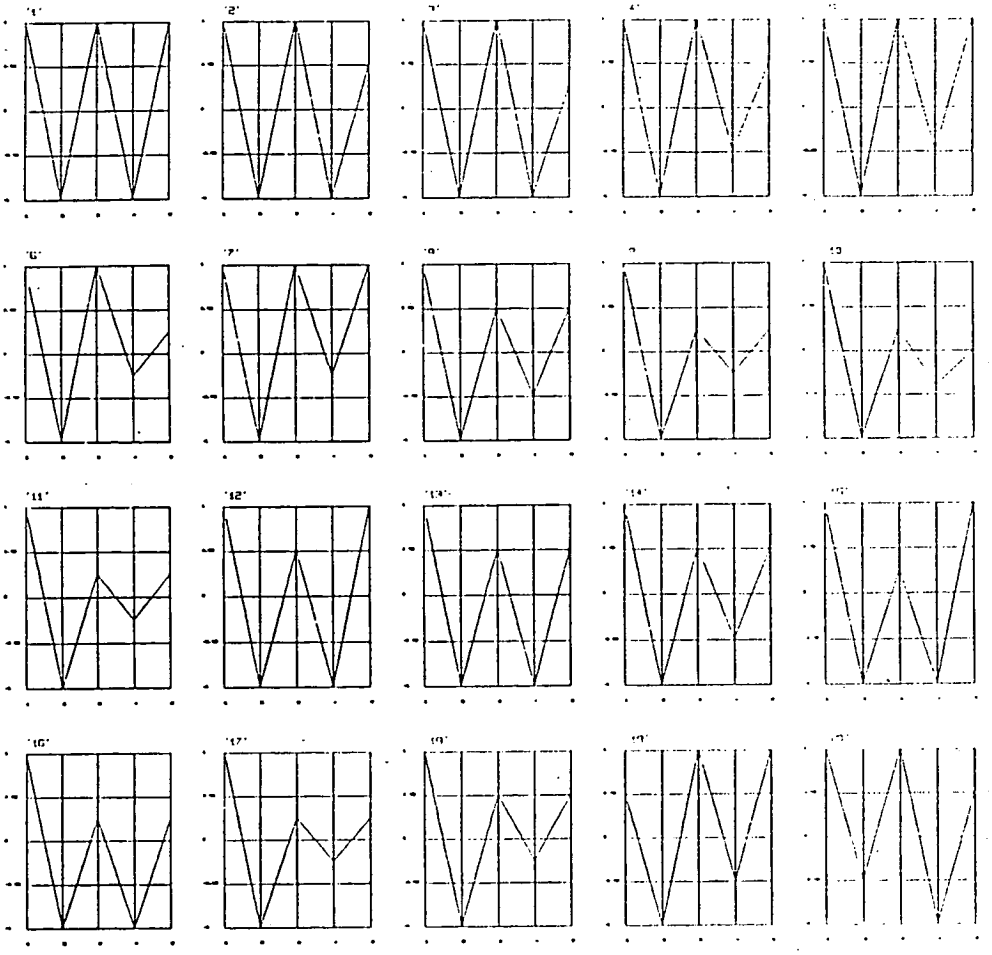

Figure 6.2:Templates of normal breathing patterns based on a feature set comprising the normalised amplitudes of 5 consecutive turning points.

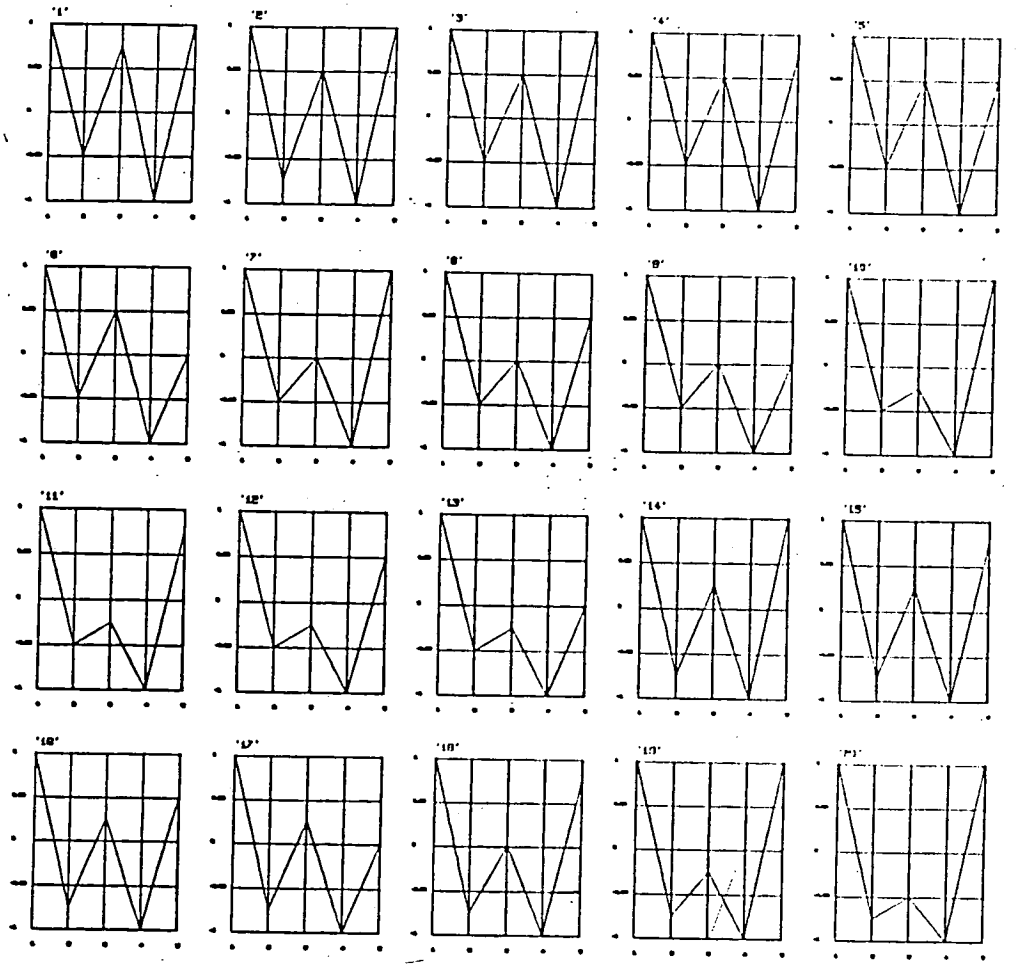

Figure 6.3:Templates of deviant breathing patterns based on a feature set comprising the normalised amplitudes of 5 consecutive turning points.

For the detection of deviant breathing patterns, a time window is used similar to the one used in AR spectral analysis outlined in chapter 4. The length of the window was not of fixed time duration, but was dictated by the duration of five consecutive turning points. These turning points represent the points of maximum inhalation and exhalation. The use of common features, e.g. shape etc., was examined, and found not to possess the desirable characteristics outlined in sec. 6.3. However, The amplitudes of the five turning points in the window were found to constitute suitable feature set. It is hypothesised that a trained observer would use these features when detecting deviant patterns. Knowledge of the time base between these turning points was found not to contribute significantly towards an improved classification of the patterns, and hence timing information was not considered. Figures 6.2 shows some examples of normal patterns and figure 6.3 shows some example of deviant patterns.

6.4. CLASSIFICATION

There are basically three different modes in a classification process. Mainly learning, testing and usage. In the next sections, these three modes are clarified:

6.4.1. TRAINING (LEARNING) MODE

Before assigning an unknown pattern to some predefined group or class, the automatic pattern recognition system must learn the properties of the different classes in the n-dimensional space, where n is the dimension of the feature vector. The classifier learns these properties using a set of feature vectors, called training samples or the training set. The training set is used to "teach" the system the properties of each group. It is important to bear in mind that the training process takes place only during the design stage of an automatic pattern recognition system, and only the properties deduced from the training samples are used. Training may take

different forms depending on the *a priori* knowledge about the training samples. Principally these are:

a) Supervised training: In supervised training it is assumed that the class memberships of the training samples are known. With this *a priori* knowledge the system develops some quantitative properties for each group. These properties are totally dependent on the pre-assignment of the training samples and how well they represent the different groups.

b) Unsupervised training: In some applications, *a priori* knowledge of class memberships is not available. Additionally, the number of groups may also be unknown. In such cases, it is desirable to determine the different possible groupings from the available data. There exist algorithms which cluster together feature vectors whose properties are closely similar. This process is known as cluster analysis,[64, 65].

6.4.2. TEST MODE

After training, some method of evaluating the performance of the classifier is required. There are several methods of doing this. In all of these methods, the system is tested on a set of features vectors (the "test set") whose class memberships are known *a priori*.

Testing provides error rate measurement which may be used as a yard-stick for performance evaluation. The error rate may be used as a forecast of performance when classifying unknown observations. Some of the many methods of estimating the error rate, [66, 65, 70] are:

a) Actual error rate: To evaluate classifier performance, the test features used for the evaluation, are different from those used to train the system. The error rate is estimated as the percentage of features misclassified in relation to the

total size of the training set.

b) Apparent error rate: This method uses the training features to test the performance of the classifier. Since the same samples are used for both training and testing, then obviously the resulting misclassification rate estimate shall be lower than the true error rate. This false impression of a good performance may lead to disappointment when the system is used on unknown data. Nevertheless, the apparent error rate provides an idea of the best possible performance achievable by the system.

c) Leave-one-out method: This method uses the training features as the testing features but in a different manner to that used in estimating the apparent error rate in method (a) above. Assume there are M samples in the training set. The leave-one-out method uses M-1 samples for training and uses the remaining sample for testing. This procedure is repeated M times, leaving out a different sample each time. When the classifier ahs been tested for every case, then the error rate is estimated as the number of misclassifications divided by the size of the set M.

6.4.3. USE MODE

Once the training phase is satisfactorily completed and the performance is estimated, then the system is applied to the task for which it was designed. The performance of the system is largely dependent on the choice of training set and how well it resembles the actual unknown data.

6.5. CLASSIFICATION ALGORITHMS

The main design task is to define some criteria by which a new observation may be correctly assigned to one of a number of possible groups. There are a number of algorithms which may be used for classification purposes, and the

following examples are discussed in the proceeding section:

1 Statistical classification algorithms.

a) Bayesian discriminant functions (Quadratic and linear).

b) Distance measurement functions (Euclidean and Mahalanobis distances).

2 Deterministic Approach.

a) Artificial Neural Network.

6.5.1. STATISTICAL CLASSIFICATIONS

Characteristically multivariate analysis may be applied to a large set of observations, where there are n features per observation. The most basic concept of multivariate analysis is the idea of a multivariate probability distribution in which the decision making process may be considered as a statistical problem[70, 68, 64, 65, 69]. There are many strategies which may be used for this solution. The Bayesian discriminant and distance measurement approach will now be described:

6.5.1.1. BAYESIAN DISCRIMINANT FUNCTIONS

In statistical methods, conditional probabilities can be used to summarise any information regarding an event (P(A|B) = probability of event A given that B has occurred). The Bayes' decision rule assigns an object to the class (or group) with the highest conditional probability. If there is an observation, denoted by vector **X**, and there are m groups to which this observation may belong, then the Bayes' rule assigns the observation to group G_i provided:

$$P(G_i|\mathbf{X}) > P(G_j|\mathbf{X}) \quad \text{for all } i \neq j \tag{6.1}$$

It is very difficult to find the *a posteriori* probability of G_i ($P(G_i|\mathbf{X})$). On the other hand, it is easier to find $P(\mathbf{X}|G_i)$, the probability of a feature vector **X** given

that it belongs to group G_i. Equation (6.2) shows the relationship between the two conditional probabilities[67, 65].

$$P(G_i|\mathbf{X}) = \frac{P(\mathbf{X}|G_i)\,P(G_i)}{P(\mathbf{X})} \tag{6.2}$$

Applying eq.(6.2) to eq.(6.1) results in:

$$P(\mathbf{X}|G_i)\,P(G_i) > P(\mathbf{X}|G_j)\,P(G_j) \quad \text{for all} \quad j \neq i \tag{6.3}$$

If the population is assumed to be governed by a multivariate normal density function with a distribution:

$$\frac{1}{(2\pi)^{n/2}|\mathbf{C}^{1/2}|}\exp[\,-\tfrac{1}{2}(\mathbf{X}-\mu)^T\mathbf{C}^{-1}(\mathbf{X}-\mu)] \tag{6.4}$$

Where:

X is the point in multidimensional space

C is the Covariance matrix

μ is the mean vector

n is the size of the feature vector (number of attributes)

Then:

$$P(\mathbf{X}|G_i) = \frac{1}{(2\pi)^{n/2}|\mathbf{C}_i^{1/2}|}\exp[\,-\tfrac{1}{2}(\mathbf{X}-\mu_i)^T\mathbf{C}_i^{-1}(\mathbf{X}-\mu_i)] \tag{6.5}$$

The above expression for $P(\mathbf{X}|G_i)$ reduces the problem of classification in eq.(6.3) to estimates of group covariance matrix, $\mathbf{C}_i$, and group mean vector, μ_i. Estimation of the covariance matrix and the mean vector for all the groups provide information pertaining to the shape and size and the position of the groups in n-dimensional space. The mean vector, μ_i, indicates the centre of the distribution for group i in an n-dimensional space. The diagonal terms of the covariance matrix indicate the spread in each direction, and the off diagonal terms are a measure of association (correlation) between the variables.

Using the normal density function, eq.(6.3) yields:

$$\frac{P(G_i)}{(2\pi)^{n/2}|C_i^{1/2}|}\exp[\ -\tfrac{1}{2}(X-\mu_i)^T C_i^{-1}(X-\mu_i)] > \frac{P(G_j)}{(2\pi)^{n/2}|C_j^{1/2}|}\exp[\ -\tfrac{1}{2}(X-\mu_j)^T C_j^{-1}(X-\mu_j)] \quad (6.6)$$

If eq.(6.6) is true then observation $\mathbf{X}$ is assigned to group G_i.

Taking natural logs of both sides of the inequality (6.6) yields:

$$\ln|C_i| + (X-\mu_i)^T C_i^{-1}(X-\mu_i) - \ln(p(G_i)) < \ln|C_j| + (X-\mu_j)^T C_j^{-1}(X-\mu_j) - \ln(p(G_j)) \quad (6.7)$$
$$\text{for all } i \neq j$$

The decision function of eq.(6.7) is a hyper-quadratic one. This is because no terms higher than second order of $\mathbf{X}$ appear in these equations. This implies that the best a Bayes' classifier can do is place a second order decision surface between each pair of classes. Furthermore, if the classes are truly characterised by normal densities, then there is no other decision surface which can perform better. This is by virtue of the fact that normal distribution was used to derive the decision boundary. Equation (6.7) is called a quadratic discriminant function.

If the covariance matrices for all the groups are assumed equal, $C_i = C$, then the Bayes' decision rule reduces to[67, 65, 70]:

$$\mu_i^T C^{-1} X - \tfrac{1}{2}\mu_i^T C^{-1}\mu_i + \ln(P(G_i)) > \mu_j^T C^{-1} X - \tfrac{1}{2}\mu_j^T C^{-1}\mu_j + \ln(P(G_j)) \quad (6.8)$$

The decision function of eq.(6.8) is a linear function of $\mathbf{X}$.

Statistical classification using Bayes' quadratic or linear decision boundaries provides some metric whereby an observation may be assigned to a predefined group. The equation for the quadratic function comprises two parts: one part has the units of distance squared; the other part is the logarithm of the volume of the n-dimensional ellipsoid ($\ln|C_i|$). For the linear decision function case, this latter

variable is assumed equal for all the groups and cancels out.

6.5.1.2. DISTANCE MEASUREMENT

A number of methods can be used to measure the distance between two points $\mathbf{X}_1$ and $\mathbf{X}_2$ in an n-dimensional Euclidean space. The simplest measure is the Euclidean distance:

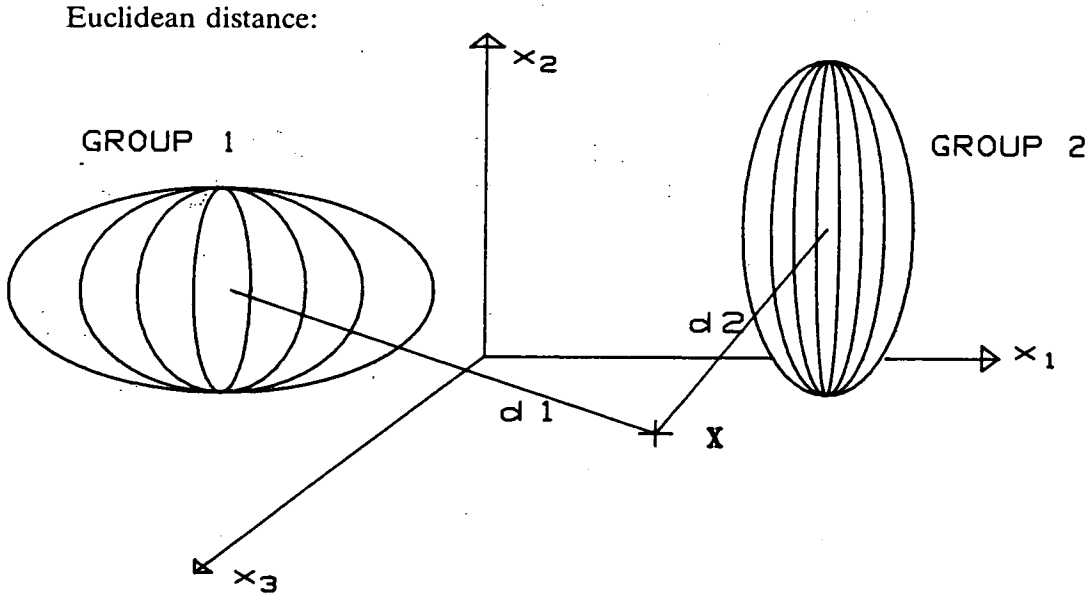

Figure 6.4: Three dimensional feature space.

$$D_E^2 = (\mathbf{X}_1 - \mathbf{X}_2)^T (\mathbf{X}_1 - \mathbf{X}_2) \tag{6.9}$$

When measuring distances between a multivariate population and a point in an n-dimensional space, (figure 6.4), the Euclidean distance provides some measure of the distance between the point and the mean of the population.

$$D_E^2 = (\mathbf{X}_1 - \mu_i)^T (\mathbf{X}_1 - \mu_i) \tag{6.10}$$

The distance metric of equation (6.10) does not take into consideration the shape of the distribution, or possible correlation between the features. In Euclidean distance measurement, two highly correlated features individually contribute the same value to the distance measurement as a third independent feature. The Mahalanobis distance measurement [65, 67, 68] takes into account the correlation

between all the features in the feature space (equation (6.11)):

$$D_M^2 = (\mathbf{X}_1 - \mu_i)^T \mathbf{C}_i^{-1} (\mathbf{X}_1 - \mu_i) \qquad (6.11)$$

The Mahalanobis distance, D_M^2, may be thought as the distance of an observation $\mathbf{X}$ from the centre of a multivariate distribution taking into account the effect of all the variables and their possible correlations. The Mahalanobis distance can also be considered as the distance to the centre of a group, with this distance normalised to a unit covariance along each direction.

For both discriminant functions (sec. 6.5.1.1) and distance measurement (sec. 6.5.1.2), the population distributions are considered multivariate normal. For normal distributions, the Mahalanobis distance, D_M^2, follows the Chi-squared distribution with n-degrees of freedom. A significantly large value of D_M^2 corresponds to an observation which is unlikely to belong to that particular population. If there is more than one preclassified group, then the assignment of the observation is to the group with the smallest Mahalanobis distance.

6.5.2. DETERMINISTIC APPROACH

So far, we have discussed the design of classifiers based on direct computation of the decision boundary from estimates of the mean vector and of the covariance matrix for each class. In the deterministic approach the decision function of the classifier is generated from the training feature set by means of "iterative learning" algorithms.

Figure 6.5 introduces the concept using a 2-dimensional feature space. The decision boundary separating the two classes can be represented by:

$$\begin{aligned} d(x) &= w_0 + w_1 x_1 + w_2 x_2 \\ &= \sum_{n=0}^{2} w_n x_n \qquad \textit{where } x_0 = 1 \end{aligned} \qquad (6.12)$$

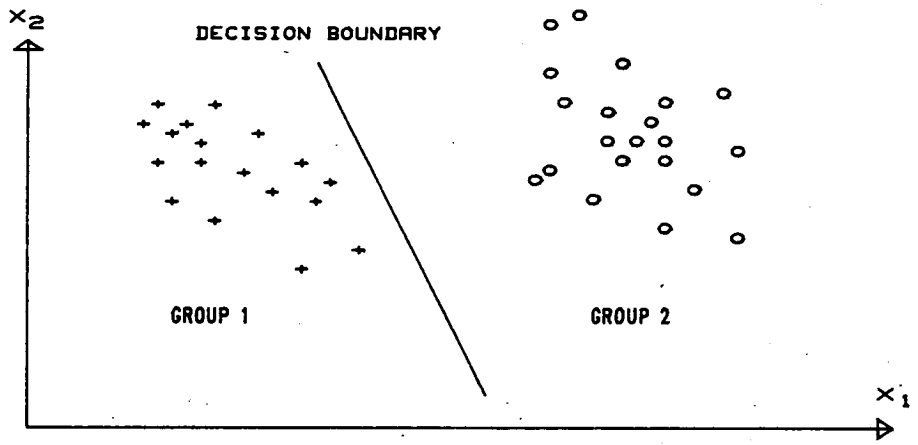

Figure 6.5: Two dimensional feature space with a decision boundary.

$$= \mathbf{W}^T\mathbf{X}$$

$\mathbf{W} = (w_0, w_1, \ldots, w_n)$ is the weight vector and n is the number of attributes in the feature vector.

In eq.(6.12), group membership is assigned by the linear decision function. After estimating the weights of the decision boundary, the observation is assigned to group 1 if:

$$d(x) > 0$$

and to group 2 if:

$$d(x) < 0$$

6.5.2.1. ARTIFICIAL NEURAL NETWORK

The above decision function may be realised using a node in a linear combiner mode [42], where the solution for the decision function is the solution to a set of linear equations (one equation in the 2-dimensional example above). A neural element is a linear combiner whose output is taken through a nonlinear limiting function (figure 6.6). Neural elements are also known as neurons[71] or perceptrons[72].

Some of the commonly used nonlinear limiting functions are: hard limiter and sigmoid functions. The output of the perceptron is in the form:

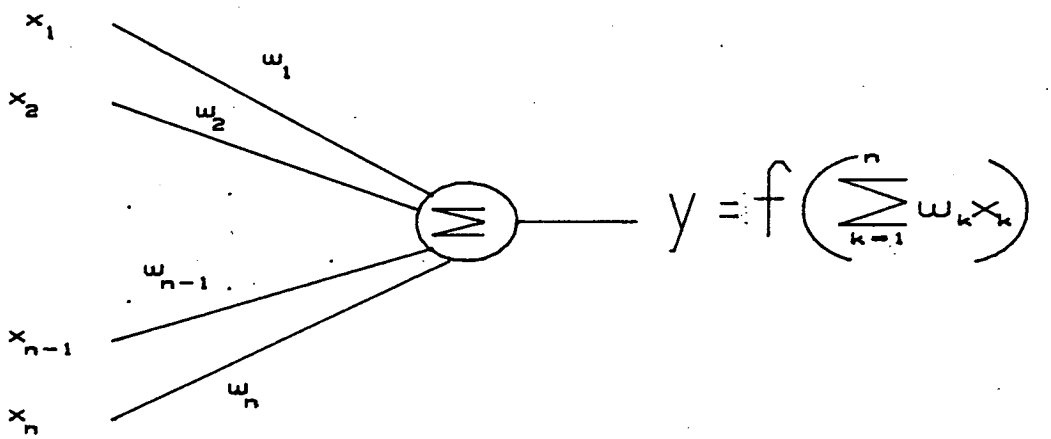

Figure 6.6: A neural element.

$$y = output = \mathbf{f}(\sum_{i=1}^{n} w_i x_i) \tag{6.13}$$

Where $\mathbf{f}()$ is the threshold function used.

A single perceptron forms two decision regions separated by a hyperplane. The equation of this hyperplane depends on the weights of the combiner and the threshold function. There are a number of different algorithms which may be used to estimate these weights. The original perceptron convergence procedure to estimate the weights was developed by Rosenblatt[72]. Widrow and Hoff[71, 72] developed a perceptron convergence algorithm based on the least-mean-square (LMS) principle. The LMS algorithm was covered in chapter 4 of this thesis.

For the case of the LMS algorithm, the perceptron may be trained using the desired input to indicate the class membership of the feature vector. A desired input of 1 indicates membership to class A while 0 indicates membership of class B. If a

bipolar threshold function is used, then 1 and -1 would indicate class memberships. A single perceptron can only discern between two groups, and complex decision boundaries may be achieved by using a multi-layered-perceptron structure (MLP)(figure 6.7). MLP comprises an input layer, an output layer and hidden (intermediate) layers.[72, 73, 71].

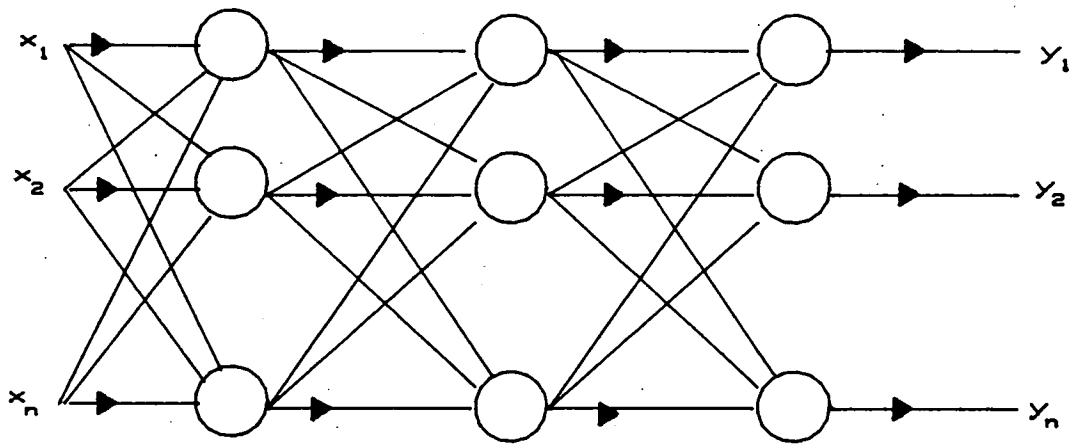

Figure 6.7: Multi-layer-perceptron (MLP).

In MLP network, the desired outcome for the entire network is the same as the desired response for the output perceptron. Therefore, given the desired response, adaptation of the output layer may be achieved using the LMS algorithm. The difficulties associated with the convergence of MLP structures lie in acquiring the desired response for the perceptrons in the hidden layers. The back-propagation algorithm was developed to estimate the desired response in the hidden layers[71, 72], and is one method which can be used to converge the weights in the hidden layers.

The back-propagation algorithm is a generalisation of the LMS algorithm. It uses a gradient search technique to minimise a cost function which is equal to mean-squared-error (MSE) between the actual output of the network and the

desired output. The desired output in this case is the *a priori* knowledge of class membership.

The MLP is trained using the back-propagation algorithm by initially selecting small random values for the weights. The training set is presented to the network repeatedly until the weights converge and the value of the cost function (MSE) is reduced to an acceptable level.

A COMPUTATIONAL PROCEDURE FOR THE BACK PROPAGATION ALGORITHM

1- Initialise weights

2- Present training set

3- Calculate the actual output using the existing weight values.

4- Adapt weights according to:

$$W_{ij}[n](t+1) = W_{ij}[n](t) + \mu\delta_j[n]x_i \tag{6.14}$$

Where $W_{ij}[n](t)$ is the value of the i^{th} weight of the j^{th} node in the n^{th} layer at the t^{th} iteration. $\delta_j[n]$ is the error of the j^{th} node in the n^{th} layer. If the output node is denoted as the k^{th} node in the m^{th} layer of the MLP structure, then for a unipolar sigmoid threshold function the error is given by:

$$\delta_j[m] = y_j[m](1-y_j[m])(d-y_j[m]) \tag{6.15}$$

Where d is the desired outcome, $y_j[m]$ is the j^{th} output of the system.

The error function for the internal j^{th} node of the n^{th} layer is given iteratively as:

$$\delta_j[n] = x_j[n](1-x_j[n])\sum_k \delta_k[n-1]W_{jk}[n] \tag{6.16}$$

Where k is over all nodes in the layers above n, connected to j^{th} node of the n^{th} layer.

Fast convergence of the weights is sometimes achieved if a momentum term, α, is added:

$$W_{ij}[n](t+1) = W_{ij}[n](t) + \mu\delta_j[n]x_i + \alpha(W_{ij}[n](t) - W_{ij}[n](t-1) \quad (6.17)$$

In the above procedure, the convergence is controlled by the adaptation gain μ, and the momentum term α which smooths the weight changes.

5- Repeat the procedure by presenting new training vector (repeat from step 2).

In the selection of the MLP structure, the number of nodes chosen must be large enough to form a complex decision region that attempts to satisfy the needs of the problem in hand. However, it must not be so large that, given the available training samples, the weights cannot be estimated reliably. The three-layer MLP has become popular due to its ability to form very complex decision regions[72], and is the neural network structure used in this chapter to classify fetal breathing movements.

6.6. PERFORMANCE EVALUATION

Classifiers based on different classification techniques were trained using thirty observations per group, and the performance of each was then evaluated using ten observations per group. The testing samples were not used in training the system. Table 6.1 presents the performance of three conventional classifiers using respectively: the equal linear Bayesian discriminant function, the non-equal quadratic Bayesian discriminant function and the Mahalanobis distance classifier. The

performance of these classifiers is presented as the percentage of features assigned to their correct groups in relation to the total number of features. The training column depicts the performance of the classifiers when the training samples are the same as those used to test the systems. The test column indicates the performance of the system after training, for the case where the testing samples used were different from those used for training. The quadratic Bayesian discriminant function seems to perform better than the other two conventional techniques. This is expected as the quadratic function takes into account the logarithm of the volume of the ellipsoid (in n_dimensional space) generated by the population distribution of each group. It is noteworthy that the assumption of normality which is required for statistical classifiers might not be strictly generally true. Despite this, the performance of the quadratic Bayesian classifier is superior to the other conventional classifiers.

Classification	Training(60)	Testing(20)
Equal Covariance Bayesian	83.3%	75%
Non-equal Covariance Bayesian	96.6%	85%
Mahalanobis	85%	75%

Table 6.1: Performance of Conventional Classification

Neural Net	Training(60)	Testing(20)
(3,3,1)	93%	80%
(3,5,1)	93%	85%
(5,3,1)	98%	90%

Table 6.2: Performance of MLP Classification (Hard Trained).

The performance of the classifiers using the neural network structure is depicted in table 6.2 and 6.3. The notation for the MLP structure is (i,j,k), where i is

Neural Net	Training(60)	Testing(20)
(3,3,1)	88.3%	90%
(3,5,1)	95%	85%
(5,3,1)	98%	90%

Table 6.3: Performance of MLP Classification (Soft Trained).

the number of perceptrons in the input layer, j is the number of perceptrons in the hidden layer and k is the number of perceptrons in the output layer. Unfortunately, definite rules to guide the selection of the structure type, the size of neural network, and other parameters do not exist. For many applications, these are selected by experimenting with different structures and learning parameters. The nonlinear threshold function used was bipolar sigmoid with +1 indicating features belonging to normal breathing patterns, and -1 indicating features belonging to the deviant patterns. In addition, two modes of training were used, hard training and soft training. With hard training, the system was trained to provide an output very close to ± 1; while with soft training the features were assigned on the polarity of the network output.

Figure 6.8 shows the convergence of the neural network for a 5-3-1 structure, and figure 6.9 depicts the corresponding tap values after convergence. This MLP structure had performed best in both training (98% matching) and testing mode (90% matching). The problem in using the neural network for pattern recognition lies in selecting the optimum structure to achieve the best performance using the available training features. In addition, due to the nonlinear properties of the neural network, the number of iterations required for convergence and the asymptotic error rate are both dependent on the initial conditions used for the tap weights.

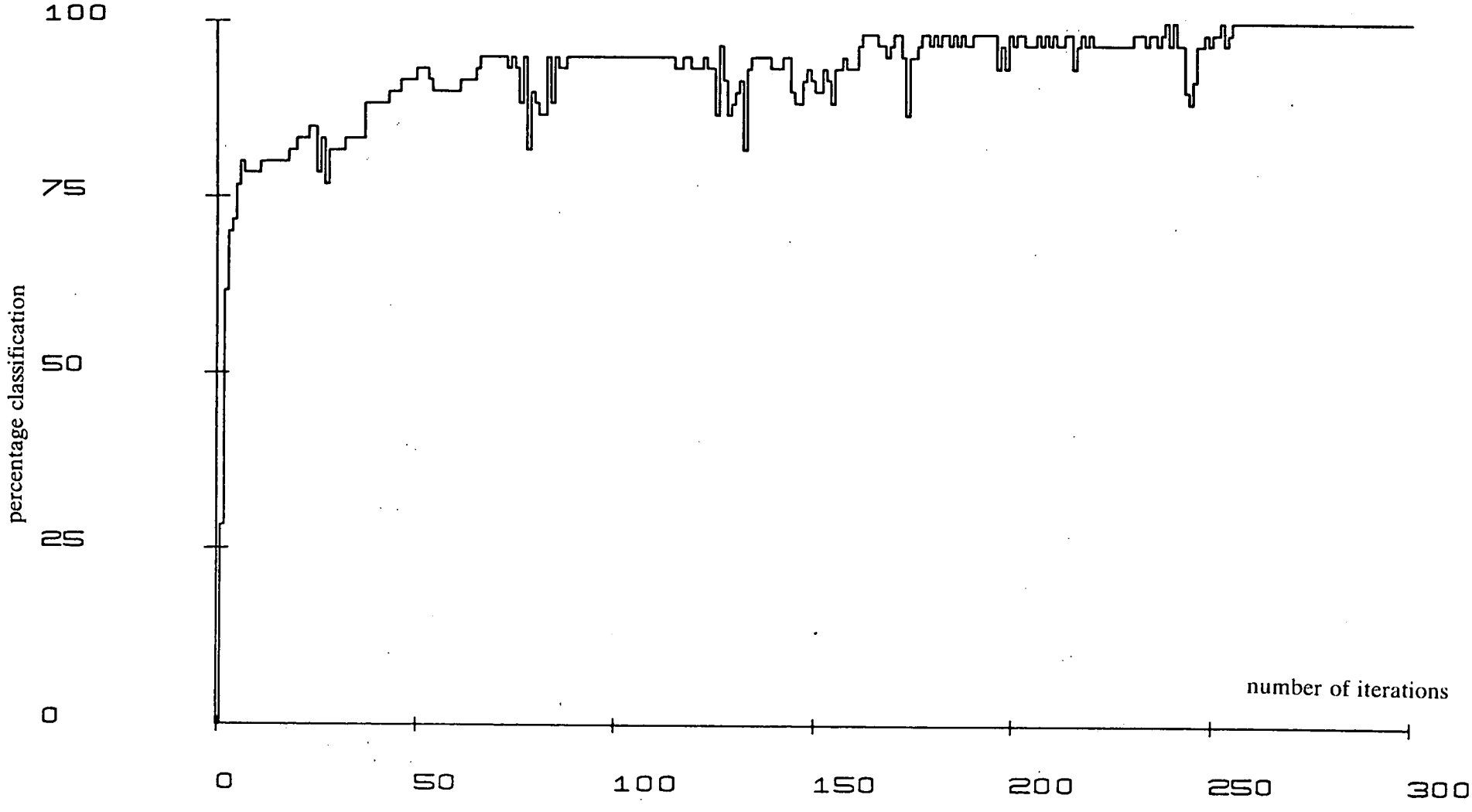

Figure 6.8: Convergence of MLP using 5,3,1 structure

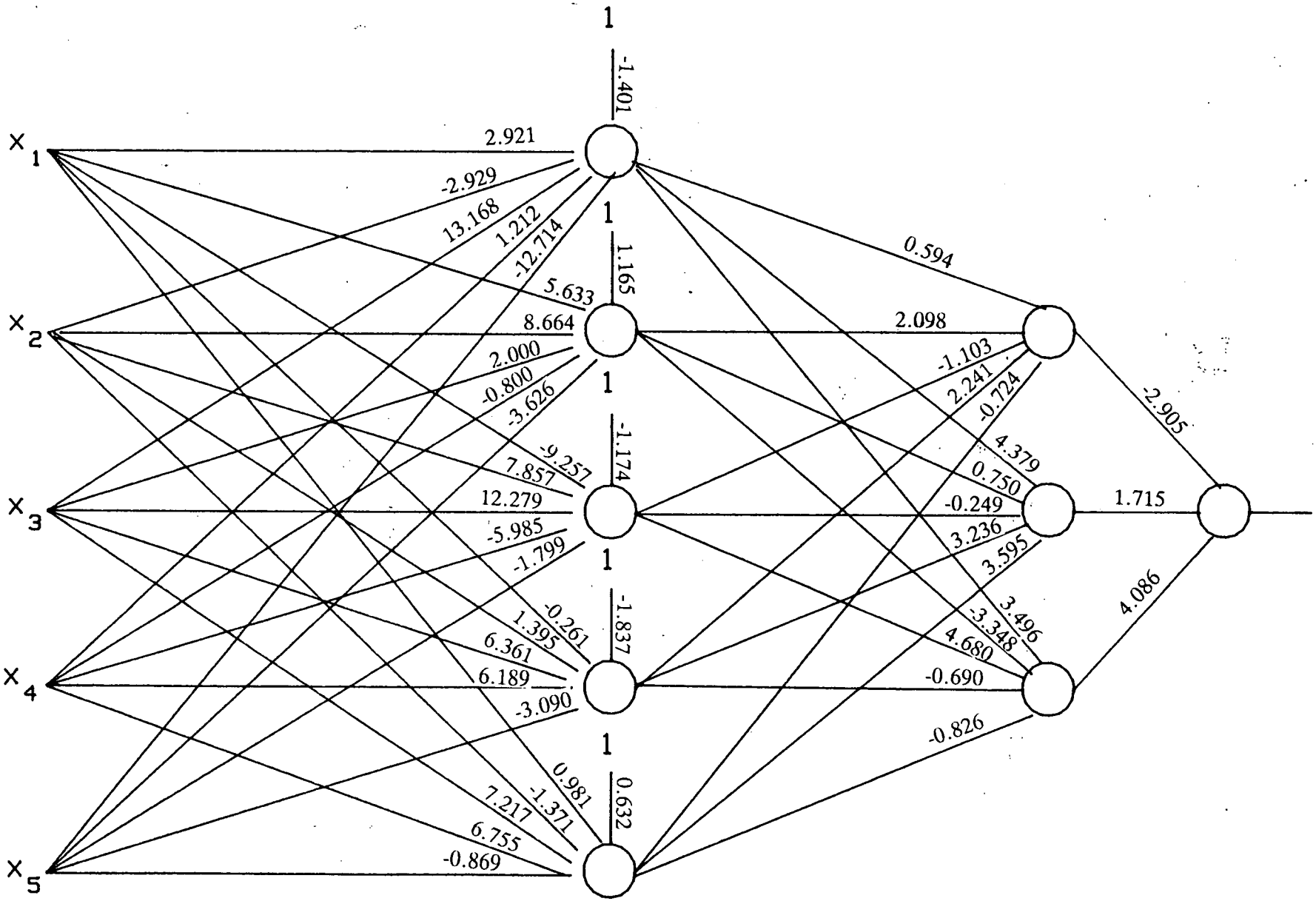

Figure 6.9: Diagram showing the tap values for a (5,3,1) MLP.

CHAPTER 7

SUMMARY AND CONCLUSIONS

7.1. SUMMARY

This thesis has investigated various digital signal processing algorithms for the analysis of fetal breathing movement. It has presented a set of algorithms which may be of clinical use in fetal antenatal monitoring,

A PVDF transducer was developed to monitor FBMs from maternal abdominal wall displacements. The transducer was also found to detect FHS which displace the maternal abdominal wall by much smaller amounts than FBMs. Although transducer compliance matching is crucial for optimum energy transfer, it was found less crucial for monitoring displacement as long as the transducer is made more compliant than the maternal abdomen. In general, the transducer was found to perform well in detecting both fetal breathing movements and heart sounds.

Analogue preprocessing was carried out on maternal abdominal wall movements. Although this thesis was mainly concerned with FBMs, the capability of the transducer to monitor both FBMs and FHS has provided a single transducer for both tasks. The preemphasis stage in the analogue preprocessing is only necessary if both FBMs and FHS are to be analysed after passing through a low resolution ADC or an analogue tape recorder. The analogue filtering has come to serve two purposes. Firstly it filters the two bands of interest as FBM rate lies mainly between 0.5

and 2.0 Hz and fetal heart sounds lie between 40 and 60 Hz. Secondly it serves as an anti-aliasing filter to ensure that signals are faithfully represented in discrete form without any corruption due to aliasing .

The analysis was carried out off line after storage on an analogue tape recorder, and the digitising process was performed using HP 5183T digitising oscilloscope. The digitised signal was down loaded to a main frame computer using an HP 210 desk top computer.

FBMs can be characterised as nonstationary signals. Spectral analysis techniques based on the FFT algorithm applied to short data blocks has its short commings due to resolution and sidelobe interference. A number of AR spectral analysis algorithms were discussed. The performance of both the gradient LMS and the optimum tapered Burg (OTB) algorithms were evaluated using simulated nonstationary signals. The LMS algorithm performed well in slightly nonstationary conditions, however, its performance deteriorated drastically when highly nonstationary signals were used. The OTB algorithm was found to exhibit the best modelling capability under highly nonstationary conditions.

FBM rate was estimated using a rule based expert system which discerned and tracked pertinent peaks in the AR spectral estimates using the OTB algorithm.

Identification of augmented breathing patterns was achieved using pattern recognition techniques. The extraction of features which represent the pattern was discussed and the performance of different classification algorithms presented. Following the current interest in neural network structures, pattern recognition using a multi layered perceptron was carried out and its performance compared with the two conventional classification techniques. The performances of the classifiers were largely dependent on the choice of the training sets and how well the chosen set resembles the actual data.

This thesis has been successful in presenting a set of algorithms for antenatal monitoring of FBMs. Analysis of FBMs using digital signal processing algorithms does not appear in the literature. At present the method of analysis is to use an ultrasound scanner and count manually the breathing movements. Therefore the work presented in thesis represents a significant advance over the present approach to FBM analysis. Also, an underlying periodicity in FBM rate has been discovered. This periodicity does not appear to have been reported previously in the literature.

7.2. CONCLUSIONS

During the course of this research interference due to maternal breathing was not found to be a problem, as gravid mothers were requested to breath gently and slowly, and to refrain from moving or talking. This control ensured that maternal breathing movement (MBM) was kept to a low rate and that harmonics of MBM were kept to a minimum. But it has been reported by Goovaerts[74] that maternal breathing rate could rise close to FBM rate and that it could have high harmonic content. However, the expert system designed could deal with these unforeseen conditions. MBM and its harmonics could be extracted using a separate chest transducer which monitors MBM only.

Another method of alleviating the interference due to the maternal components is to use an LMS adaptive transversal filter, as discussed in chapter 4 and chapter 5. To cancel the maternal components from the abdominal signal, the transversal filter uses the chest transducer output (comprising MBM and its harmonics) as the input to the filter and the abdominal transducer output (comprising FBM and its harmonics in addition to MBM and its harmonics) as the desired input to the filter as described by Widrow[62]. The error output of the transversal filter provides an FBM signal without MBM components. There are, however, some problems with this latter method. If for some reason maternal breathing was suppressed

from the abdominal signal then the transversal filter would either become unstable or the error output would contain maternal breathing and its harmonics as well as fetal components.

The transducer has also provided the possibility of simultaneously measuring of fetal heart sounds. Unfortunately the detection of FHS is localised to the anterior fetal shoulder, and if during recording, the fetus undergoes gross body movement then the detection of FHS would be lost, and consequently, the transducer must be repositioned. This could be overcome using a belt incorporating many transducers, say 6, and an algorithm can be developed which tests each transducer and chooses the output from the one which is closest to the anterior shoulder and contains the strongest FHS signal.

7.3. FUTURE WORK

This thesis was mainly concerned with investigating different algorithms for FBM analysis. The processing and analysis were successfully carried out off line, and the proposed algorithms operated disjointly.

For use in a bedside monitor, these algorithms must be adapted to operate in real time and they must be amalgamated to provide a comprehensive FBM analyser of the type proposed in figure 7.1. Prior to this the transient response of the spectral estimation algorithms must be tested for a step change in frequency, and their robustness for high noise level. Opto-isolator was used for patient safety, a transformer coupled isolator could be used to ensure a more linear performance down to DC level.

Once a real time FBM analyser is achieved, then the analyser can work in conjunction with other algorithms to develop a comprehensive fetal analyser providing the following fetal parameters:

a) Fetal breathing rate estimation.

b) Incidence of deviant breathing.

c) Fetal heart rate (FHR) estimation.

d) FHR patterns.

e) Systolic time interval estimation.

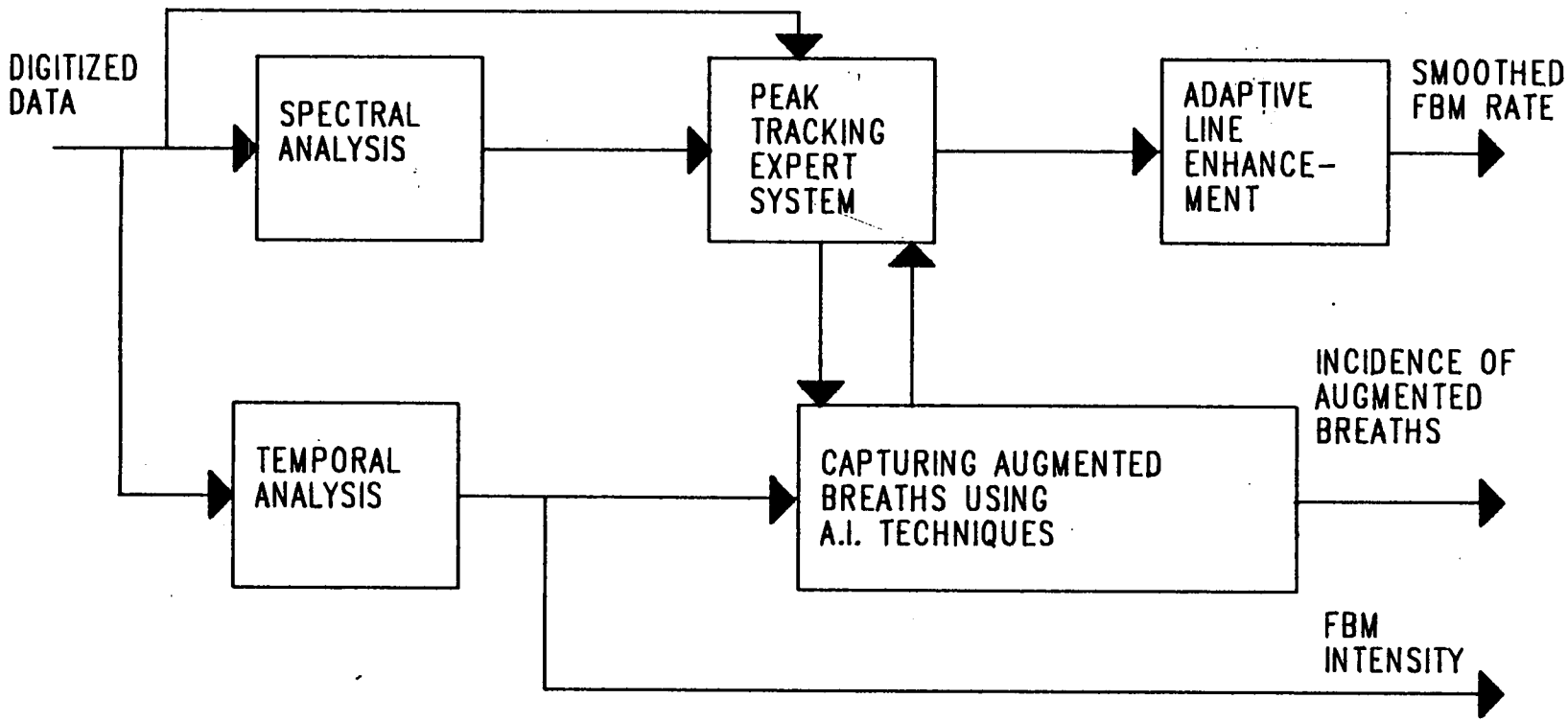

Figure 7.1: Proposed FBM analyser

APPENDIX A

PIEZO FILM

Polyvinylidene flouride (PVDF) is a semi-crystalline high molecular weight polymer. As its name suggests, it is constructed from the vinylidene flouride monomer (fig. A1). The monomer has a large dipole moment. The polymerisation of the monomer provides a structure where the "vinyl" unit (CH_2 CF_2) is repeated essentially head-to-tail (fig. A2).

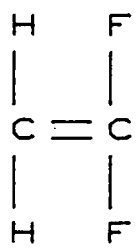

Figure A1: Monomer

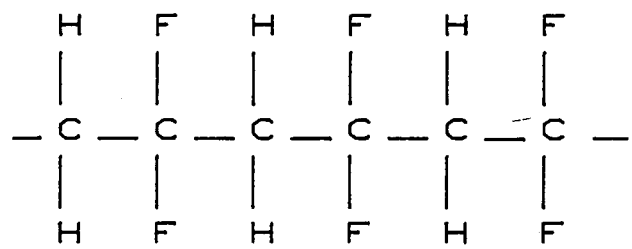

Figure A2: Vinyl polymer

The principle crystalline form of this polymer is the nonpolar α forms (fig. A3), where the dipole moments are randomly oriented with respect to each other. The non-polar α form is polarised (poled) to the highly polar β form, fig. A4. As mentioned above, poling exposes the polymer to a high electric field (~ 500 KV/cm.) at elevated temperature (~ 100° C) for an extended period followed by slow cooling. The β form has the hydrogen and flourine atoms per "unit cell" arranged to render maximum net dipole moment, hence large net polarisation.

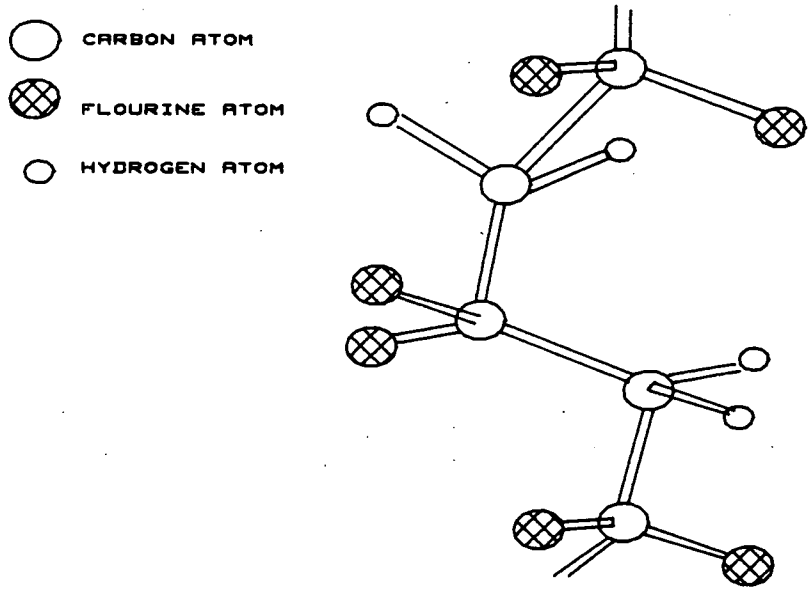

Figure A3: Nonpolar α form.

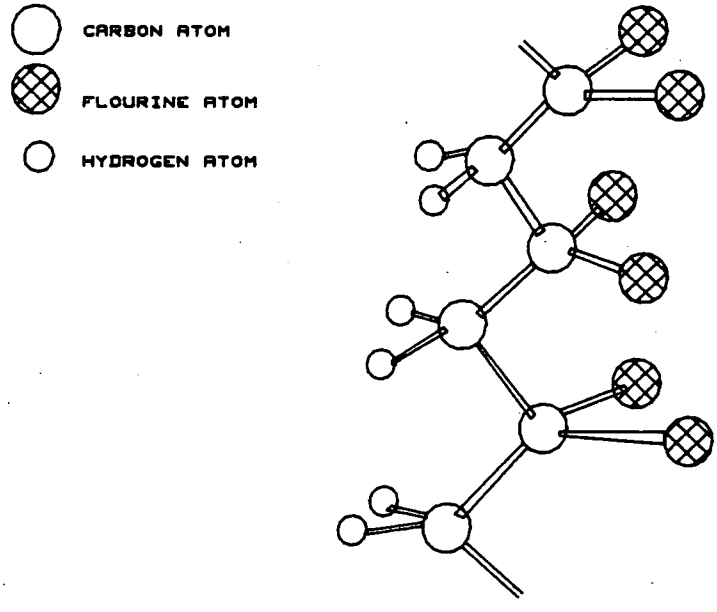

Figure A4. Polar β Forms.

The poling also aligns the β phase crystallites along the thickness direction (the direction of extrusion) fig. A5. This makes it possible to use the piezo in film sheets, by coating each side of the film. The metallisation process is essential for

removing the charge developed on the surfaces due to physical deformation of film.

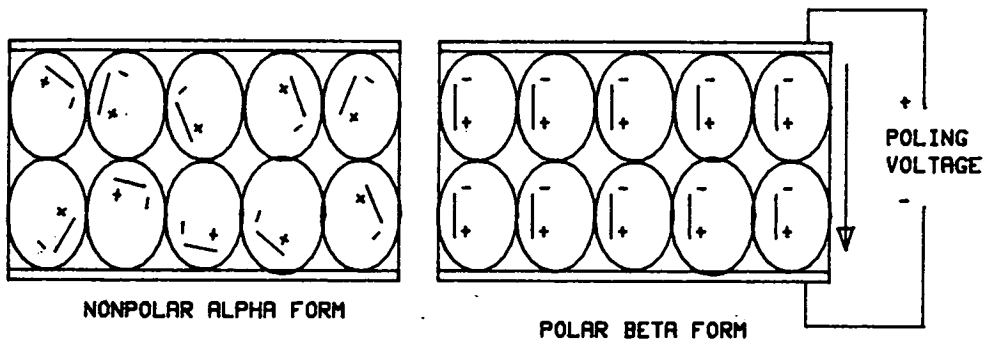

Figure A5. Dipole Alignment of α and β Forms.

APPENDIX B

CHARACTERISTICS OF PIEZOACTIVE MATERIALS

The alignment of the polymer dipoles is along the axis of poling and the orientation of the crystallite chains in the direction of stretch, render the piezo film anisotropic:- direction dependence of piezoelectric activities.

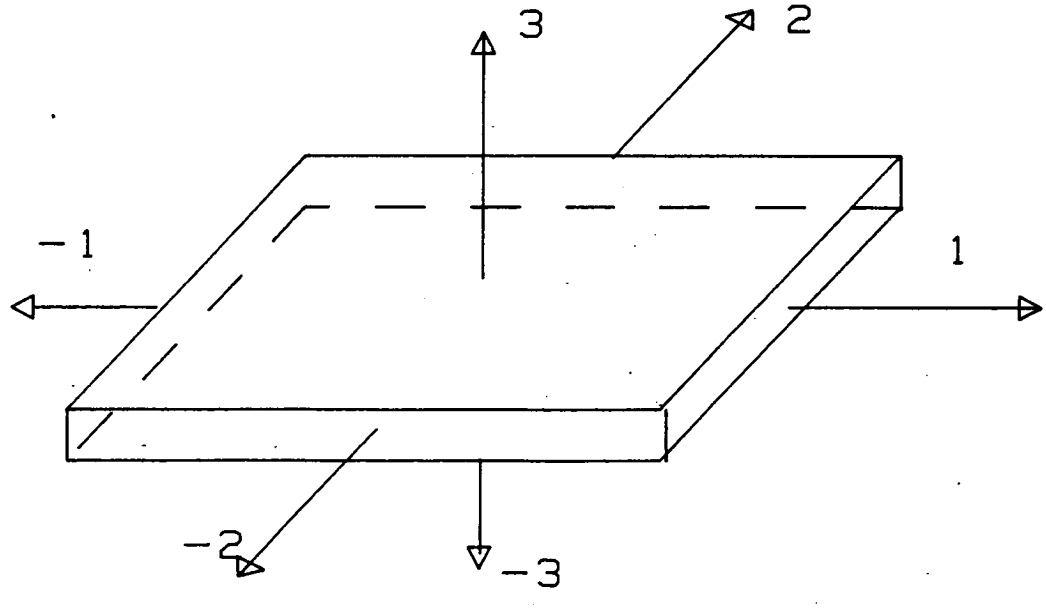

Figure B1: Numerical Convention of Axes.

Conventions have been established which identify the film's axes by the numerals indicated in fig. B1 where: 1 corresponds to length, 2 to width and 3 to thickness. By the same conventions, direction-dependent constants have two subscripts: the first identifies the axis of applied (or induced) electric field (or charge)

and the second identifies the axis of induced mechanical strain(or applied stress).

B.1 Properties of PVDF Piezo Film.

Relevant characteristics of PVDF films are summarised in appendix C. Some of these properties are self explanatory, but the most pertinent to piezoelectric properties which require some clarification are : the piezo stress and piezo strain constants.

B.2 Piezo Stress Constant (g-constant).

The g-constant is the negative of the electric field developed by the film, under open circuit conditions, along axis j, relative to the stress applied along axis i. The axes i and j may take any of the values of 1, 2 and 3 (figure B1).

$$-g_{ij} = \frac{Field\ developed\ along\ axis\ j}{stress\ applied\ along\ axis\ i} = \frac{V/m}{N/m^2} = \frac{Vm}{N}$$

The stress constant may also be expressed as the amount of strain induced along axis j relative to the applied electrical charge per unit area of electrode (mostly across axis 3), under stress free conditions

$$-g_{3j} = \frac{strain\ developed\ along\ axis\ j}{applied\ charge/elctrode\ area} = \frac{m\,m}{C/m^2} = \frac{m^2}{C}$$

B.1.2Piezoelectric Strain Constant (d-constant).

When deformation in a piezo material is caused by an applied electrical field, then the degree of deformation (strain) under stress-free conditions is given by:

$$-d_{ij} = \frac{strain\ developed\ along\ axis\ j}{applied\ electric\ field\ across\ axis\ i} = \frac{m/m}{v/m} = \frac{m}{v}$$

Strain constant can also be expressed as the ratio of short circuit charge per unit area across the plates (normally across axis 3) to the stress applied along axis j.

$$-d_{31} = \frac{charge\ per\ electrode\ area\ across\ axis\ 3}{stress\ applied\ along\ axis\ j}$$
$$= \frac{C/m^2}{N/m^2} = \frac{C}{N}$$

Piezo electricity involves the electrical and mechanical characteristics of the material. Definitions of constants such as Young's modulus, permittivity etc., are not included in this section, but their values are shown in Appendix C.

APPENDIX C

TYPICAL PROPERTIES OF PVDF FILM USED

PROPERTIES OF THE PVDF FILM USED			
Property	symbols	Values	Units
Piezo strain constant	d_{31} d_{32} d_{33}	$23x10^{-12}$ $3x10^{-12}$ $3x10^{-12}$	(m/m)(V/m) or $(C/m^2)/(m/m)$ or $(N/m^2)/(V/m)$
Piezo stress constant	g_{31} g_{32} g_{33}	$216x10^{-3}$ $19x10^{-3}$ $-399x10^{-3}$	$(V/m)/(N/m^2)$ or $(m/m)/C/m^2)$
Permittivity	ϵ	$106x10^{-12}$	F/m
Capacitance	C	$379x10^{-12}$	F/cm^2
Young's Modulus	Y	$2x10^9$	N/m^2

The properties shown above are the ones relevant for this thesis.

APPENDIX D

DESIGN CALCULATIONS FOR PVDF TRANSDUCER

In appendix B, we have defined some of the constants which characterise piezo electric activity and provided a tool in calculations. In this appendix we shall outline briefly the relevant steps required to calculate the voltage induced and the charge generated by an external force stressing the film in one of the three axes.

When the transducer is used to detect small displacements, the objective is to use the plastic properties of the film. By holding one of the axes as the neutral axis any deformation is going to compress or expand the other surface, with minimum stress exerted on the neutral surface. This deformation may be converted to a corresponding stress value using Young's law of elasticity. Assuming that the deformation of a film length l metres, width w metres and thickness t metres, changes the length of the film from l to l'. then the strain on the film is :

$$strain = \frac{(l' - l)}{l} \tag{4B.1}$$

The stress applied can be found by :

$$Stress\ S = strain\ .\ Y \tag{4B.2}$$

Where Y is Young's modulus of elasticity.

If the force is exerted on axis 1 and the induced voltage is across axis 3, then once the stress is calculated, the voltage developed across the plates of the film is

given by:

$$V = g_{31} \cdot S \cdot t \qquad (4B.3)$$

Regarding the film structure which uses parallel plates, then the capacitance is C = ϵ area /thickness. The permittivity of the piezo film is given in appendix C, and can be expressed as $\epsilon = \epsilon_r \epsilon_0$, where ϵ_0 is the permittivity of free space and is given as 8.854×10^{-12} F/m, and ϵ_r is the relative permittivity Therefore the charge developed across the plates is given by:

$$Charge = Q = C\ V \qquad (4B.4)$$

From the above brief outline of the calculations one can conclude that for an effective voltage output the higher percentage of the film area should come under the influence of the force in order to increase the strain, hence the stress. If only a part of the film metallised surface is excited by the force then the passive parts of the metallised area act as capacitance in parallel with the capacitance of the active part. This distributes the charge over the entire area (charge sharing) which in turn, reduces the total charge available at the charge amplifier.

References

1. Talbert, D.C., Lyn_Davies, W., Johnson, F., Abraham, N., and Colley, N., "Wide Bandwidth Fetal Phonocardiography Using a Sensor the Compliance of the Mother's Abdominal Wall," *IEEE Trans. Biomed. Eng.*, vol. BME-33 No.2, pp. 175-180, Feb. 1986.

2. Boddy, K. and Dawes, G.S., "Fetal Breathing," *Br. Med. Bull.*, vol. 31, No. 1, pp. 3-7, 1975.

3. Dawes, G.S., Fox, H.E., Leduc, B.M., Liggins, G.C., and Richards, R.T., "Respiratory Movements and Rapid Eye Movement Sleep in the Foetal Lamb," *J. Physiol.*, vol. 220, pp. 119-143, 1972.

4. Boddy, K., "Fetal Circulation and Breathing Movements," in *Fetal Physiology and Medicine*, ed. Baird and Nathanielz, pp. 302-328, W. Saunders and Co., 1976.

5. Boddy, K. and Robinson, J., "External Method for Detection of Fetal Breathing in Utero," *Lancet ii*, pp. 1231-1233, 1971.

6. Manning, F.A. and Platt, L.D., "Fetal Breathing Monitoring- Clinical Considerations," *Semin. Perinatal.*, vol. 4, p. 311, 1980.

7. Wladimiroff, J.W. and ligtvoet, C.M., and Sperman, J.A., "Combined One- and Two-dimensional Ultrasound System for Monitoring Fetal Breathing Movements," *BR. Med. J.*, vol. 2, pp. 975-976, 1976.

8. Gough, J.D. and Poore, E.R., "A Continuous Wave Doppler Ultrasound Method of Recording Fetal Breathing in Utero," *Ultrasound in Med. Biol.*, vol. 5, pp. 249-256, 1979.

9. Manning, F.A., Harman, C.R., Lange, I.R., and Morrison, I., "Fetal Assessment By Biophysical Profile Scoring: 1985 Update," *Eur. J. Obstet. Gynecol.*

Reprod. Biol., vol. 21, pp. 331-339, 1986.

10. Devoe, L.D. and Searle, J.R., "The Fetal Biophysical Profile: Antepartum Assessment Using a Programmed Microcomputer," *J. Clinical Eng.*, vol. 11 No. 4, pp. 285-289, Jul-August 1986.

11. Boddy, K. and Mantell, C., "Observation of Fetal Breathing Movement Transmitted Through maternal Abdominal Walls," *Lancet ii*, pp. 1219-1220, 1971.

12. Manning, F.A., Pugh, E. Wyn, and Boddy, K., "Effect of Cigarette Smoking on fetal breathing Movements in normal pregnancies," *Br. Med. J.*, vol. 1, pp. 552-553, 1975.

13. Manning, F.A., Platt, L.D., and Sipos, L., "Antepartum Fetal Evaluation: Development of a Fetal Biophysical Profile," *Am. J. Obstet. Gynecol.*, vol. 136, pp. 787-803, 1980.

14. Goovaerts, H.G., Rompelman, O., and Geijn, H.P. Van, "A Transducer for Detection of Fetal Breathing Movements," *IEEE Trans. Biomed. Eng.*, vol. 36 No. 4, pp. 471-478, April 1989.

15. Fox, H.E., "Fetal Breathing Movements and Ultrasound," *Am. J. Dis. Child*, vol. 130, pp. 127-129, Feb. 1976.

16. Tremewan, R.N., Aickin, D.R., and Tait, J.J., "Ultrasonic Monitoring of Fetal Respiratory Movement," *Br. Med. J.*, vol. 1, pp. 1434-1435, June 1976.

17. Arduini, D., Rizzo, G., Pennestri, F., and Romanini, C., "Modulation of Echocardiographic Parameters by Fetal Behaviour," *Prenatal Diagnosis*, vol. 7, pp. 179-187, 1987.

18. Rapoport, I. and Cousin, A.J., "New Phase-lock Tracking Instrument for Foetal Breathing Monitoring," *Med. Biol. Eng. and Comp.*, vol. 20, pp. 1-6,

Jan. 1982.

19. Timor-tritsch, I.E., Diecker, L.J., Hertz, R.H., Zador, I., and Rosen, M.G., "Human Fetal Respiratory Movements: a Technique for Noninvasive Monitoring with the use of a Tochodynamometer," *Biol. Neonates*, vol. 36, pp. 19-24, 1979.

20. Stagg, J. and Gennser, G., "Electronic Analysis of Foetal Breathing Movements: A Practical Application of Phase-Lock-Loop Principles," *J. Med. Eng. and Technology*, vol. 2, No. 5, pp. 246-249, Sept. 1978.

21. Chen, C., *Active Filter Design,* Hayden, NJ, 1982.

22. Valkenburg, M.E. Van, *Analog Filter Design,* Holt-Saunders, NY, 1982.

23. Clayton, G.B., *Operational Amplifiers,* Butterworths, 1979.

24. Colley, N., Talbert, D.G., and Southall, D.P., "Biophysical Profile in the Fetus from a Phonographic Sensor," *Eur. J. Obstet. Gynecol. Reprod. Biol.*, vol. 23, pp. 261-266, 1986.

25. Oppenheim, A.V., Wilsky, A.S., and Young, I.T., *Signals And Systems,* Prentice-Hall, NJ, 1983.

26. Oppenheim, A.V. and Schafer, R.W., *Digital Signal processing,* Prentice Hall, 1975.

27. Haykin, S., in *Digital Communication*, Wiley, 1988.

28. Penwalt,, *PVDF Technical Information*, 1983.

29. Chatigney, J.V. and Robb, L.E., "Sensors: Making the Most of Piezo Film," *Sensor Review*, vol. 7(1), pp. 15-20, 1986.

30. Charlton, T. M., *Principles of Structural Analysis,* Longmans, London, 1969.

31. Kay, S.M. and Marple, S.L., "Spectrum Analysis - A Modern Perspective,"

Proc. IEEE, vol. 96,No. 11, pp. 1380-1418, Nov. 1981.

32. Kay, S.M., *Modern Spectral Estimation, Theory and Application,* Prentice-Hall, New Jersey, 1988.

33. Roberts, R.A. and Mullis, C.T., *Digital Signal Processing,* Addison-Wesley, 1987.

34. Marple, S.L., *Digital Spectral Analysis with Applications,* Prentice-Hall, New Jersey, 1987.

35. Kinkel, J.F., Perl, J., Scharf, L.L., and Stubberud, A.R., "A Note on Covariance-Invariant Digital Filter Design and Autoregressive Moving Average Spectrum Analysis," *IEEE Trans. Acoust. Speech Signal Processing*, vol. ASSP-27 No.2, pp. 200-202, April 1979.

36. Linkens, D.A., "Short-Time-Series Spectral Analysis of Biomedical Data," *IEE Proc.*, vol. 129,Pt. A, No. 9, pp. 663-672, dec. 1982.

37. Akaikie, H., "A New Look at the Statistical Model Identification," *IEEE Trans. Autom. Contr.*, vol. AC-19, pp. 716-723, Dec. 1974.

38. Parzen, E., "Some Recent Advances in Series Modeling," *IEEE Trans. Autom. contr.*, vol. AC-19, pp. 723-730, Dec. 1974.

39. Ulrych, T.J. and Clayton, R.R., "Time Series Modelling and Maximum Entropy," *Phys. Earth Planet. inter.*, vol. 12, pp. 188-200, 1976.

40. Ulrych, T. and Ooe, M., "Autoregressive and Mixed ARMA Models and Spectra," in *Nonlinear Methods of Spectral Estimation*, ed. S. Haykin, p. Chapter 3, Springer-Verlag, New York, 1983.

41. Honig, M.L. and Messerschmitt, D.G., *Adaptive Filters, Structures, Algorithms, and Applications,* Kluwer Academic Press, MA-USA, 1984.

42. Widrow, B. and Stearns, S.D., *Adaptive Signal Processing,* Prentice-Hall, New Jersey, 1985.

43. Widrow, B. and McCool, J.M., "A Comparison of Adaptive Algorithms Based on the Methods of Steepest Descent and Random Search," *IEEE Trans. Antennas Propag.*, vol. AP-24 No.5, pp. 615-638, Sept. 1976.

44. Leib, H., Eizeman, M., Pasupathy, S., and Krolik, J., "Adaptive Lattice Filter for Multiple Sinusoids in White Noise," *IEEE Acous. Speech Sig. Proc.*, vol. ASSP-35, No. 7, pp. 1015-1023, July 1987.

45. Makhoul, J., "Linear Prediction: A Tutorial Review," *IEEE Proc.*, vol. 63, pp. 561-580, April 1975.

46. Levy, J.B. and Linkens, D.A., "Spectral Analysis of Short-time Biomedical Data Using Adaptive Filters," *IEE Proc.*, vol. 131,Pt. A,No. 3, pp. 164-169, May 1984.

47. Griffiths, L.J., "Rapid Measurement of Digital Instantaneous Frequency," *IEEE Trans. Acoust. Speech Sig. Proc.*, vol. ASSP-23 No.2, pp. 207-222, April 1975.

48. Giordano, A.A. and Hsu, F.M., *Least Square Estimation with Application to Digital Signal Processing,* John Wiley, New York, 1985.

49. Swingler, D.N., "A Modified Burg Algorithm for Maximum Entropy Spectral Analysis," *Proc. IEEE*, vol. 67 No.9, pp. 1368-1369, Sept. 1979.

50. Scott, P.D. and Nikias, C.L., "Energy-Weighted Linear Predictive Spectral Estimation: A New Method Combining Robustness and High Resolution," *IEEE Trans. Acoust. Speech Signal Process.*, vol. ASSP-30 No.2, pp. 287-293, April 1982.

51. Kaveh, M. and Lippert,, "An Optimum Tapered Burg Algorithm for Linear

Prediction and Spectral Analysis," *IEEE Trans. Acoust. Speech Signal Processing*, vol. ASSP-31, pp. 433-444, April 1983.

52. Helme, B.I., "Improved Spectrum Performance Via a Data-Adaptive Weighted Burg Technique," *IEEE Trans. Acoust. Speech Signal Process.*, vol. ASSP-33 No.4, pp. 903-910, Aug. 1985.

53. Widrow, B., McCool, J.M., Larimore, M.G., and Johnson, C.R., "Stationary and Nonstationary Learning Characteristics of the LMS Adaptive Filter," *Proc. IEEE*, vol. 64 No.8, pp. 1151-1162, Aug. 1976.

54. Rich, E., *Artificial Intelligence*, McGraw-Hill, 1983.

55. Zimmermann, H.J., *Fuzzy Set Theory- and its Applications*, Kluwer-Nijhoff, 1985.

56. Forsyth, R., *Expert Systems: Principles and case studies*, Chapmann and Hall, 1984.

57. Kandel, A., *Fuzzy Mathematical Techniques with Applications*, Addison-Wesley, 1986.

58. Waterman, D.A., *A Guide to Expert Systems*, Addison-Wesley, 1986.

59. Gondran, M., *An Introduction to Expert Systems*, McGraw-Hill, 1986.

60. Daku, B.L.F., Grant, P.M., Cowan, C.F.N., and Hallam, J., "Intelligent Techniques for Spectral Estimation," *Journal of IERE*, vol. 58 No. 6, pp. 275-283, Dec. 1988.

61. Ziedler, J.R., Satorius, E.H., Chabries, D.M., and Wexler, H.T., "Adaptive Enhancement of Multiple Sinusoids in Uncorrelated Noise," *IEEE Trans. Acoust. Speech and Signal Processing*, vol. ASSP-26 No. 3, pp. 240-254, June 1978.

62. Widrow, B., Glover, J.R., McCool, J.M., Kaunitz, J., Williams, C.S., Hearn, R.H., Zeidler, J.R., Dong, E., and Goodlin, R.C., "Adaptive Noise Cancelling: Principles and Applications," *Proc. IEEE*, pp. 1692-1716, Dec. 1975.

63. Jarisch, W. and Detwiler, J.S., "Statistical Modelling of Fetal Heart Rate Variability," *IEEE trans. Biomed. Eng.*, vol. BME-27, pp. 582 - 589, Oct. 1980.

64. Bow, Sing-Tze, *Pattern Recognition - Application to Large Data-Set Problems*, Marcel Dekker, New York, 1984.

65. Therrien, C.W., *Decision Estimation and Classification - An Introduction to Pattern Recognition and Related Topics*, John Wiley & Sons, New York, 1989.

66. Castleman, K.R., *Digital Image Processing*, Prentice-Hall, NJ, 1979.

67. Chatfield, C. and Collins, A.J., *Introduction to Multivariate Analysis*, Chapman and Hall, London, 1980.

68. Manly, B.F.J., *Multivariate Statistical Methods - A Primer*, Chapman and Hall, London, 1986.

69. Hand, D.J., *Discrimination and Classification*, John Wiley & Sons, 1981.

70. James, M., *Classification Algorithms*, Collins, London, 1985.

71. Widrow, B., Winter, R.G., and Baxter, R.A., "Layered Neural Nets for Pattern Recognition," *IEEE Trans. Acoustic Speech and signal Process.*, vol. 36 No. 7, pp. 1109-1118, July 1988.

72. Lippmann, R.P., "An Introduction to Computing with Neural Nets," *IEEE ASSP Magazine*, pp. 4-22, April 1987.

73. Huang, W. and Lippmann, R.P., "Comparisons Between Neural Net and Conventional Classifiers," *IEEE Int. Neural Net Conf.*, pp. 485-493, San Diego, 1987.

74. Goovaerts, H.G., *Instrumentation for the Quantitative Assessment of Fetal Respiratory Sinus Arrhythmia,* Ph.D. Thesis, Vrij University, Amsterdam Holland, 1989.

PUBLICATIONS AND PRESENTATIONS

[1] Ansourian M.N., J.H. Dripps G.J. Beattie J.R. Jordan and K. Boddy "Measurement of Fetal Breathing Movement and Fetal Heart Sounds" presented at the meeting on *BIO-ENGINEERING MEASUREMENTS* held by the British Strain Society 22nd March 1989 Edinburgh Scotland, UK.

[2] Beattie G.J., M.N. Ansourian J.H. Dripps and K. Boddy "Monitoring of Fetal Breathing Movements and Fetal Heart Sounds" 2nd Simpson Symposia Sept. 1989 Edinburgh Scotland, UK.

[3] Ansourian M.N., J.H.Dripps G.J. Beattie and K. Boddy "Analysis of Fetal Breathing Movements" 2nd Simpson Symposia Sept. 1989 Edinburgh Scotland, UK.

[4] Ansourian M.N., J.H. Dripps G.J. Beattie and K. Boddy "Autoregressive Spectral Estimation of Fetal Breathing Movements" IEEE Trans Biomed. Eng. vol. 36 No. 1, pp. 1076-1084, Nov. 1989

PAPER SUBMITTED FOR REVIEW

Ansourian M.N. J.H. Dripss and A.R. Mirzai "Performance Comparison of Neural Networks and Conventional Classification Techniques for Biomedical Signals" submitted for review in July 1989 to the IEEE Trans. for Biomed. Eng.

Autoregressive Spectral Estimation of Fetal Breathing Movement

MEGEURDITCH N. ANSOURIAN, JAMES H. DRIPPS, GERALD J. BEATTIE, AND KEN BODDY

Abstract—Fetal breathing movement (FBM) *in utero* may be an indicator of fetal health. This paper provides a second-by-second estimate of FBM rate. In the absence of a statistical model for the fetal breathing movement, block data structured autoregressive spectral estimation is used. The optimum tapered Burg algorithm provides a minimum variance breathing rate estimate from a short block of data. The data were recorded using a PVDF (PolyVinyliDeneFluoride) transducer which picks up maternal abdominal wall movements. A peak tracking algorithm is used to extract the fetal breathing rate. Results from these signals are presented in graphical form. Further analysis of the fetal breathing rate has revealed periodicities, similar to that observed in the fetal heart rate.

I. Introduction

HUMAN fetal breathing movements (FBM) were first recorded, by Ahlfeld, at the turn of this century. His observation of maternal abdominal wall movements (MAM) representing fetal breathing movements *in utero* was disbelieved by his peers. The development of catheter placement techniques and advancements in blood gas determination made it possible to confirm FBM in exteriorized fetal lambs. Such observations were attributed, at that time, to external or asphyxial stimuli. FBM were subsequently confirmed to be normally present using fetal lambs *in utero*. Developments in ultrasound have now made it possible to conduct examinations of the human fetus *in utero* with minimum external stimuli.

Gough and Poore [7] used a continuous-wave (CW) Doppler ultrasound to detect FBM indirectly through its presumed effect on blood velocity in the hepatic vein and the inferior vena cava.

In [2]–[6], [8]–[10], real-time ultrasound imaging was used. The ultrasound beam was aligned with the fetal thorax and the X-scan output from the distal or proximal chest wall echo was recorded. The output varied in sympathy with fetal chest wall movements and thus indicated FBM [4]. Stagg and Gennser [9] processed the fetal thoracic wall movements using a phase-locked loop (PLL) where the filtered phase comparator output provided FBM rate directly in analog form. The PLL method is an analog realization of mean-squared phase error optimization. In the above, commercially available real-time ultrasound scanners were used with a single gate movement tracker. Rapoport and Cousin [11] adapted a commercially available scanner to incorporate a multiple gate movement tracking facility. This provided simultaneous tracking of both the fetal chest wall and diaphragm movements.

The recording methods described thus far require frequent realignment of the ultrasound beam following fetal movements. This method necessitates the presence of a trained observer throughout the recording.

The aim of this paper is to present a digital analysis using autoregressive (AR) power spectral estimation or perceived FBM signal, transmitted through maternal abdominal wall [1], [3]. Section II discusses the data acquisition. Section III reviews the concept of AR spectral analysis and discusses the advantages of the optimum tapered Burg algorithm, which is based on the maximum entropy spectral estimation. Section IV presents the results in graphical form.

II. Data Acquisition

In this paper, we used maternal abdominal wall movements (MAM) to indicate FBM [3]. A PVDF transducer was used to convert maternal abdominal wall movements into electrical signal. These signals were corroborated as an FBM signal by an obstetrician using a real-time ultrasound scanner. In Fig. 1, the square pulses indicate the obstetrician's perception of FBM by observing fetal thorax and diaphragm; the top trace is the transduced maternal abdominal wall movements. As observed by [2]–[4], [6]–[9], and [11], the FBM rate lies between 30–90 breaths/min (0.5–1.5 Hz). The transduced signal is filtered using a cascaded second-order low-pass filter with 2 Hz cutoff frequency and a second-order high-pass filter with a cutoff frequency of 0.5 Hz. The resultant band-passed MAM signal will contain FBM and other signals pertaining to fetal and maternal biological activities. The significance of these undesired signals will vary according to the FBM intensity, and will become of relative significance when the FBM component becomes small.

Fig. 2 shows 5 min of filtered MAM signal, and Fig. 3 shows three 60 s blocks of contiguous data. From Figs. 2 and 3, the following conclusions may be deduced:

1) the FBM rate varies throughout the recording
2) the MAM signal processes a time-varying amplitude.

Therefore, the filtered MAM signal may be modeled as being a frequency and amplitude modulated signal where the carrier may not be a pure sinusoid.

In the absence of a statistical model for the above variations 1) and 2), one is compelled to analyze the data in short data blocks. This forces the signal to behave as small-sense stationary. Spectral estimation using the classical FFT approach suffers from poor frequency resolution for short data blocks. Mixed autoregressive-moving average (ARMA) displays good modeling and resolution properties, but the algorithm is not guaranteed to converge to a global minimum. In addition, the computational complexities involved encourage one to search other less complex algorithms. FBM, which is stochastic signal, can be modeled as an AR process. The resolution of an AR analysis is not dependent on data block length, but rather on model order, sampling interval, and signal-to-noise ratio [22], [23].

$$\text{resolution}_{AR} = \frac{1.03}{T_s p\left[\eta(p+1)\right]^{0.31}} \tag{1}$$

η = SNR of a single sinusoid (linear)
T_s = sample interval
p = model order.

III. Autoregressive (AR) Spectral Analysis

An AR spectral analysis is a process whereby the present data sample x_n is estimated from knowledge of its past samples.

$$x_n = -\sum_{k=1}^{k=p} a_k x_{n-k} \tag{2}$$

where x_n is the nth data sample, p is the filter length, and $\{a_k : k = 1, 2, \cdots, p\}$ is the filter characteristics of the generating (AR) process.

The above process is modeled as an all-pole (recursive) filter where the transfer function is

$$H(z) = \frac{1}{\sum_{k=0}^{k=p} a_k z^{-k}} \tag{3}$$

where a_0 is always 1.

The relationship between the autocorrelation function of the input signal and the modeling parameters is given by [13], [14]

$$R_{xx}(n) = \begin{cases} -\sum_{k=1}^{k=p} a_k R_{xx}(n-k) & n > 0 \\ -\sum_{k=1}^{k=p} a_k R_{xx}(k) + \sigma^2 & n = 0 \end{cases} \tag{4}$$

where σ^2 is the variance of the output.

Expressions in (4) are the well-known Yule-Walker equations. In order to develop an AR power spectral estimate, the coefficients $\{a_k; k = 1, 2, \cdots, p\}$ must be evaluated.

The Levinson-Durbin algorithm provides an efficient recursive solution to the Yule-Walker equations requiring $o(p^2)$ (order of p^2) operations. The Levinson-Durbin algorithm computes recursively the filter coefficients and the variance σ^2. It was shown in [13], [14], [19] that $a_p[n]$, which denotes the nth coefficient of the pth-order linear prediction, is given by

$$a_p[n] = a_{p-1}[n] + a_p[p]a_{p-1}^*[p-n] \tag{5}$$

for $n = 1, 2, \cdots, p-1$.

The superscript (*) denotes the complex conjugate.

$a_p[n]$, which is also equated to the reflection coefficient K_p, is

$$a_p[p] = K_p = \frac{-\sum_{k=0}^{k=p-1} a_{p-1}[n]R_{xx}(p-n)}{\sigma_{p-1}^2}. \tag{6}$$

Equation (4) can also be expressed in terms of the reflection coefficient

$$a_p[n] = a_{p-1}[n] + K_p a_{p-1}^*[p-n]. \tag{7}$$

The final set of coefficients for (7) at model order p is the desired solution. The procedure for solving (7) uses the following:

$$\sigma_0^2 = R_{xx}(0)$$

$$a_{p-1}[0] = 1 \quad \text{for all } p$$

$$a_1[1] = K_1 = -R_{xx}(1)/R_{xx}(0)$$

$$\sigma_1^2 = (1 - K_1^2)R_{xx}(0)$$

and

$$\sigma_p^2 = (1 - K_p^2)\sigma_{p-1}^2.$$

If the linear prediction error filter is implemented using the lattice filter structure, as shown in Fig. 4, then the forward and backward prediction errors are defined as [19]

$$ef_p[n] = x[n] + \sum_{k=1}^{k=p} a_p[k]x[n-k]. \tag{8}$$

And the backward prediction error is

$$eb_p[n] = x[n-p] + \sum_{k=1}^{k=p} a_p^*[k]x[n+k-p]. \tag{9}$$

Using $p-1$ in (9) and substituting into (8), the forward and backward prediction errors become

$$ef_p[n] = ef_{p-1}[n] + K_p eb_{p-1}[n-1] \tag{10}$$

$$eb_p[n] = eb_{p-1}[n-1] + K_p^* ef_{p-1}[n]. \tag{11}$$

The negated reflection coefficient K_p is also known as the PARCOR coefficient (Partial correlation coefficient) between the forward and backward linear prediction errors.

The Burg algorithm [13], [15]–[17], [19] uses the Levinson-Durbin recursive solution to the Yule-Walker equations. The PARCOR coefficient is based on the minimization of the arithmetic mean of the forward and backward linear prediction error power. This yields the PARCOR coefficient estimate

$$K_p = \frac{-2\sum_{k=p}^{k=N-1} W_{p-1}[k]ef_{p-1}[k]eb_{p-1}^*[k-1]}{\sum_{k=p}^{k=N-1} W_{p-1}[k]\left(|ef_{p-1}[k]|^2 + |ef_{p-1}[k-1]|^2\right)} \tag{12}$$

where $W_{p-1}[k]$ is a nonnegative weighting function [19].

Burg selected a uniform weighting function where $W_p[k] = 1/N$ and where N is the total number of data samples available.

A uniform tapered window provides an AR power spectral estimate with errors in the estimated frequencies [16], [17]. The errors are dependent on the length of the data block, the signal phase, and the sampling frequency. These frequency errors can be reduced if the window is optimized [19]. Such optimization is acheived by minimizing the average variance of the estimated frequency. The optimum weighting function is not a constant value, and may be computed recursively [19] as follows:

$$W_m[k] = 2W_m[k-1] - W_m[k-2] - \lambda_m$$

$$\lambda_m = \frac{12}{(N-m+1)(N-m+2)(N-m+3)} \tag{13}$$

where λ_m is the Lagrange multiplier, and $W_0 = 0$, and $W_1 = N\lambda_1/2$.

The Burg algorithm and the optimized Burg algorithm yield the same desired properties, i.e., guaranteed stability, spectral resolution. But the optimized tapered Burg algorithm alleviates spectral line splitting and decreases errors in the estimated frequencies.

IV. Results

The optimum tapered Burg algorithm was used in analyzing fetal breathing movements. This algorithm is able to accurately determine spectral contents from short data blocks. The data block length used in our analysis was of 2 s duration (20 samples). The data block chosen is long enough to ensure that a full wavelength of the lowest possible frequency of FBM (0.5 Hz) is present for the autocorrelation estimates, while still being short enough for the data block to be stationary, hence validating a Toeplitz autocorrelation matrix assumption [14]. The Toeplitz characteristic of the matrix is necessary for the Levinson-Durbin decomposition.

Akaikie [24] and Parzen [25] developed different criteria for model order selection. Ulrych and Ooe [26] have tried different information criteria for model order selection and suggested that for a short time series, a model order of 1/3 to 1/2 of the data length would give satisfactory results. Hence, an eighth-order autoregressive spectal model was assumed in our analysis.

Fig. 5 outlines the signal flow at each stage of processing. Analysis of the data is presented graphically in Figs. 6–11. Figs. 6, 7, and 8 depict waterfall representation of the AR spectral estimate for 100 s each. The analysis uses 2 s sliding window with a 1 s overlap. The time traverses along the horizontal axis from 0 to 3 Hz. The boxed waveform represents the 100 s of filtered MAM signal used for each figure.

In biomedical signals, the problem of time-varying characteristics is nearly always present. Such characteristics for MAM signals were discussed in Section II. The tracking of the relevant frequency components under these time-varying characteristics is not a straightforward task. Nevertheless, these characteristics may often possess some significant biological activity.

At the onset, the analysis was to provide a fast and efficient method for a second-by-second estimation of FBM rate. This was achieved by employing an intelligent peak tracking algorithm. This is a rule-based algorithm which looks retrospectively at the running FBM mean and weights, in a Gaussian spread, the spectral peaks in accordance to their distance from the mean. The rule-based peak tracking algorithm takes into consideration the amplitude of the FBM signal to provide a figure of confidence in the tracked peak.

Fig. 9 depicts the tracked FBM rate. This satisfies the main objectives of the analysis, but further filtering of the estimated FBM rate reveals short-term periodicity. Fig. 11, which depicts the spectral estimate of the tracked FBM, reveals signal corrupted by noise. The filtering was achieved through a transversal filter employing the Widrow least mean-square (LMS) algorithm [28], [29], which enhances periodic signals corrupted by colored or white noise. Fig. 10 depicts the filtered FBM rate. The short-term periodicity in FBM rate is clearly identified. Fig. 12 depicts the spectral density of the filtered FBM rate. The short-term periodicity is identified from Fig. 12 to be about 25 s (0.04 Hz).

V. Discussion

The system described monitors FBM represented by maternal abdominal wall movements. Estimation of breathing rate is achieved using digital signal processing (optimum tapered Burg algorithm). These estimates present the supervising obstetrician a quantified parameter of FBM rate, which is another dimension in the assessment of fetal health *in utero*.

Most biological activities possess both long-term and short-term periodicities. In our study, we have observed the presence of short-term periodicities in FBM rate; the period, shown in Figs. 8 and 10, was found to be about 25 s. The FBM rate normally varies from 30 breaths/min to 90 breaths/min [2], [3], but on a few occasions, the rate went up to 160 breaths/min. Fetal heart rate (FHR) is known to vary between 90–200 beats/min. During instances of high FBM rate, the FHR was observed to be different; hence, the rates of the two activities were not confused.

This is an ongoing research program, and the dependence of short-term periodicity on gestation age and other criteria will be investigated in the future.

VI. Conclusion

Most biological processes are nonstationary. Hence, proper modeling of signals from biological activities requires analysis based on short-time series. The optimum tapered Burg algorithm provides a good capability for modeling short-time series, and offers greater resolution over the classical FFT [22]. It also minimizes the average variance of estimated frequency and alleviates spectral line splitting. The advantages of the optimum tapered Burg algorithm are gained at the expense of increased computational complexity compared to that of the classical FFT.

Acknowledgment

The authors would like to thank the following for their assistance in this research: Dr. D. Southall and Dr. N. Colley, Department of Pediatrics, Cardiothoracic Institute, University of London; Dr. G. K. Manning, for his help and discussions; and the UGC UK for the signal acquisition and digitizing equipment.

References

[1] D. Talbert *et al.*, "Wide bandwidth fetal phonography using a sensor matched to a compliance of the mother's abdominal wall," *IEEE Trans. Biomed. Eng.*, vol. BME-33, pp. 175–180, Feb. 1986.

[2] K. Boddy and G. Dawes, "Fetal breathing," *Brit. Med. Bull.*, vol. 31, no. 1, pp. 3–7, 1975.

[3] K. Boddy and C. Mantell, "Observation of fetal breathing movement transmitted through maternal abdominal walls," *Lancet*, vol. ii, pp. 1219–1220, 1972.

[4] K. Boddy and J. Robinson, "External method for detection of fetal breathing in utero," *Lancet*, vol. ii, pp. 1231–1233, 1971.

[5] R. Tremewan, D. Aickin, and J. Tait, "Ultrasonic monitoring of fetal respiratory movement," *Brit. Med. J.*, vol. 12, pp. 1434–1435, June 1976.

[6] J. Wladimiroff *et al.*, "Combined one and two dimensional ultrasound system for monitoring fetal breathing movements," *Brit. Med. J.*, vol. 2, pp. 975–976, 1976.

[7] J. Gough and E. Poore, "A continuous wave Doppler ultrasound method of recording fetal breathing in utero," *Ultrasound Med. Biol.*, vol. 5, pp. 249–256.

[8] D. Arduini *et al.*, "Modulation of echocardiographic parameters by fetal behaviour," *Prenatal Diagnosis*, vol. 7, pp. 179–187, 1987.

[9] J. Stagg and G. Gennser, "Electronic analysis of foetal breathing movements: A practical application of phase-lock-loop principles," *J. Med. Eng. Tech.*, vol. 2, pp. 246–249, Sept. 1978.

[10] L. Devoe and J. Seale, "The fetal biophysical profile: Antepartum assessment using a programmed microcomputer," *J. Clin. Eng.*, vol. 11, pp. 285–289, July–Aug. 1986.

[11] I. Rapoport and A. Cousin, "New phase-lock tracking instrument for foetal breathing monitoring," *Med. Biol. Eng. Comput.*, pp. 1–6, 1982.

[12] K. Boddy, "Fetal circulation and breathing movements," in *Fetal Physiology and Medicine*, X. Beard and X. Nathanielz, Ed., vol. 1. Philadelphia, PA: Saunders, 1976, ch. 16.

[13] S. Kay and S. Marple, "Spectrum analysis—A modern perspective," *Proc. IEEE*, vol. 69, pp. 1380–1418, Nov. 1981.

[14] J. Makhoul, "Linear prediction: A tutorial review," *Proc. IEEE*, vol. 63, pp. 561–580, Apr. 1975.

[15] S. Kay, "Maximum entropy spectral estimation using the analytical signal," *IEEE Trans. Acoust., Speech, Signal Processing*, vol. ASSP-26, pp. 467–469, Oct. 1978.

[16] R. Keeler, "Uncertainties in adaptive maximum entropy frequency estimators," *IEEE Trans. Acoust., Speech, Signal Processing*, vol. ASSP-26, pp. 469–471, Oct. 1978.

[17] D. Swingler, "Frequency errors in MEM processing," *IEEE Trans. Acoust., Speech*, Signal Processing, vol. ASSP-28, pp. 257–259, 1980.

[18] M. Kaveh and Lippert, "An optimum tapered Burg algorithm for linear prediction and spectral analysis," *IEEE Trans. Acoust., Speech, Signal Processing*, vol. ASSP-31, pp. 433–444, Apr. 1983.

[19] A. Marple, *Digital Spectral Analysis with Application*. Englewood Cliffs, NJ: Prentice-Hall, 1987.

[20] R. Roberts and C. Mullis, *Digital Signal Processing*. Reading, MA: Addison-Wesley, 1987.

[21] C. McGillem and G. Cooper, *Continuous and Discrete Signal and System Analysis*. New York: Holt Rinehart and Winston, 1984.

[22] L. Marple, "Resolution of conventional Fourier, autoregressive and special ARMA methods of spectral analysis," in *Rec. 1977 IEEE Int. Conf. Acoust., Speech, Signal Processing*, May 1977, pp. 74–77.

[23] ——, "Frequency resolution of Fourier and maximum entropy spectral estimation," *Geophys.*, vol. 47, pp. 1303–1307, Sept. 1982.

[24] H. Akaikie, "A new look at the statistical model identification," *IEEE Trans. Automat. Contr.*, vol. AC-19, pp. 716–723, Dec. 1974.

[25] E. Parzen, "Some recent advances in the series modeling," *IEEE Trans. Automat. Contr.*, vol. AC-19, pp. 723–730, Dec. 1974.

[26] T. Ulrych and M. Ooe, "Autoregressive and mixed ARMA models and spectra," in *Nonlinear Methods of Spectral Analysis*, S. Haykin, Ed. New York: Springer-Verlag, 1983, ch. 3.

[27] A. V. Oppenheim and R. Schafer, *Digital Signal Processing*. Englewood Cliffs, NJ: Prentice-Hall, 1975.

[28] B. Widrow *et al.*, "Adaptive noise cancelling: Principles and applications," *Proc. IEEE*, vol. 63, pp. 1692–1716, Dec. 1975.

[29] B. Widrow and J. McCool, "A comparison of adaptive algorithms based on the method of steepest descent and random search," *IEEE Trans. Antennas Propagat.*, vol. AP-24, pp. 615–638, Sept. 1976.